Diploma Thesis

Improvement of the HMGU Neutron Dosemeter by Monte Carlo Simulations and Measurements

Matthias Volnhals

13th November 2012

HelmholtzZentrum münchen
German Research Center for Environmental Health

Abstract

In this work, investigation was done on the prototypes of the neutron dosemeters developed at the Helmholtz-Zentrum München (HMGU), by means of both simulation and experiment. These (active electronic personal) dosemeters consist of four sensors with different characteristics, i.e. converters and thresholds.

For the simulations, the Geant4 Monte Carlo framework was used. First, pulse height spectra of the four sensors at different neutron energies were obtained. Thereby the charge collection efficiency of the detectors was accounted for with an innovative analysis procedure. With an AmBe energy spectrum as an input, good agreement with a measured pulse height spectrum was found. The further acquired spectra provided insight into the functional principles that lead to signal creation. The dominant physical effects in different energy regions were identified. The influence of dosemeter and converter materials were studied, as well as the impact of a phantom.

Second, for the first time response functions of the prototype sensors were determined from thermal to several 100 MeV neutron energies by means of Geant4. Geometries with and without phantom were used. The results are discussed with the help of the previously acquired pulse height spectra. The impact of a phantom on the response functions was quantified.

Furthermore, experiments were conducted using the dosemeter prototypes in three different neutron fields.

At the Helmholtz-Zentrum Berlin (HZB), the various sensors were for the first time tested in a pulsed neutron field (with a burst frequency of 100 Hz) as part of an international measurement campaign. The experimental setup was also simulated using Geant4. In the measurements, linearity between count and fluence rate was established for all sensors, except for a slight excess at the highest rate for two sensors. Thus, the prototypes were demonstrated to work reliable in a pulsed field up to a neutron fluence rate of about $40 \cdot 10^3\,\mathrm{cm^{-2}s^{-1}}$. Also, irradiations were conducted with an AmBe source; thereby, differences in the "Albedo" sensor´s response were observed depending on the experimental setup. In both measurements the "Delta" sensor group was deactivated resulting in an underestimation of dose up to 40 %.

In an experiment at the Zugspitze, secondary cosmic radiation was measured with the dosemeter prototypes. The neutron energy spectrum was provided by a Bonner Sphere Spectrometer. Comparing the measured and expected counts, an excess in the former was observed, which is explained with the impact of other cosmic radiation but neutrons. Consequently, the sensors´ response to muons and protons was estimated with a Geant4 simulation for the first time. It could be shown that the proton fluence at the Zugspitze possibly caused around

12 % of the measured counts.

Eventually, the experimental results are compared with simulation outcomes, using corrected threshold settings for the sensors. An overall good agreement is observed, which is considered a verification of the simulations. Using the simulated data, suggestions are then made to improve the accuracy of the dose reading.

The experiment at the HZB and its results will be published as an article in an international journal soon.

Contents

List of Figures

List of Tables

1. Introduction

For many years now, dosimetry in and protection against neutron fields has become increasingly more important, which is due to the fact that neutron radiation occurs frequently in nature, and also in the technical field neutrons play an essential role. A prominent example for the latter is nuclear engineering; recently, however, with the application of proton and heavy ion accelerators for tumor treatment, producing a significant radiation background of secondary neutrons, also this field has begun to attract scientific attention ([1, 2, 3]). There, as well as for example in the field of secondary cosmic radiation in the atmosphere, the high-energetic fraction of the neutron radiation with kinetic energies of more than 20 MeV is essential for correct dose assessment ([4, 5, 6, 7, 8, 9, 10]). In general, the wide range over several orders of magnitude neutron energies cover in environment and industry poses a tremendous difficulty in the development of neutron dosemeters ([11, 12]).

Like with photon radiation, dose assessment in neutron fields, e.g. for medical staff, is based on measurements of the *personal dose equivalent* with *(personal) dosemeters*. *Passive* dosemeters are still commonly used for that task; that is, these devices are irradiated and read out afterwards, so that the dose acquired during the time in which the dosemeter has been worn can be determined. Passive devices are cheap, robust and easy to use; moreover, in many cases they offer various additional information on the radiation field, e.g. estimates of the angular and energy distributions ([13]). Therefore, passive dosemeters are state-of-the-art of technology, and for records in the official dose register (in Germany), usually the reading of a passive device is required ([13, 14]). This is despite the obvious advantages that *active* dosemeters would have over passive ones. Unlike the latter, these devices can *display* the current *dose rate* as well as the totally acquired dose during operation. The person wearing such a dosemeter can therefore check the conditions he or she is working in, and take precautions if it seems necessary. Danger as well as even accidents can be prevented with such devices, e.g. if audible warnings at high dose rates are enabled. On the other hand, efficiency of labor could also be enhanced in certain situations, for example if, due to a lack of information because of a passive-only dosemeter, preventive measures are taken, which would render unnecessary if an accurate active device was on hand.

However, only few active personal dosemeters for neutrons are available yet, and most of these are still in the stage of prototypes so far. This is due to the difficulties associated with the development of such devices. Not only is it necessary that the active dosemeters exhibit a certain accuracy in the dose reading over the already mentioned wide energy range, which is difficult to be achieved ([15, 12, 11, 14]); usual problems also include the low overall sensitivity

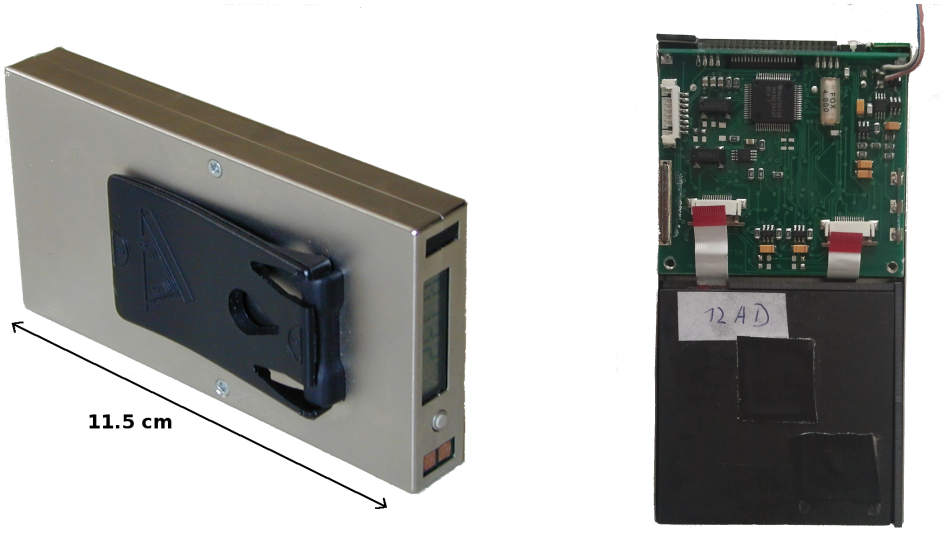

(a) Dosemeter prototype in casing, with an indication of the size

(b) Device with open casing

Figure 1.1.: Photographs of a HMGU neutron dosemeter prototype

with corresponding high detection limit and the under-estimation of dose at high dose rates or in pulse fields due to pile-ups ([16, 17, 18, 19]).

At the Institut für Strahlenschutz (ISS) of the Helmholtz-Zentrum München - Deutsches Forschungszentrum für Gesundheit und Umwelt (HMGU), an active electronic personal neutron dosemeter has been developed for several years ([20, 21, 22, 23, 24, 25]). It is designed to overcome some of the common problems in neutron personal dosimetry mentioned above. That is, it is equipped with four sensors in order to achieve a very uniform response from thermal up to more than 100 MeV neutron energy; due to the overall high sensitivity the detection threshold is very low. Very recently, the design of the HMGU neutron dosemeter prototypes was revised, and the newly constructed devices were tested in the fields of a Castor cask and the HMGU Americium-Beryllium (AmBe) source ([25]). A photograph of one of a dosemeter prototype is shown in figure 1.1a. In 1.1b, the same device with open casing is displayed.

The purpose of this work, was to study these dosemeters in their current design in detail. The overall aim was to develop suggestions for further improvement. For that, *experimental research* was conducted in three different neutron fields; these measurements revealed some drawbacks and limitations of the dosemeters. A main part of this work was *simulations* of the single sensors as well as the whole device with the *Monte Carlo* Geant4 toolkit ([26, 27]). The interpretation of the simulation results provided a complete understanding of the dosemeter and its functional principle. This allowed to give suggestions concerning the uniformity of the dose reading over the desired neutron energy range, which represents a major improvement of the HMGU dosemeter prototypes.

In chapter 2, a short overview is given over the scientific field of neutron dosimetry, and the current state of research in active neutron dosemeters is outlined. Chapter 3 then provides a detailed description of the HMGU prototypes, i.e. the *detectors*, the various *sensors* and the *dose assessment* procedure.

In chapter 4, the Monte Carlo simulations with GEANT4 conducted in this work are described. The simulations of the sensors are outlined and discussed in terms of *pulse height spectra*; a determination and discussion of the *response functions* of the sensors over a wide energy range is given next.

Chapter 5 deals with the experimental part of this work. The measurements in the three neutron fields at the HELMHOLTZ-ZENTRUM BERLIN (a pulsed field with burst frequency 100 Hz at neutron energies up to 68 MeV), of the HMGU AmBe source (with neutron energies up to 11 MeV) and at Zugspitze mountain (neutrons from secondary cosmic radiation with an energy range from thermal to more than 1 GeV) are described and discussed. A comparison with the simulation results from the previous chapter is also given.

In the last chapter 6, an example is given how the simulated data can be applied to improve the dose reading of the prototypes over the entire energy range. Then, areas in which further improvements are required are identified and suggestions for future activities are given.

2. Neutron dosimetry

This thesis deals with the *detection* of neutrons with a *dosemeter* for the purpose of *radiation protection*. As it is commonly known, neutrons interact with matter in a totally different way than charged particles, which renders their detection a complicated task. However, the *dose* that is caused by neutron radiation can be considerable in many cases. Generally, to measure doses (or the *personal dose equivalent*, see section 2.3 on page 21), dosemeters are used, which are often uniquely dedicated to a certain kind of radiation.

2.1. Typical sources of neutron radiation

Neutron radiation, i.e. radiation *fields* that are composed of neutrons, occur, as already mentioned, in various situations. There are many natural sources for neutrons, as these particles are common products of nuclear reactions. A prominent example is the (γ, n)-reaction; e.g. if deuterium (^2H or d) is hit by a gamma photon, a neutron can be produced:

$$^2H + \gamma \rightarrow ^1 H + n$$

This type of reaction is sometimes referred to as *nuclear photo effect*. ([28, 29, 30])

Another, even more well-known source of neutrons is *fission*. In nuclear power plants, the fact that in fission of ^{235}U neutrons are emitted is employed to keep up a chain reaction (which works since the fission is also triggered by neutrons itself, [31]). There are many isotopes that *decay* by *spontaneous fission*, e.g. ^{254}Cf, which is commonly used as a technical neutron source.

Neutrons can also be produced by the interaction of other particles with matter. There are numerous examples for this procedure; a technical application would be the production of neutrons with a *spallation source*. If for instance protons hit on a tungsten target, several neutrons are emitted. These neutrons can be directly produced in the nuclear reaction or be *evaporated* by the nucleus remaining after it, which commonly resides in a highly excited state and hence distributes its energy on the nuclei ([29, 28]).

Unlike α-particles, electrons or even protons, neutrons are not emitted as sole products of radioactive decays ([32]); i.e. there is no decay like $^AX \rightarrow^{A-1} X + n$. However, if ^AX is in an excited state after a β^--decay, the excitation energy can be transfered to a neutron leading to its release ([29, 28]). An example is the decay of ^{17}N:

$$^{17}N \rightarrow^{17} O^\star + e^- + \bar{\nu_e} \qquad ^{17}O^\star \rightarrow^{16} O + n$$

When it comes to radiation protection, both technical and environmental sources of neutrons play an important role. In the technical field, the most obvious example is *nuclear reactors*, since most of them are based on the fission of ^{235}U, as stated above. The *neutron spectrum*, i.e. energy distribution of the neutrons, is actually high energetic in that situation ([31, 29, 28]). However, in order to keep up a chain reaction, the neutrons emitted in the fission of uranium are moderated (e.g. with water) and thus thermalized.[1] It becomes obvious that a device which is designed to accurately measure neutron doses (that is, a dosemeter) must be able to work with very different neutron energies, even if it is to be applied in one situation only.

Another kind of facilities where prevention from neutron radiation is of concern is *medical treatment units* ([1, 2, 3]). Accelerators used there are capable of producing electrons with kinetic energies up to roughly 25 MeV, or protons with several times that energy. Interaction of those particles (or secondary photons, produced with a target for example) with the surrounding matter, i.e. the shielding of the facility, or the patient, can create neutrons up to very high energies, e.g. by the (γ, n)-reaction describe above. Indeed, care must be taken in medical facilities nowadays to shield neutrons as well as the actual treatment radiation.[2]

A natural source of neutron radiation which is nevertheless of interest in radiation protection is *cosmic radiation*. It accounts for a effective dose (see 2.3) of about 0.3 $^{\mathrm{mSv}}/_{\mathrm{a}}$ to the normal population ([33, 6]); for air crew staff, e.g. pilots, the average annual dose is much higher, at around 2.0 $^{\mathrm{mSv}}/_{\mathrm{a}}$, since the intensity of cosmic radiation depends on altitude very much ([5, 6, 33]). At a typical flight altitude of 10 km, the effective dose rate is roughly 5 $^{\mu\mathrm{Sv}}/_{\mathrm{h}}$; it originates from neutrons to about 50 ... 60 % ([5, 6]). The production of these particles from incoming high energetic protons (of which the *primary* cosmic radiation is comprised of by a huge part) can be a spallation reaction for example.

The neutron component of the secondary cosmic radiation has been a field of investigation by the HMGU for many years now ([9, 10]). So far, not only the dose caused by neutrons can be measured and even assessed to air crew members (with the EPCARD program,[3] [34, 35, 36]); also the energy spectrum is continuously measured by means of *Bonner Sphere Spectrometers* ([37, 38]) at the Zugspitze mountain ([9]) and on Spitsbergen ([10]). For the design of such an instrument, Monte Carlo simulations play an essential role as well ([39, 40, 41]). In the present work, the secondary cosmic radiation provided a field in which the HMGU dosemeter prototypes were investigated experimentally (section 5.3 on page 97).

2.2. Short description of neutron interactions with matter

Different kinds of particles show very different behaviors when interacting with matter. As it was mentioned above, neutrons do not interact with materials the same way as e.g. protons or alpha particles do. In the derivation of the *Bethe-Bloch-Formula*, the charge of the incident

[1] *Thermal* means a kinetic energy equivalent to the ambient temperature, i.e. about 25 meV
[2] J. Kratz (Klinikum Landshut gGmbH), private communication
[3] `http://www.helmholtz-muenchen.de/epcard-portal`

particle plays an essential role ([42, 19, 29, 28]). As neutrons are uncharged particles, it is clear that the energy loss they exhibit in matter is not due to direct ionization, nor due to bremsstrahlung. Instead, neutrons are referred to as *indirectly ionizing* particles ([43, 42, 19, 29, 28]). That is, their energy is transferred in single interactions only, which are denoted as *nuclear reactions*. The particles produced in those reactions can be of other type, and thus show again directly ionizing behavior.

In principle, four basic types of neutron interactions with matter can be identified:

- *Scattering* means that path and energy of the incident neutron are altered merely by a collision with a target nucleus. If that target is denoted as ${}^{A}X$, such a collision would be a nuclear reaction like ${}^{A}X\,(n,n)^{A}\,X$, i.e. the neutron that leaves the reaction is the same as the incident one. Its energy will in that case be only determined be kinematics, that is the scattering angle, the mass of ${}^{A}X$ and the incident energy. Thus, the scattering is *elastic*. *Inelastic* scattering occurs if the target nucleus resides in an excited state after the collision; the energy of the emitted neutron is in that case lower as in the elastic case due to energy conservation. A inelastic reaction is written as ${}^{A}X\,(n,n')\,{}^{A}X^{\star}$.
  In the elastic case, the kinematic treatment of the scattering process leads to a simple formula for the energy of the nucleus after the collision ([19, 42, 29, 28]):

$$E_X = E_n \cdot \frac{4 m_n m_X}{(m_n + m_X)^2} \cdot \cos^2\theta \tag{2.1}$$

  where m are the masses, E the energies after and before the collision respectively and θ the scattering angle. For the scattering on ${}^{1}H$ for example, it is evident that in forward direction, i.e. $\theta \approx 0\,^{\circ}$, virtually all of the neutron energy is transferred to the target, because of $m_{{}^{1}H} = m_p \approx m_n$. This relationship is applied in 3.3.1 on page 34.

- There are numerous nuclear reaction in a narrower sense in which the incident neutron vanishes and another type of particle is emitted instead. Those reactions are denoted for example (n,γ), (n,p), (n,α) etc., depending of course on the emitted particle. In some reactions the nucleus resides in an excited state afterwards; also, in various cases more than one particle can be emitted. An example for this behavior is ${}^{208}Pb$, where several neutrons are produced for an incoming one; e.g. ${}^{208}Pb\,(n,3n)\,{}^{206}Pb$ means that one neutron is captured, but three are emitted in that reaction.
  The energetic treatment of a nuclear reaction is governed by its specific *Q-value*. This quantity is defined as the difference in energy before and after the reaction,

$$Q = \left[\sum m^{(0)} - \sum m^{(1)}\right] c^2 \tag{2.2}$$

  which can of course be determined by summing of the involved masses ([29, 28]). The Q-value can be both positive or negative; in the case of $Q > 0$, the reaction is *exothermic*, which means that energy is released. For $Q < 0$, the reaction is called a *endothermic* or *threshold* reaction, because the energy consumed or converted to binding energy must be

brought in by the incident particle. If this energy does not suffice, that is for $E_n < |Q|$, the reaction does not occur.

- Another important way in how neutrons can interact with some materials is that they can trigger *fission*. The products of fission can be of various kind; usually, the target nucleus is divided into two smaller nuclei and a number of further neutrons, whose energy is distributed depending on the fission reaction. In nuclear power plants, the fission of uranium with thermal neutrons, i.e. $^{235}U\,(n,f)$ plays a key role ([31, 29]).

- Neutrons can also *activate* materials. In that case, a neutron gets captured by a target nucleus like in a nuclear reaction as stated above; however, the resulting nucleus then enters an excited, radioactive state with a certain half-life, which can be considerable. Thus, activation means induced radioactivity. A well-known activation product is ^{60}Co, which is produced in nuclear reactors via $^{59}Co + n \rightarrow {}^{60}Co$ and is used for medical applications. Neutron activation is also applied frequently in analyzing samples for trace elements. In the human body however, activation products can contribute to the dose a person gets from neutron radiation to a significant amount, for example because of the $^{14}N\,(n,p)\,^{14}C$ reaction that yields a radioactive isotope of carbon ([33, 43]).

As mentioned above, neutrons interact with matter not in a continuous way but in discrete steps. For each kind of target nuclei and each interaction process, the *cross section* defines the probability for the process to occur; there are for example scattering cross sections σ_{sc} or fission cross sections σ_f for each material, which are furthermore dependent on the neutron energy E_n. The *differential* cross section $\frac{\mathrm{d}\sigma}{\mathrm{d}\Omega}$ is proportional to the probability that the reaction product is emitted in a solid angle with direction Ω.

Cross sections are measured in *Barn*, with $1\,\mathrm{barn} = 1\,\mathrm{b} = 10^{-24}\,\mathrm{cm}^2$. If σ is multiplied with the density of target nuclei n, the result is called *macroscopic* cross section $\Sigma = \sigma \cdot n$. The inverse of this quantity is the so-called *mean free path* λ, which is the average distance neutrons of a specific energy can travel in a certain material without interacting in the denoted way. It is essential to note that the mean free path defines an average only; the track of a single neutron is inherently unpredictable, so the concept of cross sections does apply to a huge number of particles only. ([29, 28, 42, 19, 31])

The interaction probability for a given path length z is calculated by

$$p = 1 - \exp\left(-\frac{z}{\lambda}\right) = 1 - \exp\left(-n\sigma z\right) \tag{2.3}$$

For small values of z this equal to $p \approx n\sigma z = \Sigma \cdot z$. Thus it becomes evident that the probability of interaction rises with the length of a path a neutron travels in matter.

Monte Carlo simulations rely on a data set of cross sections for all processes and materials involved in order to create the probability distributions (like (2.3)) random numbers are then sampled from. A common database, not only for neutrons but other particles, is ENDF-B/VI ([44]), which contains cross section data up to a neutron energy of $E_n = 20\,\mathrm{MeV}$. For this

thesis, cross sections from ENDF-B/VI have been used and incorporated in the simulations (see chapter 4 on page 43).

2.3. Personal dosimetry with neutrons

2.3.1. Physical quantities for dosimetry

In radiation protection, the main quantities of interest are the so-called *personal* and *ambient dose equivalent*, which are both given in Sv (*Sievert*). Dose equivalent is a measured variable, unlike the well known quantity *effective dose*, which is calculated from the *absorbed dose* (in an organ or tissue) by applying radiation weighting factors (which yields the equivalent dose) and tissue weighting factors (yielding the effective dose). ([45, 13]) However, dose limits regulated by law usually refer to the latter; the personal and ambient dose equivalents are thus used as an estimate for the effective dose a person receives in a radiation field.

The ambient dose equivalent, $H^\star$, as it is defined by [46, 47], relates to a spherical phantom (the *"ICRU-Sphere"*) made of tissue-equivalent material; the depth in *mm* in the phantom at which the dose equivalent is taken is denoted in the symbol of the quantity; e.g. $H^\star(10)$ means an ambient dose equivalent for a depth of 10 mm. The personal dose equivalent H_p however refers to a $30 \times 30 \times 15\,\mathrm{cm}^2$ slab phantom of water. Here the depth in the phantom is given as well. Using a slab phantom, also the direction of the incident particles plays a role. The angle at which those hit the phantom surface is denoted in the quantity´s symbol. Thus, $H_p(10, 30\,^\circ)$ stands for the dose equivalent in a depth of 10 mm cased by radiation hitting the phantom at an angle of 30 °, for example. If no angle is given, 0 ° is to be understood.

The main objective of a personal neutron dosemeter is to measure the quantity $H_p(10)$ in a neutron radiation field. The dose associated with such a field can be calculated from its *fluence* Φ, which is the number of incident particles per cm^2. According to [46, 47], there is a linear relationship between neutron fluence and personal dose equivalent for radiation protection usage. The proportionality factor is $h_p(10) \equiv h_p \equiv h$:

$$H_p(10) = h \cdot \Phi \tag{2.4}$$

This *conversion coefficient* h is dependent on the neutron energy ($h = h(E_n)$); thus, if there is a broad spectrum, i.e. energy distribution, of the neutrons, the resulting dose must be calculated via[4]

$$H_p(10) = \int \mathrm{d}E_n h(E_n) \cdot \frac{\mathrm{d}\Phi}{\mathrm{d}E_n} \tag{2.5}$$

The dependence of $h = h_p$ and $h^\star$ on the neutron energy is shown in figure 2.1. Values up to $E_n = 20\,\mathrm{MeV}$ are tabulated in [46, 47]; for higher energies, the values published in [48] are used throughout this work. They are acquired using Monte Carlo simulations, just like the official conversion coefficients recommended by the ICRU. For the ambient dose, another factor $h^\star$

[4] Of course, for binned experimental data the integral in (2.5) is approximated by a sum.

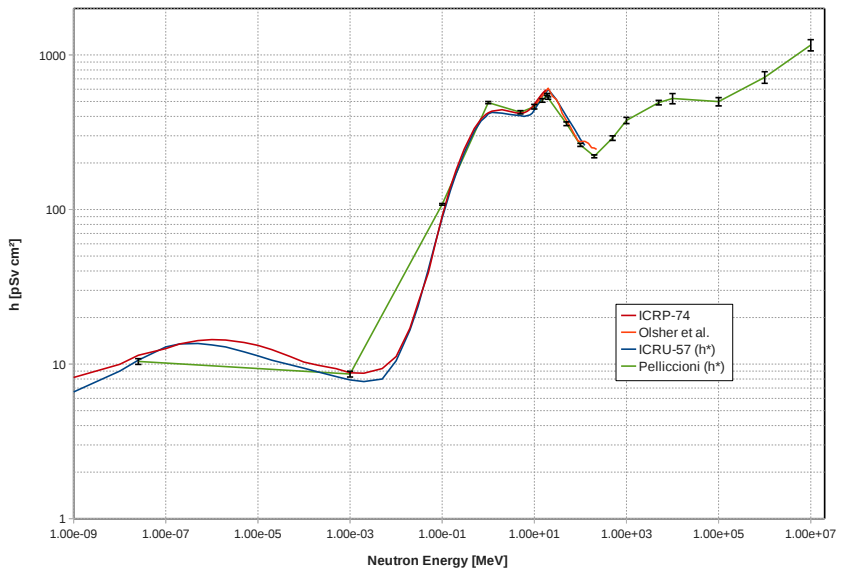

Figure 2.1.: Dependency of the fluence-to-dose conversion coefficients h_p and $h^\star$ on the neutron energy, according to *ICRP-74* ([46]), *Olsher et al.* ([48]) and *Pelliccioni* ([49]). For the latter, uncertainties are given; the three lower energies were calculated to demonstrate agreement with *ICRU-57* ([47]) only. Note that linear interpolation (on a logarithmic scale) was applied in between the calculated points.

is given in [46]; the values of h and $h^\star$ lie together closely over a wide energy range, which holds for the calculated values in [48] as well, serving as an indication for their correctness. For neutron energies of more than around $E_n = 250\,\mathrm{MeV}$, only values for $h^\star$ are available, which are given in [49]. In case conversion factors for such high energies are required in this work, i.e. for the secondary cosmic radiation in section 5.3, the values in [46, 47] and [48] are used as far as possible; above, $h^\star$ from [49] is taken as a substitute for h_p . This is justified since also at lower energies, the behaviors of the two different conversion factors and their dependencies on neutron energy is quite similar.[5]

2.3.2. Active personal neutron dosemeters

A dosemeter that is designed to work in neutron fields with various energies must account for the fact that these different neutron energies lead to different dose values per unit fluence. Thus, the *response,* i.e. the number of *counts* divided by the neutron *fluence*, should follow the energy dependence of the conversion coefficient shown in figure 2.1 ([11]). By that, the sensitivity with respect to dose (which corresponds to the number of counts per unit *dose* equivalent) can be kept constant. The measured dose can than be inferred from the count reading of the device by just applying an appropriate *calibration factor*.

[5] V. Mares (HMGU), private communication

Although various means of neutron measurement for active personal dosimeters are possible, for example tissue-equivalent proportional counters, CCD detector arrays, scintillators or superheated drop detectors ([11, 14]), the most commonly used technique is the operation of semiconductor *detectors* in pulse counting mode with different *converters*. The role of the latter is to create charged particles in conversion reactions triggered by the incident neutrons, as is described in more detail in section 3.1. In this thesis, a unit consisting of detector and adjacent converter is referred to as a *sensor*.

Using that kind of functional principle, the response of the device can be adjusted in order to exhibit a neutron energy dependence similar to the conversion coefficients (figure 2.1) by choosing an appropriate converter material. In many cases, more than one sensor is applied, so that the different sensors with accordingly different converters show responses distinct from one another´s, which leads to more possibilities for variation. By setting discriminators on the pulse heights, only an appropriate part of the signals in each sensor can be chosen for dose assessment, so that in many cases a good agreement between measured dose reading H^m and the reference $H^{ref} \equiv H_p(10)$ dose equivalent can be achieved. This however generally holds for a limited energy range only. Another common problem is the very low overall sensitivity of many dosemeters in the converter-detector design ([11]), leading to a high detection threshold. Another issue is the angular dependency of the dosemeter response, which may be of concern if very big sensors are used.

So far, electronic personal dosemeters based on one sensor ([50, 51, 52]), two sensors ([53, 54, 55]) and even three and more (like the HMGU prototype) have been developed ([11, 14]). A few devices also contain a separate sensor designed for the detection of photons so that photon fields can be taken into account in the dose reading H^m ([53, 55]). For pure neutron measurement, that contribution from photons (but also from other kinds of radiation) must be discriminated however, which is usually done by applying an appropriate threshold on the minimal signal height ([52]).

In recent years, many commercially available as well as prototype devices have been tested in several intercomparison measurement campaigns, e.g. [56, 57, 12, 15, 58, 3]. A huge variation in the overall response of the devices was reported. Furthermore, a very non-uniform response dependency on neutron energy could be discovered, which can still be regarded the main problem of neutron personal dosemeters. The ratio of measured and reference dose, i.e. $\frac{H^m}{H^{ref}}\big|_{E_n}$, reaches a value of $\frac{H^m}{H^{ref}}\big|_{E_n \approx 1\,\mathrm{eV}\ldots 10\,\mathrm{keV}} \approx 10\ldots 100$ at low neutron energies from about 1 eV to 10 keV for some devices. Moreover, a common drawback is a decreased sensitivity at around 100 keV to 1 MeV, where values as low as $\frac{H^m}{H^{ref}}\big|_{E_n \approx 0.1\ldots 1\,\mathrm{MeV}} \approx 0.01$ are observed. Since this energy region is of high importance for many thinkable applications of neutron dosemeters, including nuclear industry and medical treatment facilities, that point is a weighty issue.

Due to the fact that in most technical and environmental fields the neutrons are not monoenergetic but possess a (possibly wide) energy distribution, over- and underestimates of the dose due to $\frac{H^m}{H^{ref}}\big|_{E_n} \neq 1$ are considered to compensate if the deviation of the ratio from unity

is not too high ([2]). A ratio of $\frac{H^m}{H^{ref}} = 1 \pm 0.3$, as it is required for photons ([59, 13]), is however not considered necessary nor achievable for neutrons. Instead, deviations of a factor two in actual dose measurements in non mono-energetic fields are regarded sufficient ([13, 12, 50]). The HMGU neutron dosemeter, which is described in detail in the next chapter, is designed to accomplish that goal. In the present work, possibilities for a significant improvement of the $\frac{H^m}{H^{ref}}$ uniformity over a very wide energy range are developed.

3. The HMGU neutron dosemeter

Since 1999, a neutron dosemeter has been developed at the Helmholtz-Zentrum München. It is an *active* dosemeter, i.e. an electronic device. Thus, the mentioned advantages of electronic dosemeters apply here; for example, if a person who is working in a radiation filed is wearing the device, it can display the dose that has already been acquired, as well as the current dose rate caused by the field. *Limits* can be set for both quantities; in that case, the dosemeter would give an acoustical warning if either dose or rate went too high. Although the device, being an electronic one, needs a battery power supply, measurement times up to two weeks can be achieved, which is enough for almost all kinds of applications.

In order to measure neutrons of various energies with a high enough sensitivity, the device is equipped with four neutron *sensors*, that are explained in detail in section 3.3. Each sensors has its own amplifier and the digital electronics (based on a MSP430 micro-controller) following the corresponding analogue one deals with counting, storage and display of the measured quantities. The principle of the analogue circuits is treated roughly in the next section.

3.1. Working principle of the sensors

The four *sensors* the HMGU neutron dosemeter is equipped with each consist of a Silicon semiconductor *detector* and a *converter*. Those two parts are essential for the efficient detection of neutron radiation; the converter is made of a material incoming neutrons interact with, creating charged particles (ions) via nuclear reactions or scattering. The choice of converter material and dimensions determines the behavior of the sensitivity with respect to the neutron energy to a great extent ([22, 24]). The principle of neutron detection by means of such a converter is depicted in figure 3.1. It is also shown that the purpose of the detector, i.e. the Silicon diode, is to count the charged particles created by the reaction of neutrons in the converter. (Of course, neutrons can also interact with the detector material, i.e. Silicon, itself, creating charged particles there. The impact of this effect is discussed in section 4.1.2 on page 51.)

If a charged particle enters the *sensitive volume* of the Silicon diode, it deposits energy there, which is mainly due to ionization. Thus, *electron-hole-pairs* are created. They account for a *charge* $Q_{created}$, which is proportional to the energy deposited by the particle, i.e. $Q_{created} \propto E_{dep}$. An *electric field* is applied to collect this charge (see section 3.2 on page 29); this field corresponds to a certain *bias* or *depletion voltage* U_D across the active zone of the detector. In the case of the HMGU dosemeter, this voltage is $U_D = 9\,\mathrm{V}$. The movement of the electrons

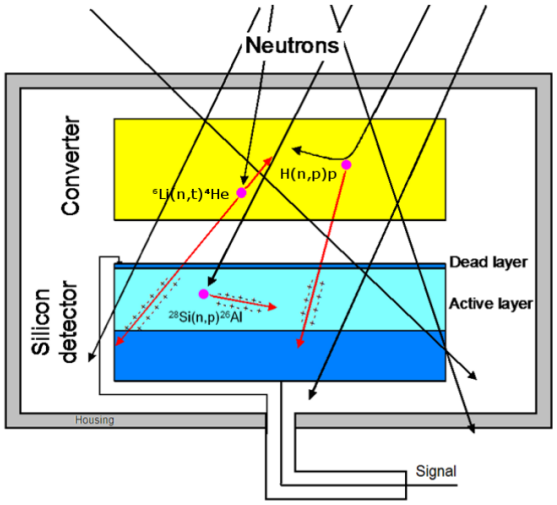

Figure 3.1.: Working principle of the neutron sensors based on converter and Silicon detector (from [25])

and holes in the electric field leads to a voltage drop U_{Drop}, since the detector can be seen as a capacity C_D. Thus, the voltage drop is given by that quantity via

$$U_{Drop} = \frac{Q_{coll}}{C_D} \tag{3.1}$$

where Q_{coll} denotes the fraction of the deposited energy that is actually collected and thus contributes to the signal U_{Drop}. Here, a proportionality

$$Q_{coll} \propto Q_{created} \propto E_{dep} \tag{3.2}$$

between the two charge values is assumed; however, the fraction

$$\frac{E_{coll}}{E_{dep}} \equiv \frac{Q_{coll}}{Q_{created}} \tag{3.3}$$

of the collected energy E_{coll} and the deposited energy in general depends on the *charge collection efficiency (CCE*, see section 3.2 on page 29) and thus the energy of the particle in question.

The principal electronic circuit employed for each sensor of the dosemeter is shown in figure 3.2. Through a resistor, the detector capacitor C_D is recharged after a voltage drop, so that in steady state 9 V are applied at it. The drop itself constitutes the *signal*, which is transferred to *preamplifier, shaper* and *post-amplifier* through a further capacitor. This chain of amplifier and shaper is designed in order to get a signal or *pulse height* proportional to the originally collected charge, that is the collected energy. For this, a characteristic *shaping time* can be set, which is 10 μs for the *Fast* and *Albedo* sensors and 60 μs for the *Delta* sensors[1] (see section 3.3).

[1] M. Wielunski (HMGU), private communication

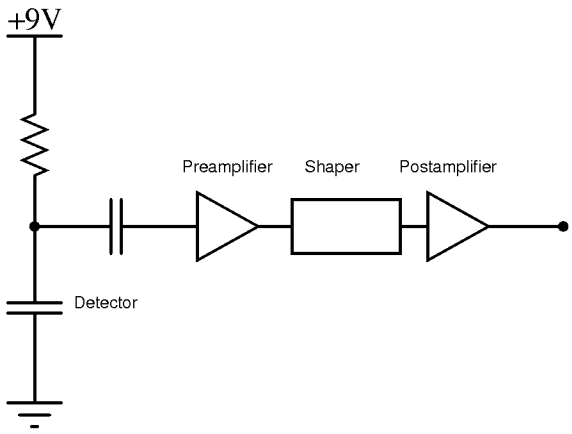

Figure 3.2.: Analogue electronic circuit used for the detectors

The different output levels of the shapers are then matched by adjusting the amplification factors of the post-amplifiers.

The pulse height, which results from the electric circuit shown in figure 3.2 is considered proportional to the collected charge; the latter is equivalent to the collected energy, since for a single electron-hole-pair $E_{eh} = 3.6\,\mathrm{eV}$ must be deposited on average. Thus,

$$\text{Signal or pulse height} = \alpha \cdot \frac{E_{coll}}{E_{eh}}$$

where α is the amplification of the whole circuit, which is the same for each of the sensors. Because of the proportionality, the signal is denoted E_{coll} in this work.

The sensors in the neutron dosemeter work in a *pulse counting mode*. That is, not the signal height itself is taken into account for dose assessment, but only the number of counts from each sensor (i.e., no pulse height spectrum is acquired). Such a *count* is registered by the (digital) electronics if the signal E_{coll} is higher than a certain *threshold* value E_{thresh}, i.e. $E_{coll} > E_{thresh}$. This value differs among the detectors and has a great influence on the counting efficiency. The main reason for applying a threshold is to either distinguish between different effects leading to a certain signal (as applied with the Delta sensor, see section 3.3.2 on page 35), or to suppress signals from incident gamma particles, i.e. photons. Clearly, a neutron dosemeter should measure only the neutron component of a given radiation field and be unaffected by photons or other particles. In order to separate those photon signals, the thresholds must be set to rather high energies. It can be shown experimentally ([59]) that for the threshold values currently applied for the dosemeter, gammas contribute only at very high dose rates, because then pile-up events play a crucial role (see below). By means of Monte Carlo simulation, the threshold necessary to prevent gamma contribution can be estimated as well. The figure on page 88 for example shows a pulse height spectrum that was

Sensor	Channel	E_{thresh}
Fast	15.77	1000 keV
Albedo	16.15	1000 keV
Delta D1	42.85	2800 keV
Delta D2	—	3500 keV
Delta G1	41.62	2800 keV
Delta G2	—	3500 keV

Table 3.1.: Threshold setting for the different sensors, i.e. the average channel number and the energy this is considered to correspond to (according to [25])

simulated for photons with $E_\gamma = 4.5\,\mathrm{MeV}$ incident on one of the sensors of the dosemeter. The procedure to create such a spectrum by simulation and appropriate analysis is described in detail is chapter 4. Here, it is only necessary to state that no events with a signal higher than $E_{coll} \approx 800\,\mathrm{keV}$ have occurred; the main contribution stems from events with $E_{coll} \lessapprox 600\,\mathrm{keV}$. As 4.5 MeV is a fairly high photon energy, it can be considered safe if the thresholds are set to $E_{thresh} > 800\,\mathrm{keV}$, since the signals caused by lower energy gammas will not exceed this value.

Practically, the thresholds for the sensors are applied by using *comparators* on each sensor, which are devices that compare the output of each amplifier with a certain reference voltage U_{thresh} that is proportional to the threshold energy E_{thresh}. This voltage can be set to various discrete *channels*, of which one roughly spans 60 keV. To find the desired channels for each sensor, an edge in the pulse height spectrum of the Albedo and Delta sensors is employed, which is located at $E_{coll} = 2.73\,\mathrm{MeV}$ (see section 3.3.2 on page 35). By varying the channel number and comparing the counts that can be measured with that particular threshold setting, the channel corresponding to that edge can be determined. Other values can then be set by just scaling the channel according to the desired energy. The procedure of setting the thresholds of the HMGU dosemeter is covered in detail in [25]. Table 3.1 gives the aimed threshold setting for all sensors of the dosemeter, along with the corresponding channel. The Delta sensors have two thresholds each, so that there are six different count values to be considered. In this work, the Delta sensors with threshold settings 1 and 2 will be referred to as "Delta 1 sensor" and "Delta 2 sensor" respectively, if the the context is clear.

As mentioned above, *pile-ups* can play a role if the fluence rate of the radiation field is very high. In that case, it can happen that two events occur, i.e. two neutrons hit a sensors and create charged particles in the converter, in a very short time interval. If this time is in the order of the shaping time (see above), the two events cannot be distinguished by the electronics. That is, not the individual energies $E_{coll}^{(1)}$ and $E_{coll}^{(2)}$ are taken into account, but a combination of them, which is (for very short times) roughly their sum, i.e. $E_{coll} \approx E_{coll}^{(1)} + E_{coll}^{(2)}$. The behavior of the dosemeter is affected by such pile-up events in two different ways:

- If both events on their own would have been below the counting threshold, $E_{coll}^{(1)} < E_{thresh}$ and $E_{coll}^{(2)} < E_{thresh}$, but the resulting pile-up event is no longer, i.e. $E_{coll}^{(1)} + E_{coll}^{(2)} >$

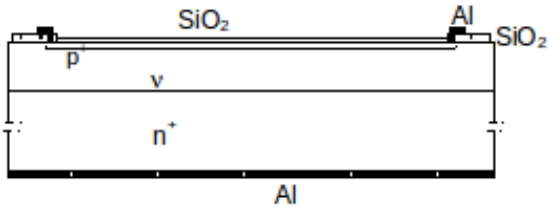

Figure 3.3.: Design of the Silicon PIN-diodes used as detectors (from [24]). The thickness of the structure is about 400 μm, the one of the ν-layer about 50 μm.

E_{thresh}, an additional count is registered, which may enhance the response of the sensor in an undesired way.

- If the single events would have been above the threshold, $E_{coll}^{(1)} > E_{thresh}$ and $E_{coll}^{(2)} > E_{thresh}$, clearly the resulting one is also, but in that case only one count is registered instead of two, which lowers the response of the sensor.

Since a pile-up event can occur only if both single events, i.e. incoming neutrons, are counted, the frequency of pile-ups strongly depends on the overall sensitivity of the sensors. For a dosemeter, only a very little fraction of the incident particles have to be detected; the probability of detecting two at virtually the same time becomes small then. Thus, the problem of pile-ups occurs at very high dose rates only when measuring neutrons, as shown experimentally as well in section 5.1 ([18])

3.2. Characteristics of the semiconductor detectors

As shown on page 26 already, the *sensors* of the neutron dosemeter consist of *converters* and *detectors*. These detectors are the same for all four sensors, so the sensors differ only in their converter and threshold setting (see section 3.1). The detectors applied here are Silicon PIN-diodes, i.e. semiconductor detectors ([60, 19, 45, 42, 61]).

The term PIN-diode denotes the principal structure of this type of detector: P means a layer with very high *p-type doping*, I stands for a *intrinsic* layer with only small dopant concentration and N is a layer with *n-type doping*. The design is shown in figure 3.3 and is denoted as p^+-ν-n^+; that is, the intrinsic layer (ν) is of very little doped n-type. The area of the detectors is $A = 200\,\mathrm{mm}^2 \pm 1\,\%$ each.

The important quantities in order to understand the behavior of the detectors, i.e. the thicknesses and resistivities of the layers, are given in table 3.2. The overall thickness of the detector is about 400 μm; the n^+-type bulk is ca. 350 μm, whereas the active ν-zone is around 50 μm. Unlike in conventional semiconductor devices, the ν-layer is imposed onto the bulk by *epitaxial growth* ([24, 60]), resulting in a very steep gradient in dopant concentration at the interface. The p^+-layer is created via diffusion of boron acceptor atoms. At that interface, the width of the transition is not exactly known; however, as the whole layer is about 1 μm only, it can be be considered a sharp interface as well.

Layer	Thickness	Dopant concentration	Resistivity
p^+	$d_p \approx 1\,\mu\text{m}$	$N_A \geq 1.0 \cdot 10^{19}\,\text{cm}^{-3}$	$\rho \leq 0.45\,\text{m}\Omega\text{cm}$
ν	$d_\nu \approx 50\,\mu\text{m}$	$N_D \leq 1.5 \cdot 10^{12}\,\text{cm}^{-3}$	$\rho \geq 3\,\text{k}\Omega\text{cm}$
n^+	$d_n \approx 350\,\mu\text{m}$	$N_D \geq 2.2 \cdot 10^{17}\,\text{cm}^{-3}$	$\rho \leq 0.02\,\Omega\text{cm}$

Table 3.2.: Thicknesses and resistivities of the PIN-diode layers ([24])

Considering the resistivities (that yield the dopant concentrations) and the dimensions of the layers, the electric field in the detector can be calculated. For the purpose of this thesis, only a simplified one-dimensional model with sharp transitions and uniform doping within the layers needs to be considered, which can be treated according to [60, 19, 42, 61, 62]. Of particular interest is the width of the *depletion zone*, i.e. the zone over which the potential difference U_D is applied. In this zone, the electrical field $\boldsymbol{\epsilon}$ caused by that difference drives the collection of the charge carriers [62, 63, 64], which contribute to the signal (see section 3.1). However, due to the huge differences in doping and the sharp transitions between the layers, the electrical field does not reach far into the n^+ bulk of the detector, yielding a very thin depletion zone with the thickness of the ν-layer $d_\nu \approx 50\,\mu\text{m}$. This can be proven by measuring the capacity of the detector with various bias voltages U_D, as shown in [24]. The resulting behavior of C_D with respect to U_D is also displayed in figure 3.4. It shows that at a certain voltage, the capacity reaches a saturation value and does not change anymore when the voltage is raised. At that point, the detector is *fully depleted*, which means that the depletion zone cannot be extended further because of the steep gradient in resistivity at the ν-n^+-interface. The resulting width can be calculated from a basic formula, assuming that the detector can be considered a parallel plate capacitor with width d_ν:

$$d_\nu = \epsilon_r \epsilon_0 \cdot \frac{A}{C_D} \tag{3.4}$$

Taking the appropriate values for A, ϵ_r (relative permittivity of Silicon, [42, 19]) and $C_D \approx 430\,\text{pF}$ (from the figure), one obtains $d_\nu \approx 47\,\mu\text{m}$, which fits very well to the estimated value, i.e. the thickness of the ν-layer. The bias voltage $U_D = 9\,\text{V}$ was of course taken in order to yield a fully depleted detector.

Although the electric field inside the biased diode does not extend further than the ν-layer thickness, the *sensitive volume* of the detector is not restricted to this zone. That is because charge collection can occur from outside the depletion volume as well, so that the signal height (which is proportional to the collected charge, see section 3.1) cannot be determined from the energy deposited in the depletion layer alone. The sensitive volume is thus defined as an effective volume in which the deposited energy does actually contribute to Q_{coll}. Applying relationship (3.3) for a certain amount of charge produced by an energy deposition E_{dep} at a certain location in the detector, the ratio $\frac{E_{coll}}{E_{dep}}$ of the energy contribution to the signal and

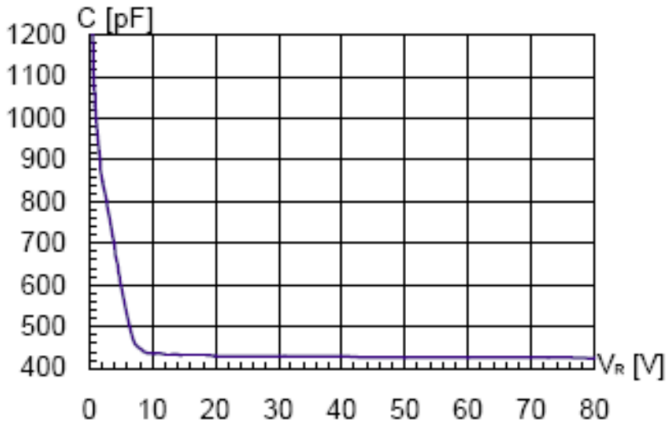

Figure 3.4.: Dependency of the the PIN-diode capacity $C_D \equiv C$ on the bias voltage $U_D \equiv V_R$ (from [24]). At about $U_D = 9\,\mathrm{V}$, a saturation value of $C_D \approx 430\,\mathrm{pF}$ is reached.

this deposition is defined as the *charge collection efficiency* (CCE) ϵ_q:

$$\epsilon_q = \frac{E_{coll}}{E_{dep}} = \frac{Q_{coll}}{Q_{created}} \tag{3.5}$$

This general definition holds for any volume and shape. In the case of the detector, one can assign a CCE which is dependent on *depth* z below the p^+-layer surface, i.e. $\epsilon_q = \epsilon_q(z)$, because of the epi-planar design (i.e. only edge effects affect the CCE in xy-direction, which can be neglected for a simplified treatment).

The dependence of the charge collection efficiency on z is governed by three processes. The most important one that drives the collection of produced charge is *drift in the electric field* $\boldsymbol{\epsilon}$; in that case, charge carriers move with an average drift velocity $v_{drift} = \mu \cdot \epsilon$ given by the electric field and the *mobility* of the electrons μ_e or holes μ_h ([60]). Drift is a very fast process, which means that in regions where charge collection occurs mainly due to drift, almost all carriers contribute to the signal. The CCE can then be set to one, i.e. $\epsilon_q = 1$. Generally, it can be assumed that in the depletion zone of a detector, the charge collection happen due to drift because of the electric field present there ([63]). Thus, in the first ca. $50\,\mu$m below the detector surface, the CCE is $\epsilon_q = 1$, with a drop behind this region.

In the following zone, the charge collection is dependent on two other processes, which are *funneling* and *diffusion*. The *funneling* phenomena is a consequence of the *depletion region collapse* following the hit of an charged particle onto the detector. In that case, a potential difference across the bulk region builds up, which leads to a current of minority charge carriers. Funneling has been investigated thoroughly for several types detection devices ([65, 66, 63, 62, 67]). Refined models exists for this process and are incorporated in device simulation tools; for this work however, an empirical treatment of the funneling effect is sufficient. Considering the charge collection due to funneling, a drop of ϵ_q within several micrometers can be assumed.

What is important to notice is that behind the depletion zone, funneling is aligned with

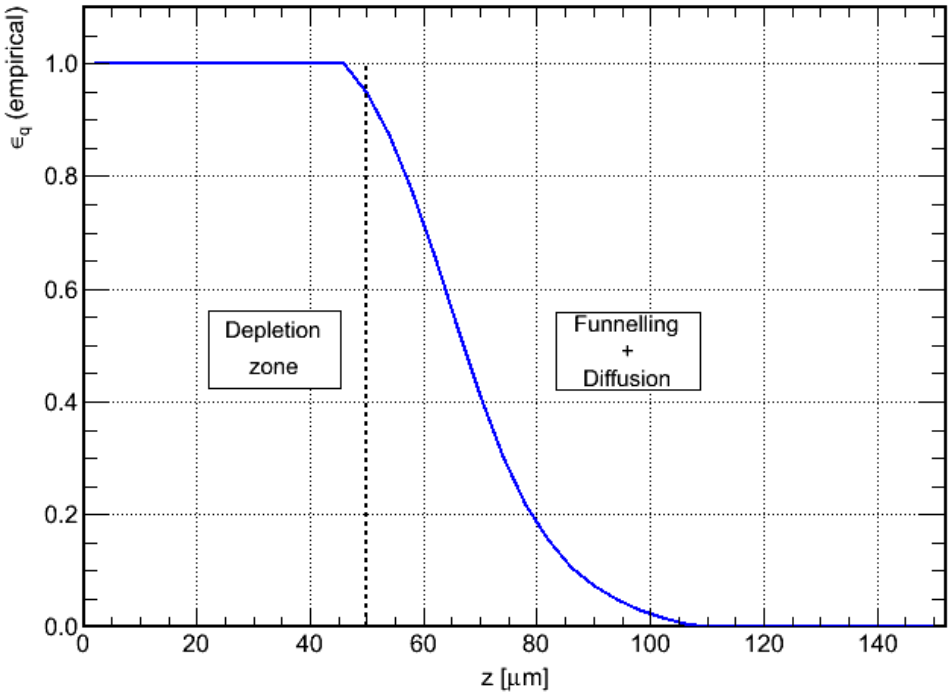

Figure 3.5.: Charge collection efficiency $\epsilon_q = \epsilon_q(z)$ assumed for the Silicon detectors; the collection processes and depletion zone width are indicated

diffusion. This process is well understood and must always be taken into account when treating the movement of charge carriers in semiconductor devices. The spread of an amount of charge Q due to diffusion leads to a current $\boldsymbol{j}$ given by

$$\boldsymbol{j} \propto D \cdot \boldsymbol{\nabla} Q \tag{3.6}$$

where D is the *diffusion constant*. It is connected to the mobility μ via the so-called *Einstein relation* ([60, 42]).

Funneling and diffusion can be assigned characteristic lengths, which are dependent on the devices dimensions, the process's effectivity to collect charge and of course to charge collection time, which is the shaping time here (see section 3.1). The funneling length can be several micrometers, whereas diffusion can account for charge collection over several 10 μm ([67, 62]).

For this thesis, an purely empirical model of the dependency of ϵ_q on z was used; it is shown in figure 3.5. As stated above, $\epsilon_q\,(z \lessapprox 50\,\mu\text{m}) = 1$ because of drift; at $z > 50\,\mu$m, funneling and diffusion are modeled with a drop of ϵ_q to zero within another ca. 50 μm. The exact behavior of the CCE was taken to fit the *partial charge collection peak* observed when measuring with the *Fast* sensor (see section 4.1.1 on page 44).

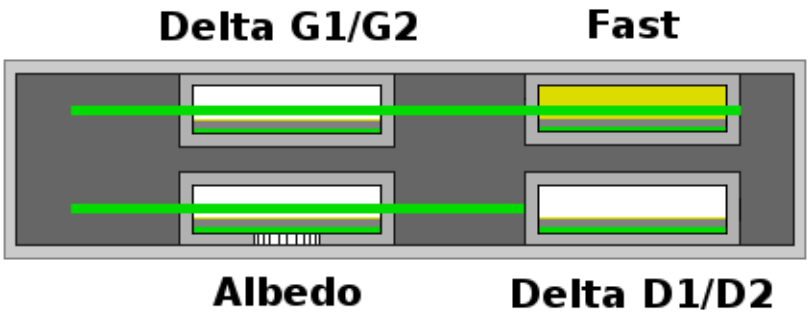

Figure 3.6.: Overview of the positions of the four sensors in the dosemeter head. The positions of the circuit boards are indicated in green, the converters in yellow. The filling of the measurement head with B_4C is drawn in dark gray. The Delta G1/G2 sensor is positioned above the Albedo one, whereas the Fast is behind the Delta D1/D2 (see projections in figure 4.1).

3.3. Design of the dosemeter

As stated in section 3.1 already, the HMGU neutron dosemeter consists of four neutron *sensors*. Each of these is comprised of a Silicon PIN-diode, the *detector*, as described in the previous section, and a *converter*. The main difference between the sensors is, besides the composition of the converter material and its thickness, the *threshold* setting, i.e. the minimal amount of collected charge in order to generate a *count*. This threshold equals a certain amount of collected energy E_{thresh}, so that the collected energy E_{coll} must exceed this value (see section 3.1 above).

The four sensors of the dosemeter are denoted as *Fast* (F), *Delta* (D or G) and *Albedo* (A). There are two Delta sensors, which are equal in design but at different positions in the dosemeter casing (figure 3.6). The reason for this is the threshold setting for the Delta sensors, which lead to a very low sensitivity ([25, 21], see below); the second sensor is thus to improve statistics. However, there are plans to replace one of the Delta sensors by a gamma detector head and thus design a combined photon-neutron-dosemeter ([24, 59]). Therefore, the second sensor was previously (e.g. in [24, 25]) called *Gamma* sensor. Of course, here the term "Gamma" means not a real γ-detector but merely the position reserved for it. For the sake of clarity, in this thesis both Delta sensors are referred to as "Delta", but with indices D and G if a distinction is required.

As shown in table 3.1 on page 28 already, for each of the Delta sensors two thresholds are applied. This would be possible for Fast and Albedo as well yielding values for F1, F2, A1 and A2 (see section 5.2.1). So far however, only one threshold has been necessary for these sensors, so six count values in six sensors (if D2 and G2 are considered separate sensors) are

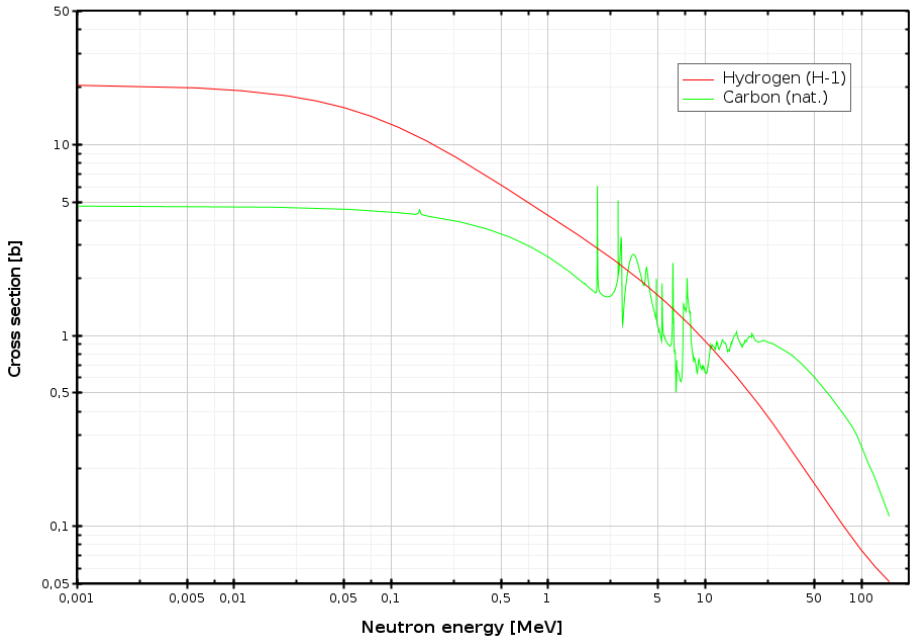

Figure 3.7.: Cross sections for elastic scattering of neutrons on Hydrogen and Carbon ([44])

used for dose assessment.

3.3.1. Fast sensor

As the name suggests, the *Fast* sensor is designed to measure fast neutrons; here, the term "fast" denotes neutrons with a kinetic energy E_n of more than 1 MeV. This value is determined by the threshold setting applied here, which is $E_{thresh} = 1\,\mathrm{MeV}$. As the comparator channel corresponding to that threshold cannot be assigned directly from measuring an edge in the pulse height spectrum (see sections 3.1 and 3.3.2), the channel number is usually set to the one applied for the Albedo sensor ([25]). This procedure is described in section 3.3.3 on page 39.

The material used as a converter for the Fast sensor is *polyethylene*, i.e. $(CH_2)_n$. It is imposed onto the Silicon detector as a wax; the whole converter has a thickness of around 2.5 mm. The reaction applied for neutron conversion here is *elastic scattering* (see section 2.2). That is, the two processes ${}^1H\,(n,n)\,p$ and ${}^{12}C\,(n,n)\,{}^{12}C$ play a main role.

For elastic scattering, the energy of the reaction products is totally governed by the kinetic energies of the incident particles, i.e. the neutrons. In the case of elastic scattering on hydrogen ${}^1H$, the recoil *proton* (that is, the Hydrogen ion) gets an energy which for forward scattering is almost equal to that of the original neutron. This can easily be seen from equation (2.1) using $m_n \approx m_p$. For scattering on Carbon nuclei, i.e. ${}^{12}C$, the energy transfer to the outgoing ion is smaller. However, also Carbon plays a role for neutron detection with the Fast detector. This is due to the energy dependence of the cross sections involved here, which is shown is figure 3.7. Besides the fact that the cross sections for both scattering reactions drop with

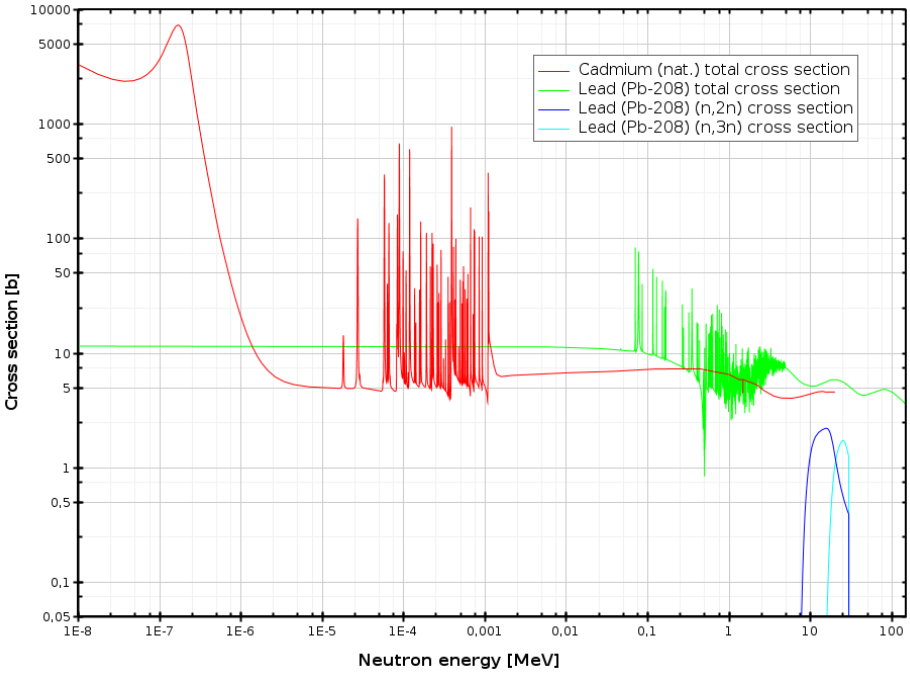

Figure 3.8.: Total cross sections for the reactions of neutrons with Lead and Cadmium and cross sections for the reactions $^{208}Pb\,(n,2n)\,^{207}Pb$ and $^{208}Pb\,(n,3n)\,^{206}Pb$ ([44])

increasing neutron energy, one can see that for $E_n \gtrapprox 10\,\mathrm{MeV}$ the scattering on Carbon is more likely than on Hydrogen. So, for very high energy neutrons, the Carbon content of the converter material plays an important role.

The housing of the Fast sensors, in which both converter and detector, as well as an Aluminum substrate, is contained, consists of Lead with a thickness of about 1 mm. This material was chosen in order to shield off photons and scattered radiation. In figure 3.8, the cross section of Lead for the reaction with neutrons is shown. Over a wide energy range, it stays around $\sigma_{Pb} \approx 10\,\mathrm{b}$; in the region of 0.1 MeV to 5 MeV, resonances occur, which are not important for the dosemeter design. At around 10 MeV however, neutron multiplication reactions like $(n,2n)$, $(n,3n)$ etc. set in. Those reactions enhance the number of neutrons hitting the converter of the Fast sensor and thus improve its sensitivity at those high energies.[2]

3.3.2. Delta sensors

As stated above, the HMGU dosemeter is equipped with two *Delta* sensors. Those sensors are equivalent in their design, but placed at different positions within the dosemeter head (see figure 3.6). Both sensors are provided with a Lithium converter of roughly 200 μm thickness. The Lithium is bound in the form of LiF powder which is dissolved in glue. When the glue is brought onto the detector, the solvents evaporate, leaving a layer of dried glue with the

[2] M. Wielunski (HMGU), private communication

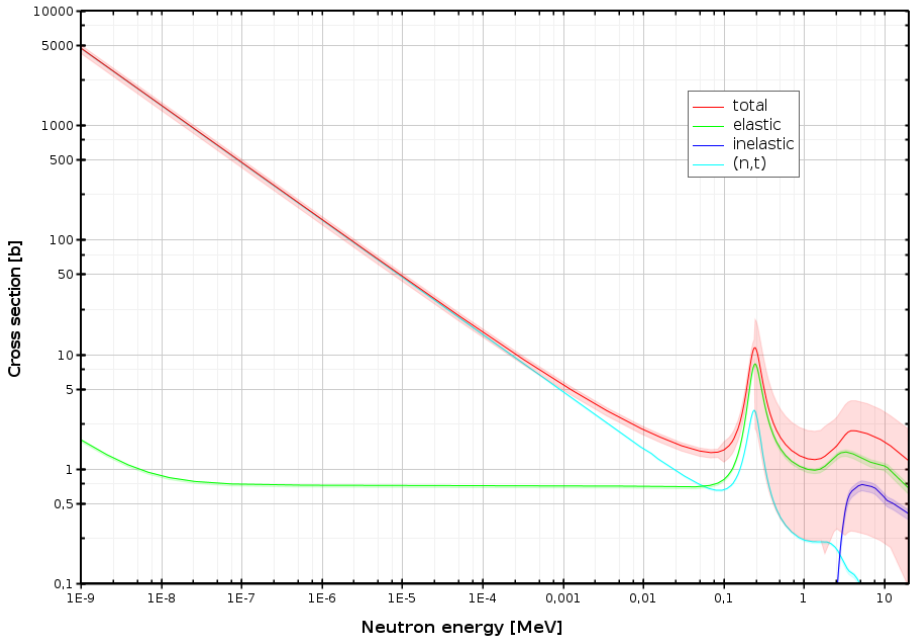

Figure 3.9.: Total cross section and cross sections for different reaction channels occurring in the reaction of neutrons with ^6Li ([44])

converter material in it. The density of the dissolved LiF is about half of the solid one.[3]

Unlike the polyethylene converter of the Fast sensors, the Lithium converter employs a nuclear reaction for the creation of charged particles. With the ^6Li isotope, neutrons can interact via the reaction $^6Li\,(n,\alpha)\,^3H$, i.e.

$$^6Li + n \rightarrow {}^3H + {}^4He \tag{3.7}$$

The Q-value of this reaction is $Q = 4.784\,\text{MeV}$ ([20, 44]). For a description of the Q-value see section 2.2. The cross section for the reaction (3.7) is shown in figure 3.9. One can see that the behavior of the cross section is dominated by the (n,t) reaction up to energies in the keV regime. For an efficient neutron conversion, however, the number of target nuclei must be enhanced, since natural Lithium has an abundance of ^6Li of 7.4 % only. For the use as a converter, the Lithium is enriched to an ^6Li abundance of about 96 %.

From (3.7), one can see that the reaction products of the conversion reaction with neutrons are tritium t, i.e. the Hydrogen isotope ^3H, and an alpha particle α, i.e. ^4He. With the Q-value, the energy distribution of the outgoing particles can be calculated. In the non-relativistic case, the so-called Q-value-equation ([28, 29]) can be applied; for the tritium product in the above

[3] M. Wielunski (HMGU), private communication

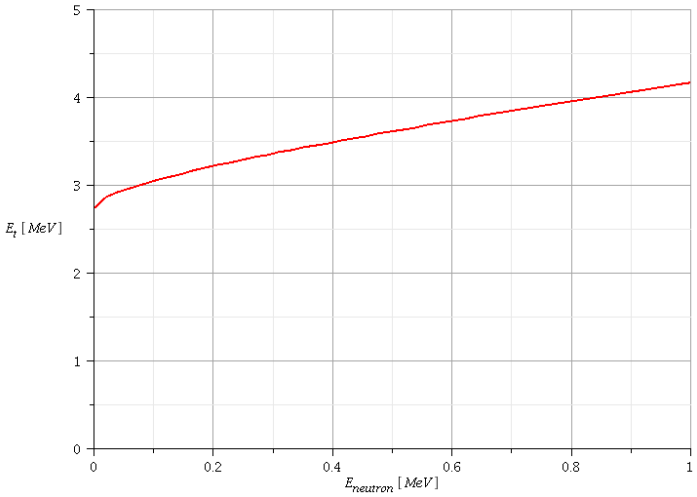

Figure 3.10.: Dependency of the kinetic energy E_t of a Hydrogen ion emitted in forward direction in the reaction (3.7) on the energy of the incident neutron $E_n \equiv E_{neutron}$; calculated according to equation (3.8)

reaction, this equation reads

$$\sqrt{E_t} = \frac{\sqrt{m_n m_t E_n}}{m_t + m_\alpha} \cos\theta + \sqrt{\frac{m_n m_t E_n}{(m_t + m_\alpha)^2} \cos^2\theta + \frac{m_\alpha Q + E_n (m_\alpha - m_n)}{m_t + m_\alpha}} \tag{3.8}$$

In the case of $E_n \to 0$, the term depending on the scattering angle θ vanishes, and the energy of the tritium is solely determined by the masses and the Q-values:

$$E_t \overset{E_n \to 0}{=} \frac{Q \cdot m_\alpha}{m_t + m_\alpha} \tag{3.9}$$

The situation described by equation (3.9) is very well fulfilled when the neutrons are of thermal energies, i.e. $E_n \approx 25\,\text{meV} \ll Q$. In that case, the energy of the tritium is $E_t \approx 2.73\,\text{MeV}$; the alpha particle energy can be calculated by the same equation yielding $E_\alpha \approx 2.05\,\text{MeV}$.

For a non-vanishing neutron energy, however, the energy of the reaction products can considerably exceed the above values. In the case of forward scattering, the tritium energy dependency on the incident neutron energy is shown in figure 3.10. One can see that even for $E_n > 100\,\text{keV}$, E_t becomes higher than 3 MeV already. The Delta sensors are designed to exploit this *Delta effect*. To achieve that, the first threshold for the Delta is set to $E_{thresh,1} = 2.8\,\text{MeV}$; thus, although the reaction cross section for (3.7) is high at thermal energies, only neutrons with a high enough energy are counted by those sensors ([25, 21]). A second threshold is set at $E_{thresh,2} = 3.5\,\text{MeV}$. This constitutes the fact that for each Delta, virtually two sensors D1/G1 and D2/G2 are considered. For the dose assessment, the difference between the to counts values, i.e. $(D_1 + G_1) - c \cdot (D_2 + G_2)$, is taken (see section 3.4 on page 40).

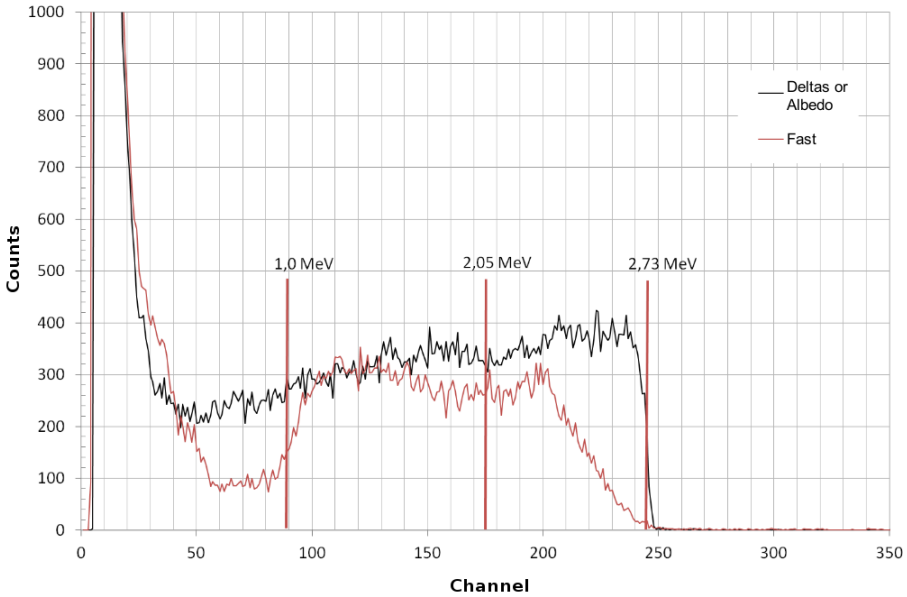

Figure 3.11.: Shape of the pulse height spectra obtained with PE converter (Fast) and LiF converter (Delta, Albedo) (from [25]). The spectra were taken by measurement with an AmBe source and at the PTB, respectively. The position of the edge used for threshold determination is indicated; also, the threshold energy for Fast and Albedo $E_{thresh} = 1\,\mathrm{MeV}$ is shown. Note that the channel numbers given here do not translate to those given in table 3.1 (change in design).

To determine the comparator channel corresponding to $E_{thresh,1}$ and $E_{thresh,2}$, thermal neutrons are used. They are produced with a Americium-Beryllium (AmBe) source as fast neutrons and thermalized by polyethylene layers. According to equation (3.9), tritium ions with a kinetic energy of $E_t \approx 2.73\,\mathrm{MeV}$ are then emitted in the converter of the Delta sensors. As the range of tritium particles at that energy is lower than the thickness of the sensitive zone of the underlying detector, all of the energy is deposited and collected, yielding a signal $E_{coll} \approx 2.73\,\mathrm{MeV}$. Since particles that are emitted not in forward direction do not receive the full kinetic energy of 2.73 MeV but less, this value constitutes an edge in the pulse height spectrum of the sensors, as shown in figure 3.11. By varying the comparator channel and comparing the corresponding count rates, the position of this edge can be determined. The threshold values $E_{thresh,1}$ and $E_{thresh,2}$ are then set accordingly. The whole procedure of threshold setting with the HMGU dosemeter is covered in detail in [25].

The casing of the Delta sensors is made of Cadmium. The cross section of this material for the reaction with neutrons is shown in figure 3.8. In general, the Cadmium cross section is below the one for Lead, which is used for the Fast sensor. For thermal energies below 1 eV however, one can see the so-called *Cadmium edge*, which is a rise in the cross section of more than two orders of magnitude. This effect efficiently shields off thermal neutrons, partly preventing problems with pile-ups (see section 3.1) that could occur in very low energetic neutron fields with a high fluence rate.

3.3.3. Albedo sensor

The design of the *Albedo* sensor is very similar to that of the Delta sensors described in section 3.3.2. The geometry and material of the converter is quite the same, i.e. it is a LiF converter based on the nuclear reaction (3.7) of neutrons with the isotope ^6Li. To enhance the reaction rate, the abundance to this isotope is enriched to 96 %. The converter is imposed onto the detector by using a LiF powder that is dissolved in glue.

Unlike the Delta sensors that are designed to count intermediate energy neutrons, the Albedo sensor is for measuring the thermal neutron component of a field. Thus, not only the reaction products exceeding a certain kinetic energy (2.8 MeV for the Delta sensors) are counted, but a bigger amount of the tritium and alpha particles produced via (3.7). In figure 3.11, the pulse height spectrum yielded by the sensors with Lithium converter is shown. Since the plateau below 2.73 MeV comes from particles with E_t or E_α less than that energy, detecting those is possible by simply setting the threshold energy E_{thresh} to a lower value. For the Albedo sensor, $E_{thresh} = 1\,\text{MeV}$ was chosen, like for the Fast sensors described in section 3.3.1. As mentioned there, for that sensors the comparator channel corresponding to 1 MeV is not possible to be determined via measurement. This becomes clear from figure 3.11, as the pulse height spectrum of the Fast does not display a sharp edge. For the Albedo however, determining the channel corresponding to 2.73 MeV is possible as described in section 3.3.2 and [25]; the channel for 1 MeV is then set accordingly, both for the Fast and Albedo sensors.

Figure 3.9 on page 36 makes it obvious that the reaction $^6Li\,(n,\alpha)\,^3H$ is very well-suited to convert low-energy neutrons, as there is a steep rise in cross section down to thermal energies. However, an unaltered Albedo detector whose response followed the behavior of the cross section would cause a too high sensitivity at this energy ([25]). Thus, two measures are taken to alter the response in order to yield a better overall behavior. First, a the housing of the Albedo sensor is made of Cadmium, as for the Delta sensors. The Cadmium edge shown in figure 3.8 on page 35 shields off huge parts of the thermal neutrons. In order to enable some of them to still enter the sensor after all, a circular hole with 5 mm in diameter is left in the casing. This hole is placed at the back side of the sensor; that is because thermal neutrons are usually scattered back from a phantom during measurement, or from the body if the dosemeter is worn. Thus, the casing is designed for shielding off thermal neutrons entering from the front side and enabling them to enter from the back.

The second measure to prevent a too high response to thermal neutrons is to fill the dosemeter head with Boron-carbide B_4C. The cross section for the reaction of neutrons with the two main Boron isotopes is given in [44]. The interaction with ^{10}B, which has a abundance of around 20 % in natural Boron, has a very high cross section whose behavior is similar to that of reaction (3.7), i.e. it rises for lower neutron energies. By filling the dosemeter with Boron, a part of the thermal neutrons that would still enter the sensor can be captured. The whole procedure of filling is described in detail in [25].

3.4. Dose assessment

The *dose reading* of the HMGU dosemeter is calculated by taking into account to number of *counts* by each of the sensors. According to section 3.1, a count is registered if the signal height (that is, the collected energy E_{coll}) exceeds a certain *threshold* value E_{thresh}. For the Fast and Albedo sensors, one threshold setting is applied each, yielding the count numbers $F_1 \equiv F$ and $A_1 \equiv A$. For each of the Delta sensors, two thresholds are applied, yielding the values D_1, D_2, G_1 and G_2. The so far estimated threshold values for the various sensors are summarized in table 3.1 on page 28.

As mentioned in section 3.3.2 already, for the dose assessment from the Delta sensors, the difference in their count values is taken. This yields a value referred to as *Intermediate counts*, I, which is

$$I = (D_1 + G_1) - c \cdot (D_2 + G_2) \tag{3.10}$$

That is, the counts obtained with the threshold setting $E_{thresh,2} = 3.5\,\mathrm{MeV}$ are weighted with a constant c and subtracted from the counts given by the threshold setting $E_{thresh,1} = 2.8\,\mathrm{MeV}$. Since $E_{thresh,2} > E_{thresh,1}$, the relationship between the count numbers is $(D_1 + G_1) < (D_2 + G_2)$. Depending on the constant c however, the whole term (3.10) can become negative. In that case, the Delta sensors are "switched off", i.e. the value I is set to $I = 0$ by the dosemeter software.

The reason for this behavior is that for high energy neutrons, the influence of the threshold value becomes smaller; thus, the number of counts in D_1/G_1 and D_2/G_2 approaches each other. At the same time, however, the total number of counts in the Delta sensors rises, because more particles receive a kinetic energy higher than the threshold value. At $E_n > 1\,\mathrm{MeV}$, the Fast sensor begins to detect neutrons (see section 3.3.1); thus, those high energy neutrons would be counted twice. The deactivation of the Delta sensors is in order to prevent that problem. Whether this happens is governed by the value of c and the mean energy of the neutron field. Currently, $c = 2.2$ is used, which has been determined at measurements with mono-energetic neutrons at the Physikalisch-Technische Bundesanstalt (PTB).[4] Of course, this value was taken to yield an accurate dose reading in these fields. In mixed fields including low and high-energetic neutrons, however, the deactivation of the Delta sensors causes problems. In those cases, the high-energetic component of the spectrum leads to the switch-off, preventing the intermediate energy neutrons (which can account for a substantial amount of the total fluence and dose) from being counted. Thus, it can happen that in a situation where non mono-energetic neutron spectra are measured, the dose is underestimated by the dosemeter. This is also shown with the measurement taken for the present work, which are presented in chapter 5.

Once the number of the intermediate counts $I \geq 0$ is determined, the complete dose reading H^m ("measured dose") is calculated by the dosemeter software. For that, appropriate *calibration factors* k_i are multiplied with the counts in the Fast and Albedo sensor and with the

[4] M. Wielunski (HMGU), private communication

constant	value
c	2.2
k_1	$0.16\,\mu$Sv
k_2	$0.0256\,\mu$Sv
k_3	$9\,\mu$Sv

Table 3.3.: Factors for dose assessment using equations (3.10) and (3.11) [25, 15]

intermediate counts; the results are then summed yielding H^m:

$$H^m = k_1 \cdot F + k_2 \cdot A + k_3 \cdot I \tag{3.11}$$

If the Delta sensors are switched off, $I = 0$ in (3.11), so that the dose reading is calculated from F and A only.

Like the value for c, the calibration factors in equation (3.11) have been determined by means of measurements. Both irradiations at the PTB ([15]) and with the AmBe source at the HMGU ([25]) have been done. The factors used so far are given in table 3.3.

Using simulated data as obtained in chapter 4, not only the threshold values but also these calibration factors can be optimized, yielding a higher uniformity of the dose reading in regions where no (mono-energetic) measurements can be conducted. This enhances the accuracy of the dosemeter by a great extent. Suggestions for new factors and thresholds are given on page 118.

4. Simulation of the neutron dosemeter

One of the major tasks in the present work is to *simulate* the HMGU neutron dosemeter. Generally, simulation stands for a computationally intensive calculation of the behavior of a system. In the case of a dosemeter, the main quantity of interest is the response of the device to a given neutron fluence; by means of simulation, this quantity can be calculated, along with all necessary data that are needed to grasp the behavior of the response. Thus, simulation provides a deep understanding of the physical and technical processes involved in the functioning of the device.

For the simulation of the HMGU dosemeter, the *Monte Carlo method* is applied. The general features of this computational tool are described in supplement A. In order to make use of this method, a generic Monte Carlo framework, GEANT4 [26, 68, 69], is used, which is covered in A.1 on page 135.

Monte Carlo simulations have already been applied to investigate the sensors the dosemeter is equipped with; this is described in [21, 20]. There, the Monte Carlo codes MCNP [70] and TRIM [71] were utilized. In this work, the focus of the simulations is different, and thus GEANT4 was chosen because it offers great flexibility and accuracy.

Generally, simulations conducted for this work have two distinct aims. First, they are designed to *reproduce* measured data. In order to achieve this, an as exact as possible emulation of the system, i.e. the dosemeter or its sensors, had to be implemented. By studying the evolution of the simulation results with the variation of the system parameters, it was possible to identify the main influences on the device´s behavior and thus gain a better understanding of its reading. Moreover, the reproduction of experimental results serves as a validation of the simulations. This is very important, because the second aim of the calculations conducted with GEANT4 was to *acquire data* that can be used to investigate *improvements* of the dosemeter. In this thesis, data from neutron energies not accessible via measurements was simulated, serving as a basis of some ideas of improvement presented in section 6.1 on page 113.

The two steps necessary to achieve the mentioned goals, i.e. the *acquisition* of *pulse height spectra* and the *calculation* of *response functions* for all sensors of the dosemeter, are described in the next sections. Details on the implementation of the simulation programs as well as a short general description of the GEANT4 framework are provided in supplement A.

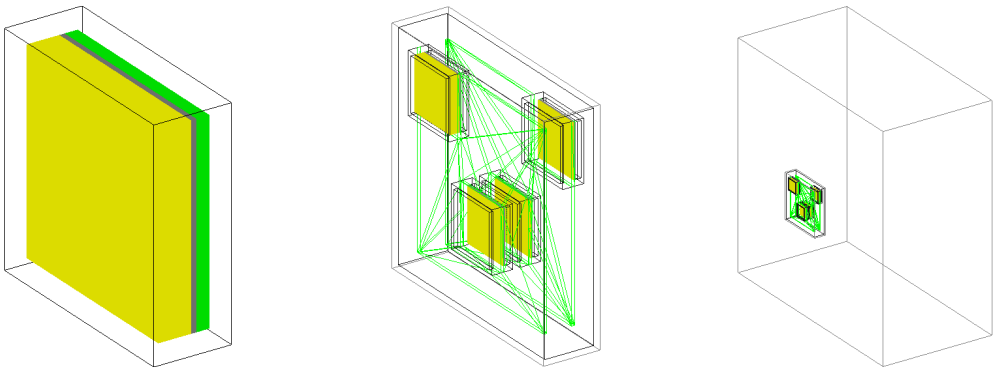

(a) Single sensor (Fast) (b) Complete dosemeter (c) Dosemeter on phantom

Figure 4.1.: Views of the different kinds of geometry used in the simulations, created with the GEANT4 OpenGL renderer ([27])

4.1. Determination of pulse height spectra

To simulate the HMGU dosemeter, i.e. to acquire pulse height spectra for the various sensors and to calculate the response from them, several simulation programs with the GEANT4 framework were created. The design of the applications was as described in supplement A.2. In general, three different kinds of geometry setups were incorporated: the single sensors, the whole dosemeter and the dosemeter attached to a plexiglass phantom (see figure 4.1).

For the simulations of the single sensors, the geometry consisted of the (Lead or Cadmium) housing, with a *converter* and a *detector* on a substrate placed in it, as shown in figure 4.1a. For a characterization of the sensors see section 3.1. The layered design of the detectors utilized in order to account for the CCE (figure 3.5 on page 32) is described in supplement A.3.

The purpose of the single sensor simulations was to gain an understanding of the physical processes creating signals in the sensors. Thus, the *Fast*, the *Delta* and the *Albedo* sensors are treated independently. The simulation results are described in terms of the acquired pulse height spectra in the following subsections.

4.1.1. Simulation of the Fast sensor

The *Fast* sensor was the first part of the HMGU dosemeter simulated in this work. The geometry was designed to emulate the real sensor. That is, the converter thickness was 2.5 mm; the thickness of the Lead housing was 1.0 mm, and the detector was assembled from 200 layers of Silicon with 2.0 μm each. For simulation purpose, the sensor *area* was not restricted to $A = 200\,\mathrm{mm}^2$, since this quantity does not alter the acquired pulse height spectrum, as it is scaled by the number of neutrons hitting the sensor according to (A.3).

For the beam, mono-energetic neutrons of $E_n = 1.5 \ldots 100\,\mathrm{MeV}$ were used, as well a energy *spectrum*. The latter was the spectrum of the *HMGU AmBe source*, which is an Americium-Beryllium neutron source ([72]). The energy distribution of that source, which was also used

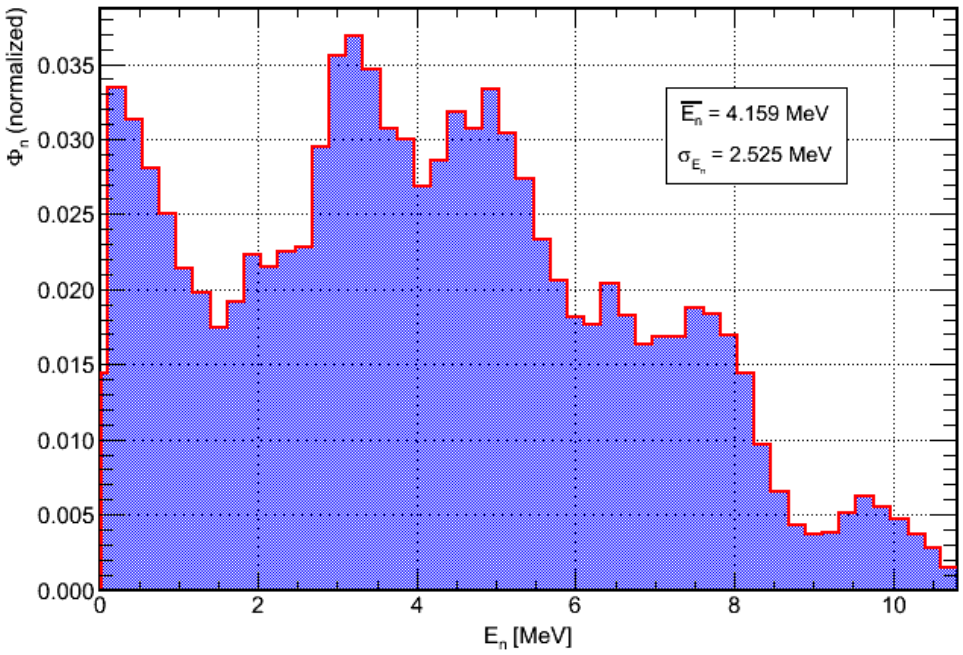

Figure 4.2.: Spectrum of the AmBe source of the HMGU ([72, 73, 25]), normalized to one

for measurements (see section 5.2 on page 91), is shown in figure 4.2. It is a rather high energetic spectrum with a mean energy of $\bar{E}_n = 4.159\,\mathrm{MeV}$ and a maximal neutron energy of around $E_n \approx 11\,\mathrm{MeV}$. Here, a normalized binned distribution is available. In order to use the spectrum as a input for the simulations, a batch file was created that looped over the energy bins and started simulations with appropriate event number according to the fraction of the total fluence in the particular bin. Since the figure shows a normalized spectrum, applying a certain fluence corresponds to just scaling it with the desired value.

The resulting pulse height spectrum from those simulations is shown in figure 4.3. The green histogram gives the result for a simulation as described above, with only the sensor implemented (and $27 \cdot 10^6$ incident neutrons on the sensor area), whereas the red line, for comparison, shows the result for a simulation of the Fast sensor in the whole dosemeter (with $6.75 \cdot 10^6$ neutrons on the sensor area, hence the lower resolution).

Here, the influence of charge collection behind the depletion zone described in section 3.2 can be seen clearly. Without accounting for that effect, that is with a CCE dependency on depth z below the detector surface given by

$$\epsilon_q(z) = \begin{cases} 1 & z < 50\,\mu\mathrm{m} \\ 0 & z \geq 50\,\mu\mathrm{m} \end{cases}$$

the energy collection spectra correspond to the dotted lines in the histogram 4.3. When using a charge collection model as given in the figure on page 32, the shape of the pulse height

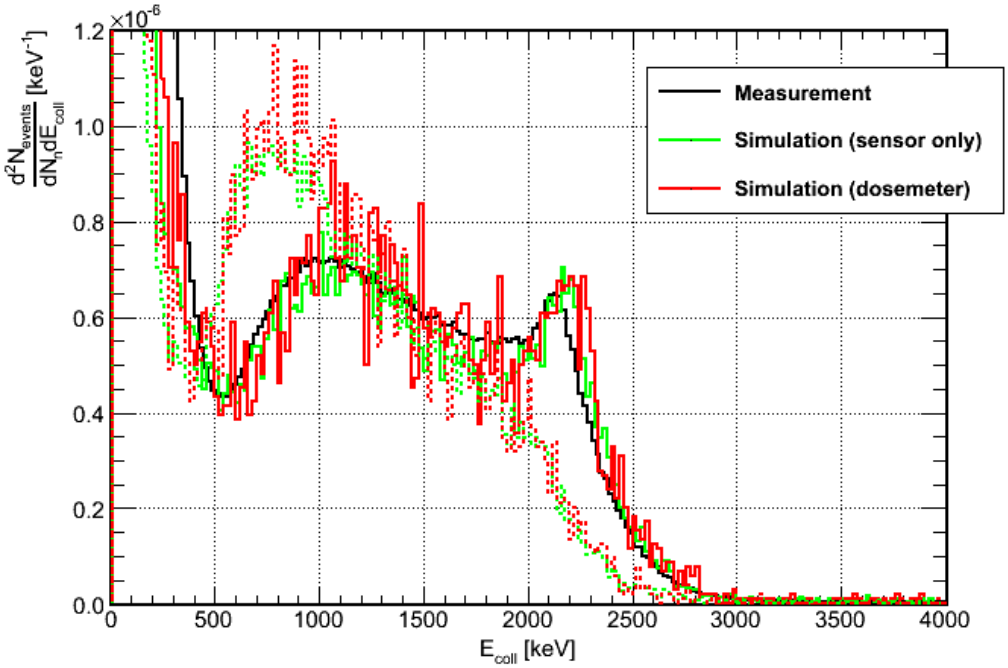

Figure 4.3.: Simulated and measured pulse height spectra of the Fast sensor and an AmBe source. The dotted lines show the spectra without the CCE being taken into account.

spectrum is quite different; the whole histogram is shifted to higher energies, and a peak around $E_{coll} \approx 2.2\,\mathrm{MeV}$ occurs. This is the *partial charge collection peak*, which stems from the fact that with the CCE given in figure 3.5 on page 32, a signal height $E_{coll} \approx 2200\,\mathrm{keV}$ can be achieved with protons incident under 0°. This situation is shown in figure 4.4, which is a plot of the collected energy E_{coll} versus the energy of *protons* E_p entering the detector perpendicularly. As these are the particles that are produced in the polyethylene converter of the Fast sensor (see section 3.3.1), the frequency of events with E_{coll} in a certain interval can be inferred from figure 4.4 given a spectrum of proton energies at the detector surface. (Such a study has been done in [22, 20, 21].) One can see that with the CCE assumed for the dosemeter simulations, the partial charge collection peak occurs for protons with $E_p = 2 \ldots 3\,\mathrm{MeV}$; with charge collection in the $\nu-$layer alone, only a small energy interval around $E_p \approx 2\,\mathrm{MeV}$ leads to a maximal energy collection, which is less than about 2 MeV. Thus, no peak occurs in the pulse height spectrum, and the energy collection is shifted to lower values in that case. This is of course because for a sharp transition in the CCE, the collected energy decreases rapidly once the proton range is so long that the *Bragg peak* (where most of the energy is deposited) lies behind the depletion zone. Instead, if the Bragg peak is only shifted to a zone with $\epsilon_q \lesssim 1$ (and decreasing very gradually), the collected energy is higher, which is exactly what is depicted in the figure.

For non-perpendicular incident of the protons, which is of course the case when using the

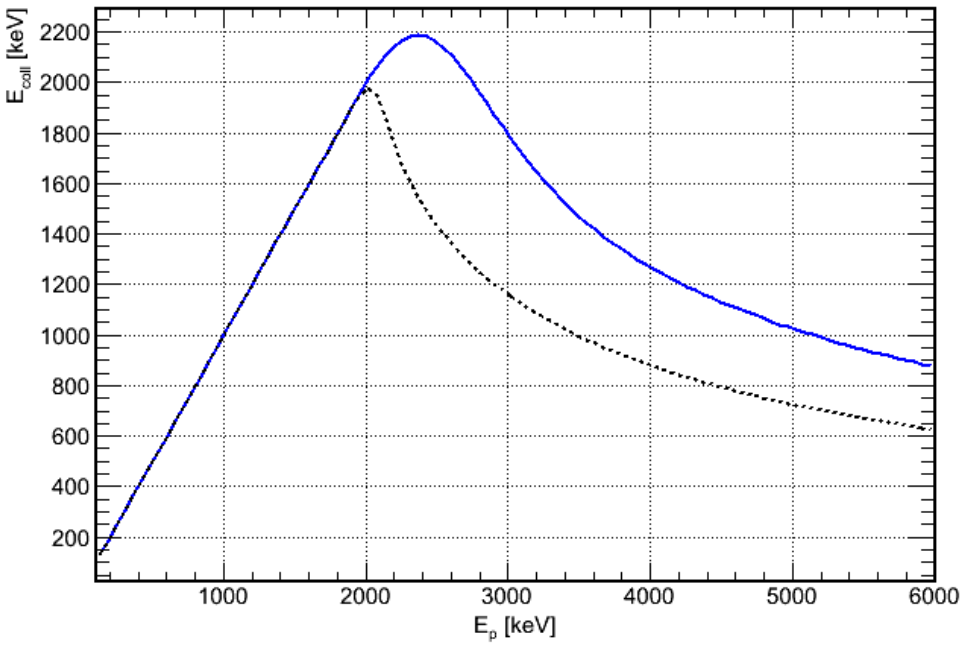

Figure 4.4.: Energy collection in the Silicon detector, i.e. signal height E_{coll}, as a function of incident *proton* energy E_p. The blue line corresponds to the CCE shown in figure 3.5; the dotted line shows the energy collection in the depletion zone alone.

described converter-detector combination, the energy collection can exceed the one than given in figure 4.4 due to a higher energy deposition within the active zone because of the longer path length. Of course, this leads to events with $E_{coll} \gtrapprox 2\,\mathrm{MeV}$ and $E_{coll} \gtrapprox 2.2\,\mathrm{MeV}$ in the pulse height spectra on the facing page for charge collection in the depletion area only and with the CCE model applied, respectively.

As a comparison, also a *measured* spectrum,[1] that was created with an AmBe source as well, is shown in figure 4.3. One can see that also in the measurement, a partial charge collection peak occurs around the given energy. The measured and simulated histograms fit very well if charge collection behind the depletion zone is accounted for in the analysis as described in this thesis.

The mechanism of partial charge collection was further studied with four simulations of the Fast sensor in a dosemeter geometry and $E_n = 1.5\,\mathrm{MeV}$, $E_n = 2.0\,\mathrm{MeV}$, $E_n = 2.5\,\mathrm{MeV}$ and $E_n = 3.7\,\mathrm{MeV}$ as incident neutron energies. The obtained pulse height spectra from irradiations of the sensor with $25 \cdot 10^6$ neutrons of each energy are shown in figure 4.5. Here, the CCE model given by in figure 3.5 was applied in the analysis of course. One can see that for the two lower energies, no peak occurs, which is simply due to the fact that in this case the energy of the emitted protons is completely in the linear range of figure 4.4, i.e. $E_p \leq 2\,\mathrm{MeV}$. For $E_n = 2.5\,\mathrm{MeV}$, a small peak at the predicted energy of around $E_{coll} \approx 2.2\,\mathrm{MeV}$ is observed,

[1] M. Wielunski (HMGU), private communication

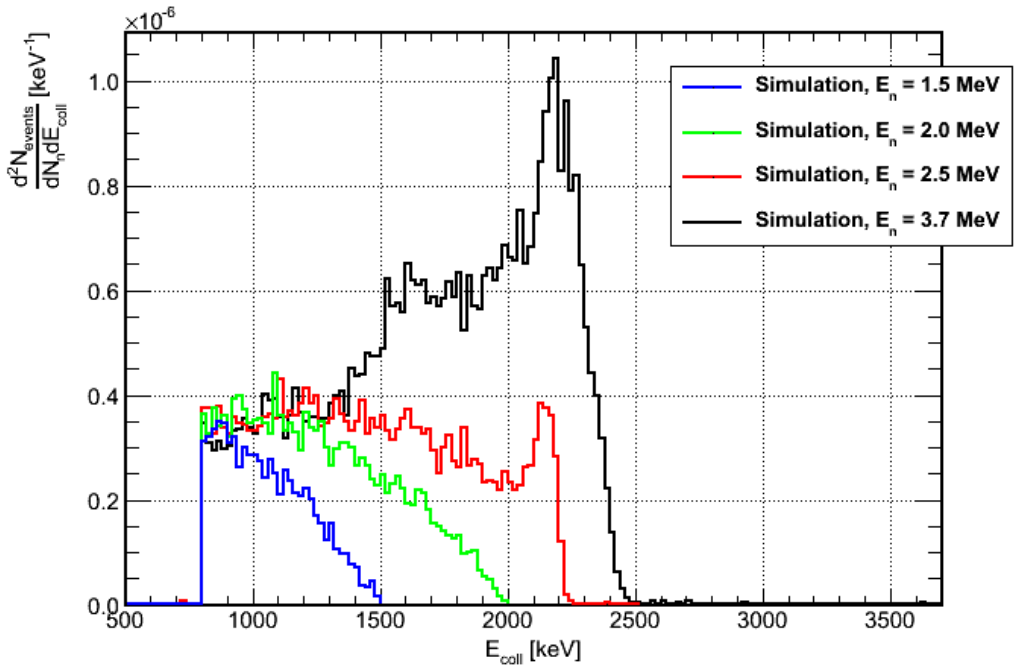

Figure 4.5.: Simulated pulse height spectra of the Fast sensor in the dosemeter geometry with neutron of energies $E_n = 1.5 \ldots 3.7\,\mathrm{MeV}$

which becomes more evident at the highest shown neutron energy. The fact that the pulse height spectra given in figure 4.5 show only very few signals at $E_{coll} \leq 800\,\mathrm{keV}$ is due to the cut-off applied here for the purpose of memory saving (see supplement A.2).

The two simulation results depicted in figure 4.3, for the sensor only and the whole dosemeter, already suggest that the surrounding of the Fast sensor has very little influence on the shape of its pulse height spectrum and its response. This is also shown in figure 4.6, where three different geometries are used for the simulations with an incident neutron energy of $E_n = 100\,\mathrm{MeV}$. The number of events was $500 \cdot 10^6$ (incident on the whole geometry). The first result (green line) shows, just like above, the pulse height spectrum for the sensor alone, and the second one (red line) for the sensor inside a dosemeter geometry. The third result is for the same sensor in another geometry which corresponds to the *demonstration device* described in former works concerning the HMGU dosemeter ([23, 21, 20, 24]). One can see that only for very small signal heights, a slight difference in the spectra occur. For $E_{coll} > 1000\,\mathrm{keV} = E_{thresh}$, i.e. for signals creating a *count* (see section 3.1), the differences are negligible.

Another result of the simulation with $E_n = 100\,\mathrm{MeV}$ is that the shape of the energy collection spectrum is quite different between the energy of the AmBe source and that energy. This is because with a polyethylene converter, three kinds of events result in a energy deposition in the Silicon detector; there is elastic scattering on Hydrogen, elastic scattering on Carbon and nuclear reactions of neutrons in the Silicon detector itself (see section 2.2). As already shown in figure 3.7 on page 34, the cross sections for scattering decrease with increasing neu-

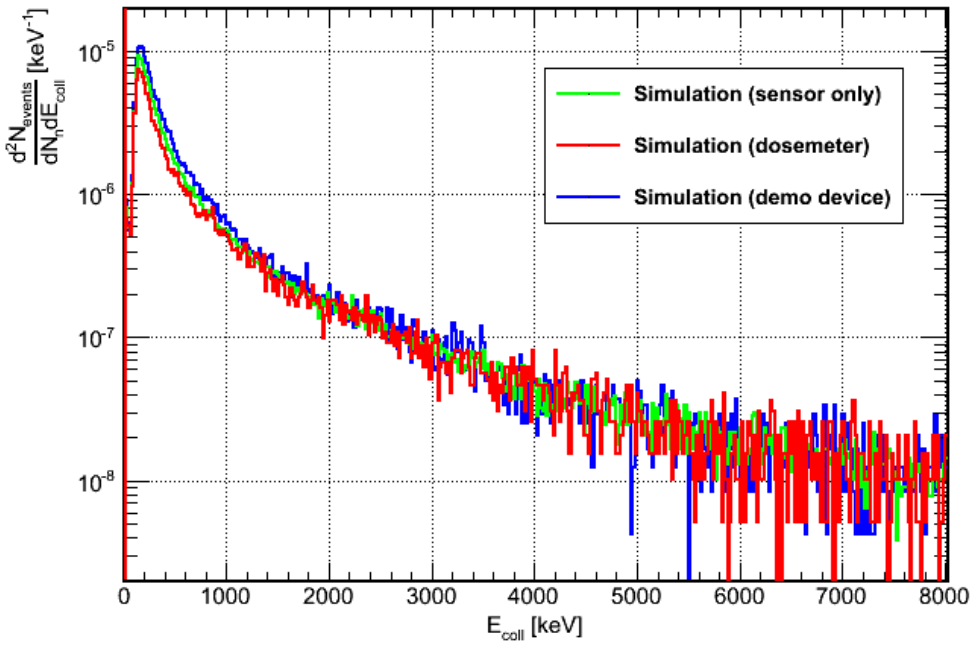

Figure 4.6.: Simulated pulse height spectra of the Fast sensor with 100 MeV neutrons and three different geometries

tron energy; for $E_n \gtrapprox 10\,\text{MeV}$ however, the cross section for scattering on Carbon is higher than for the reaction with Hydrogen. For the AmBe spectrum with $\bar{E}_n = 4.159\,\text{MeV}$ (figure on page 45), the scattering on protons is the dominant effect; for 100 MeV, even though the amount of C in polyethylene is half of the H amount, scattering on Carbon is more important. Those C ions receive less kinetic energy in the scattering process than protons due to their higher mass (equation (2.1)), but are able to deposit their energy in a shorter path because of their higher stopping power. Thus, the energy collection resulting from those processes is higher than for protons, too. The Hydrogen ions that are still produced have higher energies than with the AmBe source because of the higher incident neutron energy. According to figure 4.4 however, the energy collection is generally lower in that case.

Further simulations were conducted with the Fast sensor in the dosemeter geometry with incident neutron energies $E_n = 5\,\text{MeV}$ and $E_n = 14.8\,\text{MeV}$. For 5 MeV, a similar shape of the pulse height spectrum as with the AmBe source is expected, whereas for 14.8 MeV the shape should resemble the one for 100 MeV, since in that case Carbon ions play a greater role. The two energies were chosen in order to compare the outcomes with former measurements at the Physikalisch-Technische Bundesanstalt (PTB) done in 1999, where a pulse height spectrum was acquired with a previous version of the Fast sensor ([21, 23]). The measurement and simulation results are shown in figure 4.7. Indeed, the energy collection spectrum for $E_n = 5\,\text{MeV}$ shows the same characteristics as the one depicted in figure 4.3; also, the partial charge collection peak can be seen, since that effect plays a important role here as well

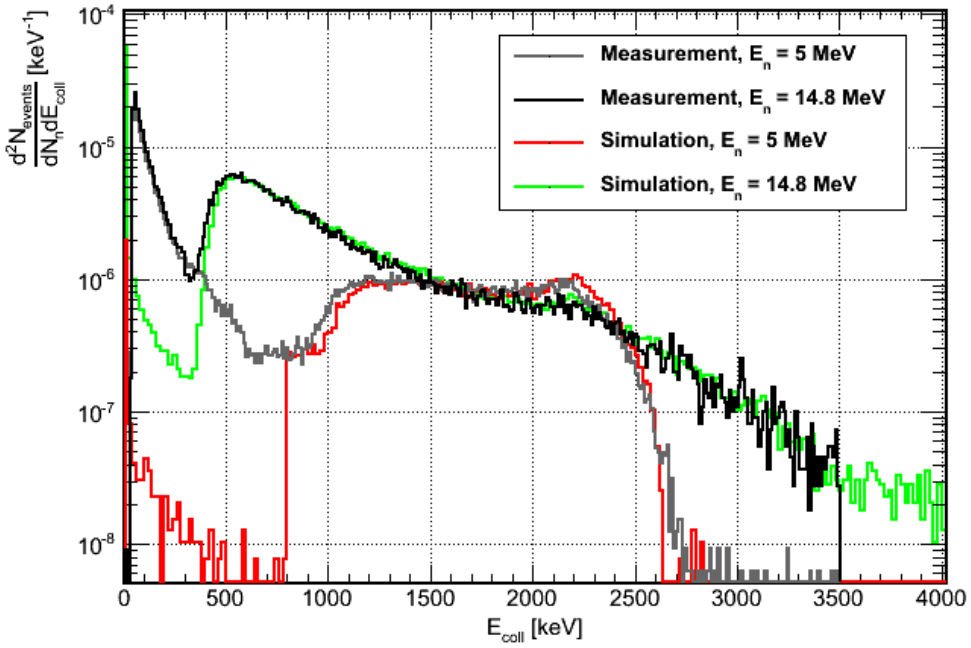

Figure 4.7.: Simulated and measured pulse height spectra of the Fast sensor in the dosemeter geometry with neutron energies $E_n = 5\,\mathrm{MeV}$ and $E_n = 14.8\,\mathrm{MeV}$. The missing signals in the 5 MeV simulation below $E_{coll} \approx 800\,\mathrm{keV}$ are due to the applied cut-off.

of course. The histogram for 14.8 MeV shows a shape roughly similar to the ones given in figure 4.6 on the previous page. Also in that case a small peak at around $E_{coll} \approx 2.2\,\mathrm{MeV}$ is observed. This is because here the energy of the incident neutrons is low enough to enable scattering on Hydrogen; the overall shape however indicates that the main contribution comes from Carbon ions and direct reactions of neutrons in the Silicon detector. The latter effect plays a great role for the *Delta* sensors as well, as will be shown below.

Finally, it can be noted that the measured and simulated energy collection spectra in figure 4.7 fit very well. The only significant differences are observed at $E_{coll} \lessapprox 800\,\mathrm{keV}$, which is partly due to the cut-off applied here as well and partly due to influences of photons etc. on the measured spectra. For the number of counts acquired with the threshold setting $E_{thresh} = 1\,\mathrm{MeV}$, as given in table 3.1, these differences are unimportant.

In the frame of the *Delta* study described in the next section, the dosemeter geometry was simulated on a phantom. In this geometry, also the Fast sensor was present. The resulting pulse height spectra of an irradiation of the dosemeter area on the phantom with $91.204{\cdot}10^6$ neutrons are given in figure 4.8. The neutron energies were $E_n = 5\,\mathrm{MeV}$ and $E_n = 14.8\,\mathrm{MeV}$, just like in the figure 4.7 above. Comparing the corresponding pulse height spectra, one can infer that the presence of a phantom does change neither the shape nor the number of signals in the relevant region $E_{coll} \geq E_{thresh} = 1000\,\mathrm{keV}$; thus, the number of *counts* would be unaffected.

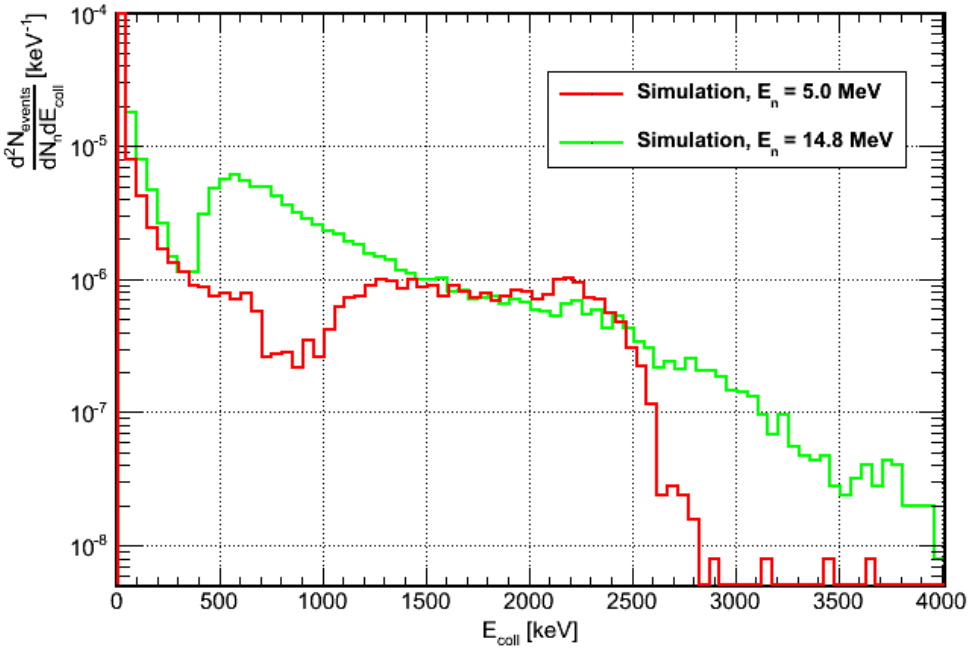

Figure 4.8.: Simulated pulse height spectra of the Fast sensor in a dosemeter geometry attached to a phantom; only the area of the dosemeter was irradiated with $91.204 \cdot 10^6$ neutrons of two different energies

This is clear from the fact that the protons and Carbon ions producing signals in that range are emitted in the direction of the incoming neutrons, which are incident from the front. The reactions in the Silicon detector material contributing to the 14.8 MeV spectrum cannot be triggered by backscattered neutrons as well due to their low energy (see next section). Thus, as far as the Fast sensor is concerned, a phantom is negligible in both simulation and measurement.

4.1.2. Simulation of the Delta sensors

It has been shown in the previous section that for the *Fast* sensor the influence of surrounding material is little. In the case of the *Delta* sensors, this was not *a priori* clear since with that sensor, the process of signal creation is quite different. Moreover, a direct and quantitative comparison with measured pulse height spectra as with the Fast sensor is not possible here, because former works like [21, 20, 25, 23] refer to a very different design of the Delta sensors; with a higher influence of the surroundings and dimensions, these differences are crucial. Thus, it was decided to conduct a comprehensive study of the influences of various geometric components on the pulse height spectrum of the Delta sensors, creating further insight into its functionality.

For that purpose, four neutron energies were chosen, which were $E_n = 570\,\text{keV}$, $E_n = 1.2\,\text{MeV}$, $E_n = 5\,\text{MeV}$ and $E_n = 14.8\,\text{MeV}$. The overall design of the simulation application

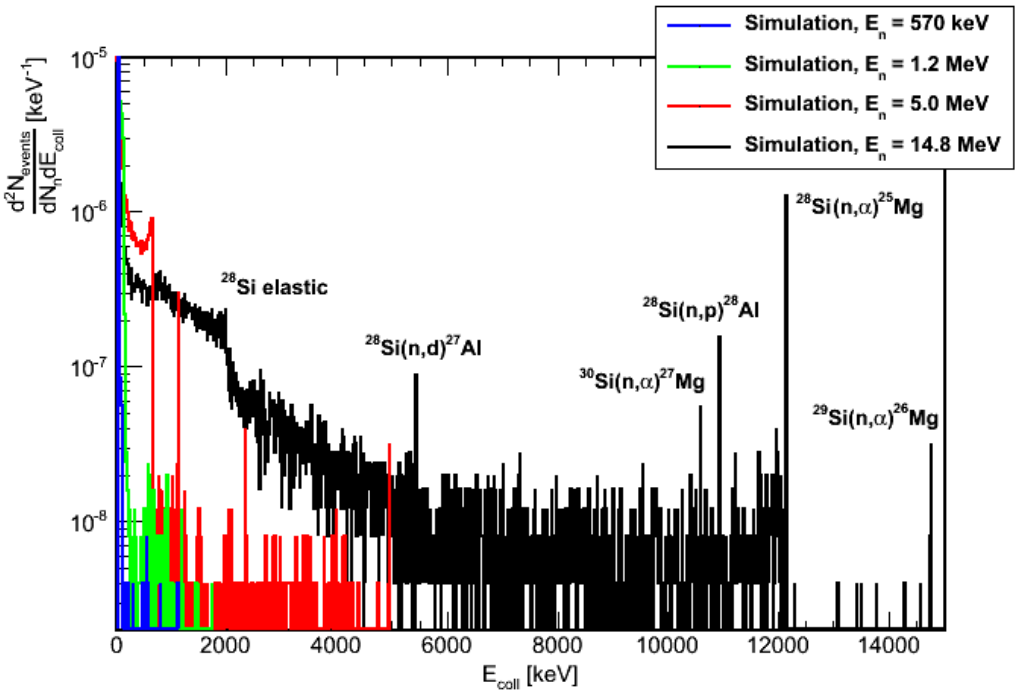

Figure 4.9.: Simulated pulse height spectra of the Silicon sensor alone, irradiated with $25 \cdot 10^6$ neutrons of four different energies. For the spectrum with $E_n = 14.8\,\mathrm{MeV}$, the reactions leading to some of the spectrum's characteristics are indicated.

was as described in supplement A.2. For the analysis, the CCE given in figure 3.5 on page 32 was used, as it was shown in the previous section that this model reproduces the features of the pulse height spectra of the Fast sensor quite well. Since the detector of the Delta sensors is of the same type, the same charge collection dependency on depth can be assumed here.

For the geometry, four steps were taken, in which the various components were added gradually. First, only the Silicon sensor was irradiated in the simulations. Then, the *LiF* converter with glue, as described in section 3.3.2, was added. After that, the sensor was placed in a housing and the dosemeter geometry, i.e. a steel case filled with Boron-Carbide. From that step on, differences between the *Delta D* and *Delta G* (which will be replaced by a γ-sensor eventually, [59]) were expected due to the different positions in the dosemeter head. As a last step, the dosemeter was simulated on a phantom. Here, however, only a rough estimate of the phantom influence was done, as not the whole phantom surface was irradiated in order to save CPU time.

Silicon detector only

The silicon detector alone was irradiated with $25 \cdot 10^6$ neutrons for each of the energies given above. The resulting pulse height spectra are given in figure 4.9. Here, different processes resulting in the signals can be identified. For the higher energies $E_n = 5\,\mathrm{MeV}$ and $E_n = 14.8\,\mathrm{MeV}$, an edge can be observed in the histograms at $E_{coll} \approx 1\,\mathrm{MeV}$ and $E_{coll} \approx 2\,\mathrm{MeV}$

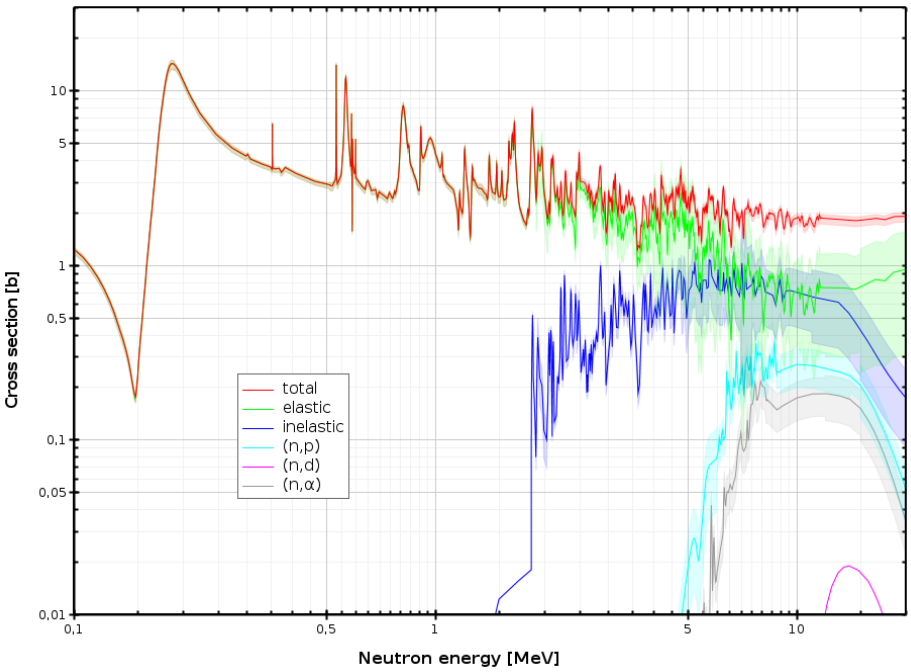

Figure 4.10.: Cross sections for various nuclear reactions of neutrons with natural Silicon, as well as for scattering and total cross section ([44])

respectively. Those stem from *elastic scattering* on ^{28}Si ([74]), which is the main Silicon isotope. The other lines standing out of the spectra for those energies come from *nuclear reactions* of the neutrons with Silicon, i.e. (n, α), (n, d) and (n, p) reactions. They can be identified according to their tabulated Q-value (see section 2.2), which is negative for the processes given here. Q-values can for example be found in [44]. The sum of kinetic energies of the particles produced is $E_n - |Q|$; if both reaction products deposit their energy in the active zone of the detector with a high CCE, $E_{coll} = E_n - |Q|$; since both are charged particles, their range in Silicon is rather short, resulting in a high probability that the energy deposition happens a very small volume, which yields the lines that can be seen in figure 4.9.

The cross sections for the various reactions of neutrons with Silicon are shown in figure 4.10. One can see that for the lower energies $E_n = 570\,\text{keV}$ and $E_n = 1.2\,\text{MeV}$, the (n, p), (n, d) and (n, α) reactions are not possible (due to the Q-value). Thus, no specific lines can be observed in the spectra shown in figure 4.9.

Since the Silicon detector used in the simulation here is the same for all of the sensors in the HMGU dosemeter, the study of the response of the Silicon itself to neutron radiation is of great importance. A pulse height spectrum as shown in the above figure underlies the spectra of the other sensors, i.e. the Fast and the Albedo sensor, as well, if the neutron energy is high enough. It must be concluded that for high energies $E_n \gg 5\,\text{MeV}$, most of the contribution to the signals stems from $Si + n$ reactions, also because for increasing neutron energies the cross sections for interactions with the various converter materials, i.e. ^6Li, C and H, decrease. E.g. for the simulation of the *Fast* sensor with $E_n = 100\,\text{MeV}$, as presented in the previous

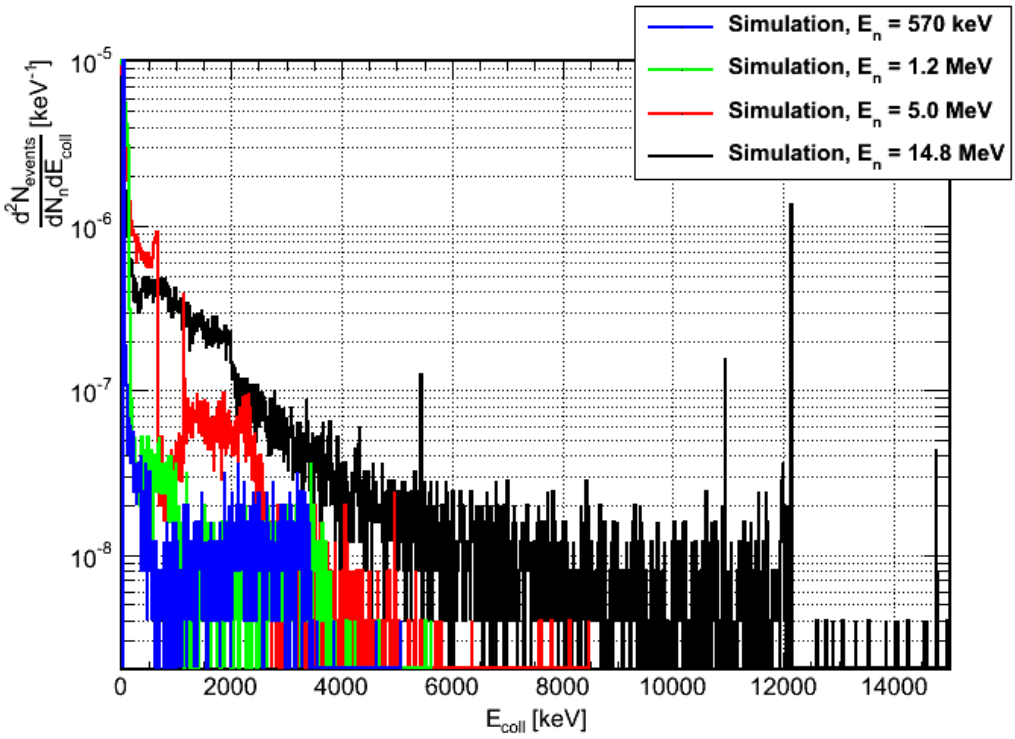

Figure 4.11.: Simulated pulse height spectra of the Silicon sensor with LiF converter, irradiated with $25 \cdot 10^6$ neutrons of four different energies.

section, most of the shape of the pulse height spectrum must actually be accredited to those direct reactions in Silicon.

Detector with ^6LiF converter

The next step in the study of the Delta sensors was the addition of a *converter* composed of Lithium-Fluoride (mainly of ^6LiF) and glue, as described in section 3.3.2, to the Silicon detector. The geometry was irradiated with $25 \cdot 10^6$ neutrons for each of the given energies. The outcome of the simulation is shown in figure 4.11.

For the highest energy $E_n = 14.8\,\text{MeV}$, the pulse height spectrum does not change much from the previous simulation, indicating that here the reactions in Silicon still play the dominant role. Also for $E_n = 5\,\text{MeV}$, still some of the characteristic lines from the $Si + n$ reactions are observed.

The influence of the LiF can be seen in the pulse height spectra for $E_n = 570\,\text{keV}$, $E_n = 1.2\,\text{MeV}$ and $E_n = 5\,\text{MeV}$. From figure 3.10 on page 37 and equation (3.8) one can infer that the tritium energy for the lower incident neutron energies is around $E_t \approx 3.5\,\text{MeV}$ and $E_t \gtrsim 4\,\text{MeV}$, respectively, if the particles are emitted in forward direction. At these energies, the signals with the highest collected energies occur in the spectra depicted in figure 4.11. Generally, more events are registered with a converter than for the detector alone, as it is expected. For $E_n = 5\,\text{MeV}$, the enhancement of the pulse height spectrum due to the converter

is clearly visible as well. According tho the figure on page 36 however, the cross section for the ${}^6Li\,(n,\alpha)\,{}^3H$ reaction is very low for that neutron energy already. But, as described in section 3.3.2, the converter of the Delta sensors consists of the elements Hydrogen and Carbon (in form of the glue) as well; the shape of the depicted pulse height spectrum is thus considered to stem from scattering on these nuclei, as well as on Lithium and Fluoride, plus a significant contribution from direct neutron reactions in Silicon as shown in figure 4.9.

The *tritium edge*, which is expected when comparing the measured pulse height spectrum in figure 3.11 on page 38 with the simulated ones shown here does not occur. This is due to the fact that in order to create such an edge, *thermal* or very low energetic neutrons are needed, since the cross section for the Lithium reaction (3.7) is high for low E_n only (figure 3.9). Those neutrons are usually produced by scattering in a *phantom*, as described in the next but one paragraph.

Sensor in dosemeter geometry

One more geometric design investigated in this study was the Delta sensors included in a dosemeter geometry, as it was done with the Fast sensor as well. Such a design is shown in figure 4.1b on page 44 for example. Here both positions of the Delta sensor, i.e. in front of the Albedo one and at the back side of the dosemeter head, corresponding to the sensors *Delta D* and *Delta G* (see figure on page 33), were simulated. The dosemeters were irradiated with $8.33 \cdot 10^6$ neutrons for each of the energies denoted above; the results are given in figures 4.12a and 4.12b.

By comparing these two figures, it can be concluded that the position of the sensor in the dosemeter head dose not make a great difference, as corresponding pulse height spectra look quite the same; also, the number of events per energy bin itself is comparable. This is because for the energies given here, the mechanisms leading to signal creation do not alter when adding more material; i.e., for lower E_n the reactions in the converter play a main role, whereas for high E_n the direct $Si + n$ reactions are dominant.

Between the spectra on the facing page, which were acquired with detector and converter only, and the energy collection spectra given here, the main difference is that the characteristic features, i.e. the lines corresponding to certain nuclear reactions at $E_n = 5\,\mathrm{MeV}$ and $E_n = 14.8\,\mathrm{MeV}$, seem to have disappeared. Also, the edge stemming from elastic scattering on ${}^{28}Si$ is no longer clearly visible for the highest neutron energy. This is partly due to *binning* (The energy bins in figures 4.12 are broader than above, allowing for less simulated events.), and partly due to the fact that the amount of material added here, i.e. the Cadmium housing and the dosemeter filling consisting of Boron, Carbon, Hydrogen and Oxygen, leads to a *"blurring"* of the incident neutron energies by elastic and inelastic scattering. For $E_n = 5\,\mathrm{MeV}$, the ${}^{28}Si$ edge is still visible however, since both effects, unlike for $E_n = 14.8\,\mathrm{MeV}$, cannot compensate the steep decline in the pulse height spectrum following the edge.

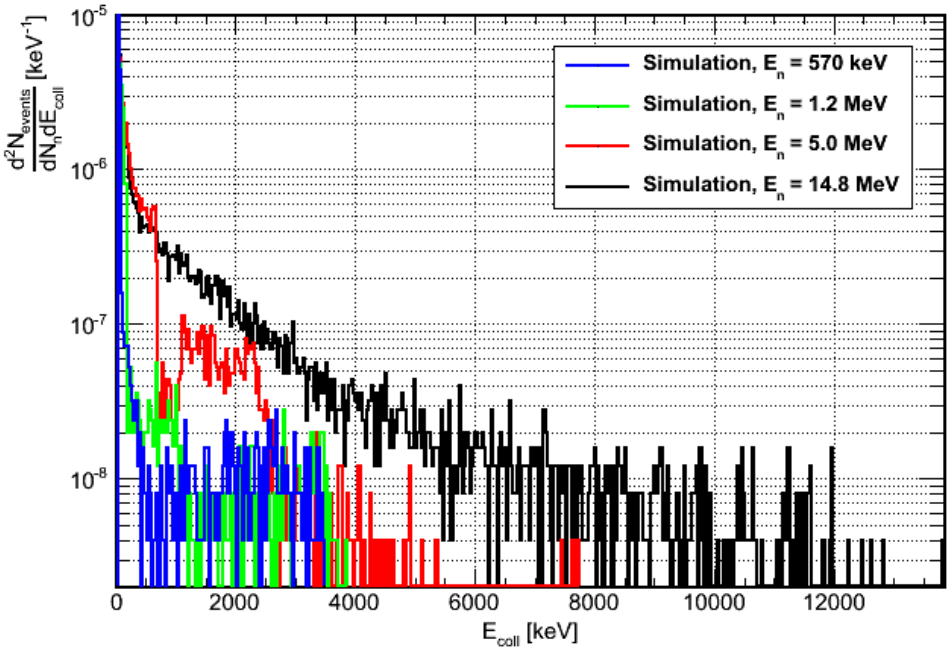

(a) Delta D

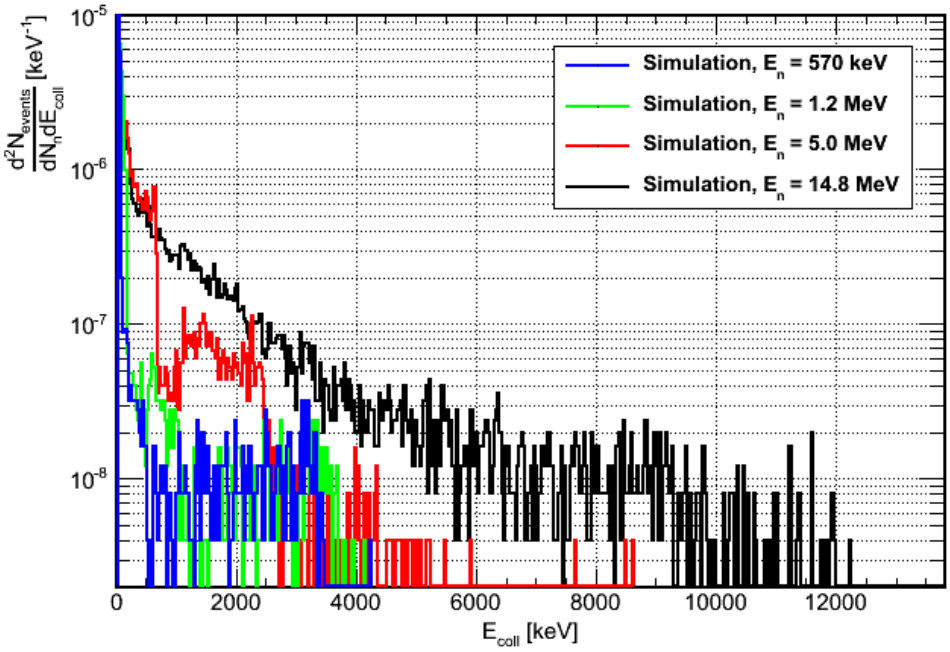

(b) Delta G

Figure 4.12.: Simulated pulse height spectra of the Delta D and Delta G sensors in a dosemeter geometry, irradiated with $8.33 \cdot 10^6$ neutrons at four different energies each

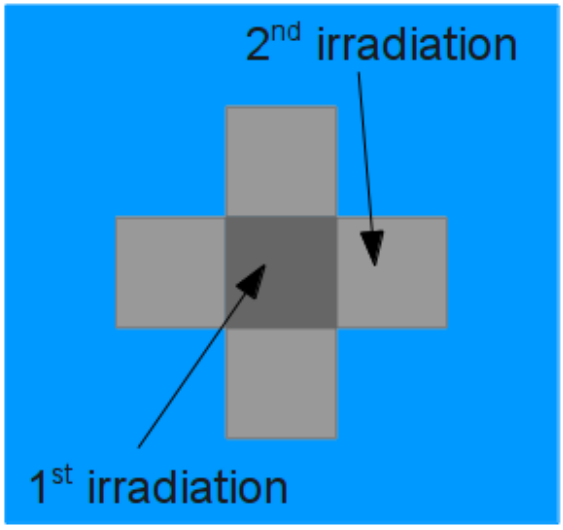

Figure 4.13.: Irradiation pattern in the investigation of the phantom influence on the pulse height spectra of the Delta sensors. First, the dosemeter area was irradiated, then the same area next to the dosemeter.

Dosemeter on phantom

The last step in this study was to investigate the influence of a slab *phantom* on the pulse height spectrum of the Delta sensors. Since the reaction of neutrons with ^6Li has a very high cross section for low neutron energies only (figure 3.9 on page 36), backscattered neutrons from a phantom with thermal and epithermal energies are expected to greatly enhance the number of signals in the spectra, although with low energies more neutrons are absorbed by the surrounding dosemeter materials like Boron, Cadmium etc.

The simulation of a phantom however constitutes a computationally extensive task. Since no information on the neutron tracks within the phantom are known in advance, i.e. no *importance* can be given to apply variance reduction techniques ([75]), the phantom surface of $30 \times 30\,\mathrm{cm}^2$ must be irradiated with a uniform fluence. The neutrons incident on parts of the surface that are not covered by the dosemeter have only a small chance of being scattered into the sensors; their track however must be simulated up to the end. This simulation of neutron interactions in the phantom body is time-consuming as well, since with raising number of scattering events, the cross sections tend to increase, which leads to shorter distributions of path lengths according to equation (2.3) and thus more computational activity. This problem would be even more obstructive if the $S(\alpha, \beta)$ matrix mechanism was applied as described in [76].

Therefore, for the study of the Delta sensors, it was chosen to produce only a rough estimation of the influence of a phantom. In the next section 4.1.3, a thorough simulation of the dosemeter attached to a phantom is presented. Here, the geometry depicted in figure 4.1c was implemented, but the beam width was not extended to cover the surface of the whole phantom. Instead, the dosemeter area was irradiated with $91.204 \cdot 10^6$ neutrons first with the

usual energies $E_n = 570\,\mathrm{keV}$, $E_n = 1.2\,\mathrm{MeV}$, $E_n = 5\,\mathrm{MeV}$ and $E_n = 14.8\,\mathrm{MeV}$; after that, the same area but *next to* the dosemeter was irradiated, with the same number of neutrons per energy, as shown in figure 4.13. The pulse height spectra for those to simulations were acquired independently. To estimate the influence of the neutrons scattered in the phantom, the pulse height spectra of the second irradiations were added four times to the ones of the first simulation, yielding an effective irradiated area as given in the figure. Here, it is assumed that neutrons e.g. from the left and the right side have the same chance of being scattered towards the sensor; at least for the *Delta G*, which is near the center of the dosemeter (figures 3.6 and 4.1b), this assumption is valid.

The results of the given procedure are shown in figure 4.14. Here, the influence of the scattered neutrons on the pulse height spectra is clearly visible, specially for $E_n = 570\,\mathrm{keV}$ and $E_n = 1.2\,\mathrm{MeV}$. When comparing these spectra to the ones shown in figure 4.12, one can see that the low energy neutrons now lead to an edge at the energy predicted by equation (3.9), i.e. $E_{coll} \approx 2.7\,\mathrm{MeV}$. The same edge occurs for $E_n = 5\,\mathrm{MeV}$, which means that even at this neutron energy scattered particles can contribute to the signals. The difference to figure 4.12 is not so huge however, since there many events with $E_{coll} \lessapprox 2 \ldots 3\,\mathrm{MeV}$ where counted, stemming from elastic scattering events in the converter. Thus, the additional contribution by the phantom is relatively low.

The histogram for $E_n = 14.8\,\mathrm{MeV}$ is seemingly unaffected by the phantom. Here the $Si+n$ reactions still play a dominant role so that additional signals from scattered neutrons do not affect the overall shape of the pulse height distribution. Moreover, with higher neutron energies the particles entering the phantom need to be scattered more often in order to be slowed down to energies where the cross section for reaction (3.7) is high, which is generally less probable than the fewer interactions needed for lower incident neutron energies.

When comparing figures 4.14a and 4.14b, one can see that for the higher neutron energies, the pulse height spectra are only very little influenced by the position of the sensor. For the lower energies, the more signals are acquired in the Delta D sensor, since that one is situated nearer to the phantom surface, so that scattered neutrons have to travel through less material to reach the converter.

Although these simulations with a phantom can be regarded a rough estimate only, they show very well the influence of the backscattered neutrons on the pulse height spectra at low energies. For quantitative statements, the whole phantom surface must be irradiated, which is shown in the next section. Here, the main result that can be inferred from figure 4.14 is that even though the phantom influence greatly enhances the number of signals with $E_{coll} \lesssim 2.73\,\mathrm{MeV}$, the signal number *above* that energy is not affected. This becomes clear when considering that for a tritium energy E_t higher than the given value, the particle must be emitted in the direction of the incident neutron (equation (3.8)). Thus, if the neutron is a scattered one coming from the back side, i.e. the phantom, the highest energy that can be achieved is given by equation (3.9) as $2.73\,\mathrm{MeV}$. In the figures on page 56 and 59, these signals with E_{coll} higher than that value either come from neutrons hitting the converter directly, or

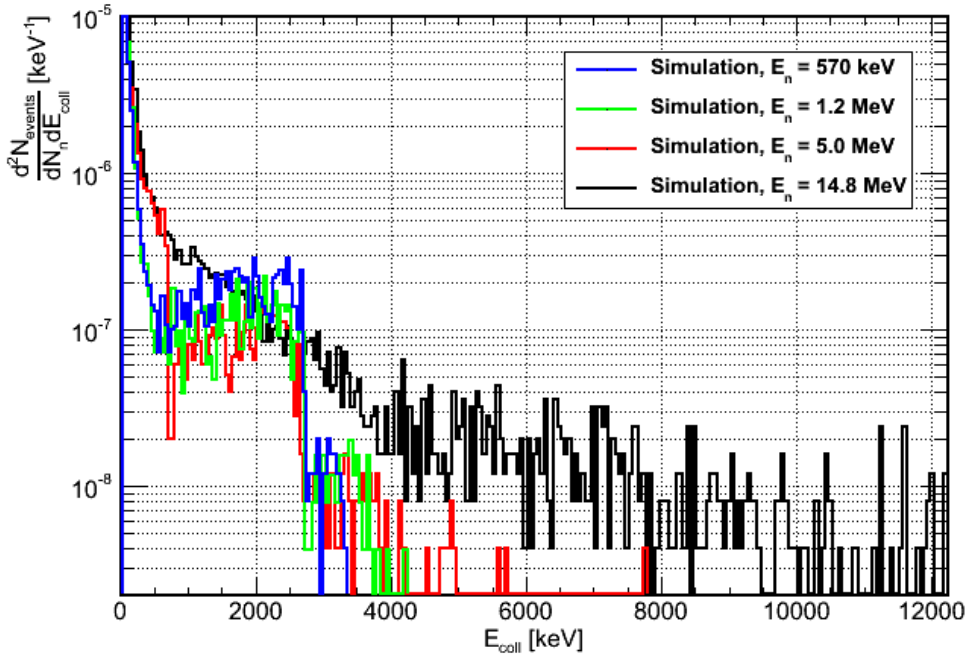

(a) Delta D

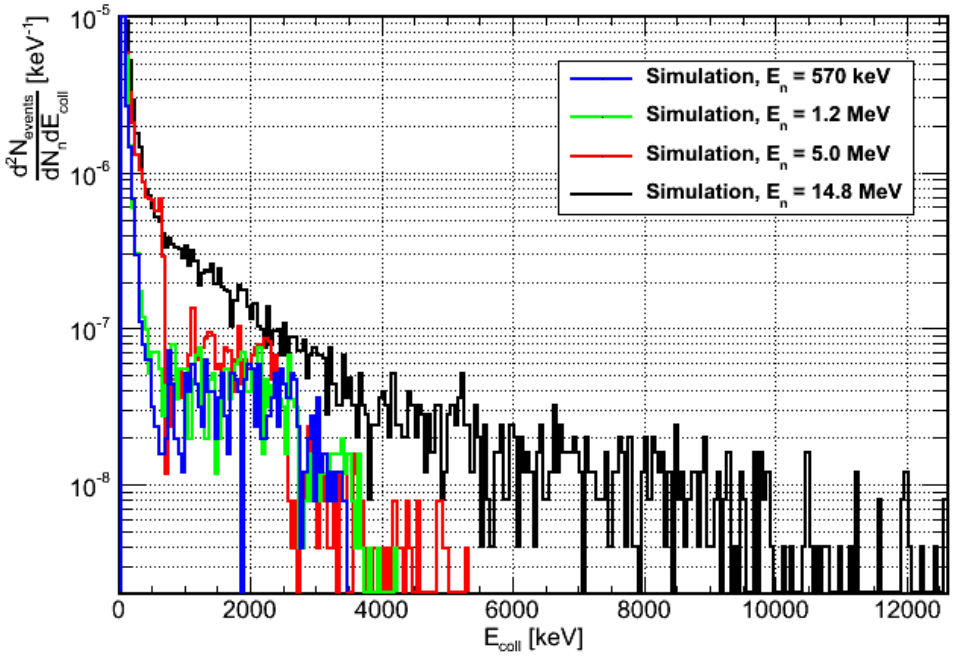

(b) Delta G

Figure 4.14.: Simulated pulse height spectra of the Delta D and Delta G sensors in a geometry involving a phantom. The irradiation patter was as given in figure 4.13, with summed up pulse height spectra shown here.

even from neutrons interacting in the Silicon detector. The latter events are not influenced by a phantom as well, since the nuclear reaction given in figure 4.9 all posses $Q < 0$, meaning that the neutron energy has to be higher than a certain value for interaction.

For the functionality of the Delta sensors, only the number of *counts* is essential, that is the number of signals with $E_{coll} > E_{thresh}$. As described thoroughly in section 3.3.2, this threshold value E_{thresh} is chosen according to the Lithium edge to be $E_{thresh} = 2.8\,\mathrm{MeV}$ (see table on page 28 and [25]). Since the phantom does not influence the number of *signals* beyond that value, it does not influence the number of *counts*; just as for the Fast, it is thus disposable for the functioning of the Delta sensors.

4.1.3. Simulation of the Albedo sensor

The third type of sensor installed in the HMGU dosemeter is the *Albedo* sensor. According to section 3.3.3, its design is almost equal to the Deltas, only with a 5 mm hole in the back side of the Cadmium housing enabling more low-energy neutrons to enter the sensor. As the name "Albedo" already suggests, it is considered especially sensible to neutrons scattered back from a phantom. Thus, for the simulation of this sensor, the full phantom geometry had to be implemented and irradiated (see figure 4.1c on page 44). For a result, a pulse height spectrum similar to the Delta spectra shown on the previous page is expected, since the mechanism of signal creation is quite the same.

In order to conduct the simulations, the parallelized version of the GEANT4 applications described in supplement A.2 was utilized; calculations were performed on 24 CPU cores at the TU MÜNCHEN.

For a thorough simulation, the AmBe spectrum shown in figure 4.2 on page 45 was used as a input, with a total number of neutrons incident on the phantom surface of $2.25 \cdot 10^9$, corresponding to a fluence $\Phi_n = 2.5 \cdot 10^6\,\mathrm{cm}^{-2}$. In order to slightly speed up the simulations, different *range cuts* (see section A.1) were applied, namely $0.002\,\mu$m in the sensor regions, $2.0\,\mu$m in the rest of the dosemeter and $6.0\,\mu$m in the phantom. The materials used in the simulation were constructed from isotopes mainly.

Since in order to create a correct pulse height spectrum for the Albedo sensor the whole dosemeter geometry had to be implemented, also the other sensors Fast, Delta D and Delta G were present in the simulations. As the phantom has no influence on the Fast sensor as shown above, and also its impact on the Delta spectra had been estimated, those sensors´ results were analyzed as well, serving as a validation. The acquired pulse height spectra of a all four sensors are shown in figure 4.15. Concerning the outcome of the *Fast* sensor, one can see that the spectrum is not different from the one given in figure 4.3; the partial charge collection peak is clearly visible (since of course the CCE model from the above section was applied) and the overall signal number is around $0.6 \cdot 10^{-6}$ per keV and incident neutron. For the Delta sensors, a small contribution from the scattered neutrons can be inferred. Below the Lithium edge $E_{coll} \approx 2.7\,\mathrm{MeV}$, more signals are registered in the Delta D sensor, since this one is nearer to the phantom surface. The dominant part of the signals in both Delta

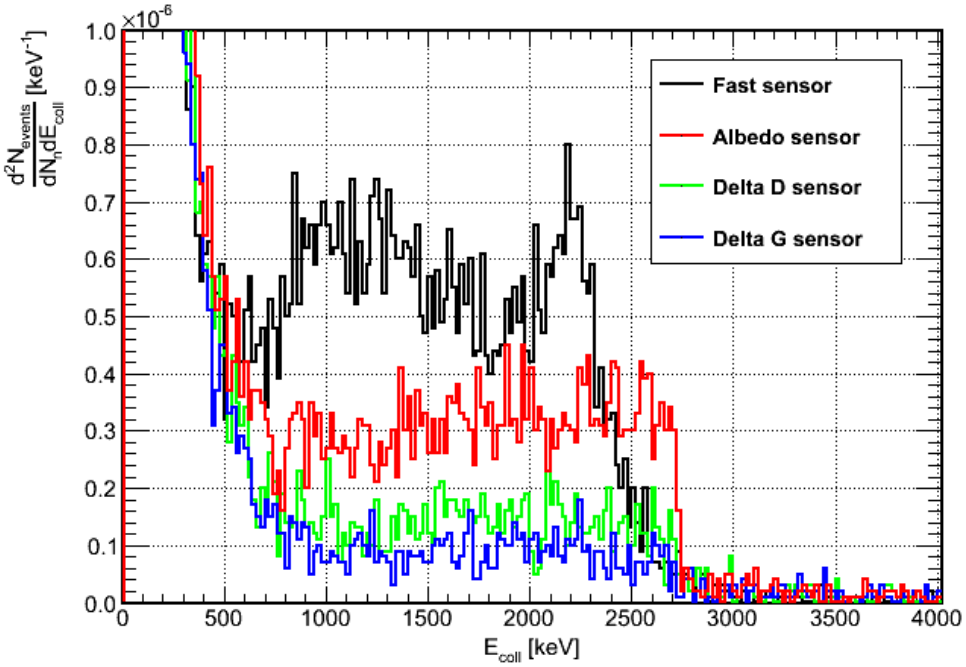

Figure 4.15.: Simulated pulse height spectra of all four sensors, including the Albedo, in a dosemeter geometry attached to a phantom irradiated with $2.25 \cdot 10^9$ neutron from the AmBe energy spectrum shown in figure 4.2

sensors however come from direct reactions in the converters and detectors. That result is in agreement with the outcome of the Delta study presented above.

For the Albedo sensor itself, the contribution of the low energetic scattered neutrons is much higher than for the Deltas. This can be seen from the pulse height spectrum given in the figure, considering that for $E_{coll} \lessapprox 2.7\,\mathrm{MeV}$, the number of signals exceeding the result of the Delta D (which is, apart from the hole, equal to the Albedo) stems from those events. Of course, at the relatively high energy of the AmBe neutrons (figure 4.2), also scattering reactions in the converter and direct $Si + n$ reactions play a role for the Albedo. This can be seen from the signals $E_{coll} > 2.7\,\mathrm{MeV}$ displayed in 4.15. Those signals cannot be created by neutrons coming from the back side of the detector, since according to equation 3.8 the maximal achievable energy is $E_t \approx 2.7\,\mathrm{MeV}$ in that case. Thus, concerning those events, the Albedo sensor behaves like the Delta ones presented in section 4.1.2. The neutrons triggering the ${}^6Li\,(n,\alpha)\,{}^3H$ reaction in the converter of the Albedo however are considered to come from the phantom through the hole in the Cadmium housing mainly.

The simulation program used to create the pulse height spectra 4.15 had been augmented before the run with the AmBe source energy spectrum, so that the primary positions of the neutrons creating a specific energy deposition in the various detectors could be scored. For that, no additional actual *scorer* had to be implemented; the information on the primary position was simply handed to the *Monitor* class by the *PrimaryGenerator* and then dumped

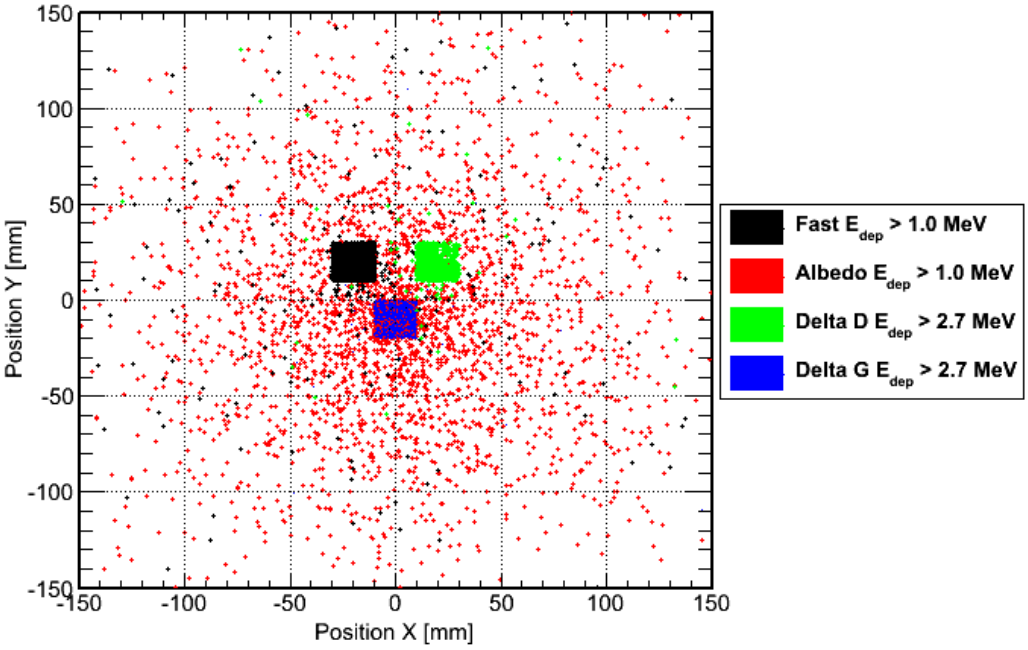

Figure 4.16.: Primary neutron positions of the events leading to energy deposition in the fours detectors with E_{dep} higher than certain values

to a dedicated table in the MySQL database (see figure A.1 on page 139). The analysis of that table gives further information on the influence of the phantom on the sensors, since the position of the neutron at the beginning of an event is also the position on the phantom surface where the latter is entered, or the position on the sensor area where a direct reaction occurs. By visualizing the distribution of positions of primary neutrons corresponding to a certain energy deposition, one can estimate how far the neutron track length in the phantom is or if scattered neutrons play a role for the pulse height spectrum at all.

The result of that analysis is displayed in figure 4.16. Here, distributions for all four sensors are drawn. For the Fast and Albedo sensors, events leading to a energy deposition $E_{dep} > 1.0\,\mathrm{MeV}$ were chosen, since those events are likely to create a count considering the threshold value $E_{coll} > E_{thresh} = 1000\,\mathrm{keV}$ (see table on page 28). For the Delta sensors, events with $E_{dep} > 2.7\,\mathrm{MeV}$ are shown for the same reason. One can see that for these sensors and the Fast, the positions of events yielding such a high energy deposition are concentrated on the sensor areas. In those cases, the primary neutrons hit the sensors *directly*, triggering either a $Si+n$ reaction in the detectors or creating secondary particles in the converters with energies high enough for the given energy deposition. Although scattered contribution is unimportant for the Fast and Deltas, neutrons that are scattered in the phantom and still deposit a huge amount of energy in the detectors of these sensors are also observed. Those neutrons obviously leave the phantom with energies high enough to undergo nuclear reactions in Silicon.

With the Albedo sensor, the situation is different. Although here a concentration of event

positions in the sensor area (the same as the one of the Delta G, see page 33) can be observed, most events with high energy deposition are scattered in the phantom. In figure 4.16, only around 36 % of the drawn positions are within the Albedo area; inside a $5 \times 5\,\mathrm{cm}^2$ square area, 64 % and within $10 \times 10\,\mathrm{cm}^2$, 90 % of the positions can be found. This is a clear indication that for the Albedo, a phantom is essential, even at high neutron energies like with the AmBe source. This result was also found experimentally, as described in section 5.2.

The intended energy range for the Albedo sensor is however not the high energetic one, but the lower energies, down to thermal neutrons. When measuring with a AmBe source, the contribution of the Albedo to the reading of the HMGU dosemeter is little ([25]). Thus, more simulations of the Albedo sensor with a phantom were conducted, with neutron energies below $E_n = 10\,\mathrm{keV}$. As described in supplement A.1, at low energies the *ThermalScattering* module in the physics lists of GEANT4 should be enabled, which implements the $S(\alpha, \beta)$ matrix describing the interaction of thermal neutrons with certain molecules like polyethylene or water [76, 77, 5]. This functionality was activated here; in order to retain a reasonable runtime of the application, the number of events was reduced to $180 \cdot 10^6$, yielding a fluence of $\Phi_n = 200 \cdot 10^3\,\mathrm{cm}^{-2}$.[2] The neutron energies used were $E_n = 25\,\mathrm{meV}$ (see footnote 1 on page 18), $E_n = 1\,\mathrm{eV}$, $E_n = 10\,\mathrm{keV}$ and $E_n = 10\,\mathrm{MeV}$, with the latter serving as a comparison since the thermal scattering physics is considered to lead to no difference at that high energy.

For further comparison, some of the simulations results described in the next section 4.2 were analyzed in terms of pulse height spectra. For those simulations, no thermal scattering was enabled, i.e. only the *High Precision Neutron Model* (see supplements A.1 and A.2). The fluence there was $\Phi_n = 500 \cdot 10^3\,\mathrm{cm}^2$ for each of the above neutron energies. For the energies $E_n = 25\,\mathrm{meV}$, $E_n = 1\,\mathrm{eV}$ and $E_n = 100\,\mathrm{eV}$, position distribution plots like figure 4.16 were created.

In figure 4.17 on the following page, the pulse height spectra for the four energies given above, acquired both with and without thermal scattering, are shown. Here, the filled spectra correspond to the activated $S(\alpha, \beta)$ matrix. The general difference in shape between low and high neutron energy (that is, $E_n = 10\,\mathrm{MeV}$) can be seen for both methods; i.e. for high incident energy, the direct reactions play a main role creating a differently formed energy collection spectrum, just as with the Delta sensors in figure 4.14. For all histograms however, the total number signals per energy bin and incident neutron is lower if thermal scattering is enabled.[3] This is especially noticeable for $E_n = 10\,\mathrm{keV}$. The reason for this is that neutrons which originally posses that kinetic energy need to be scattered more often to achieve thermal energies; thus, the altered cross sections below 4 eV (see A.1 and [76, 77]) come to their own. This is not the case if the neutron energy is below that value originally already, because in that case a augmented scattering probability and kinematics would not alter such a great number of events. Therefore, the difference between the histograms for $E_n = 1\,\mathrm{eV}$ and $E_n = 25\,\mathrm{meV}$

[2] With that value, and a response of roughly $R = 2000\,\mathrm{cm}^2$, the relative statistical error in the number of counts according to equation A.10 is around 5 %.

[3] Note that this is not due to the different number of incident neutrons, since all pulse height spectra are scaled with that number according to section A.3

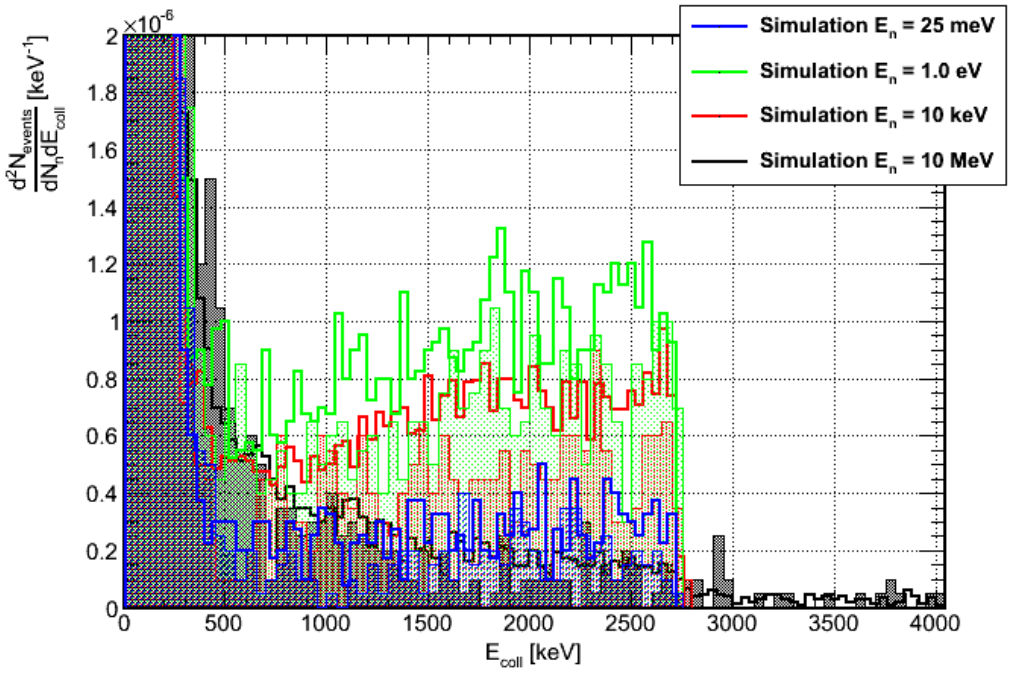

Figure 4.17.: Simulated pulse height spectra of the Albedo sensor in a dosemeter geometry attached to a phantom, for four neutron energies. The filled histograms were acquired with the $S(\alpha, \beta)$ matrix enabled and $180 \cdot 10^6$ incident neutrons per energy, the unfilled ones with the HP package only and $450 \cdot 10^6$ neutrons per energy.

is smaller in comparison. For 10 MeV, the difference in pulse height spectra is small due to the fact that here the scattered neutrons play a less dominant role, as explained above.

The positions of the primary neutrons leading to a energy deposition higher than the collection threshold value for the Albedo sensor, i.e. $E_{dep} > 1000\,\mathrm{keV}$, were scored in the thermal scattering simulation as well. In figure 4.18, these distributions are compared to corresponding distributions acquired without thermal scattering. In both cases, it can be seen that for the lowest energy $E_n = 25\,\mathrm{meV}$, only very few events can be counted, and that within the dosemeter area (except the area of the sensor itself), almost no positions are shown. The same is true for $E_n = 1\,\mathrm{eV}$; here, however, many events are displayed within the sensor area. The reason for this behavior is that for low energies, absorption in the Boron filling of the dosemeter is very important due to the high cross section ([44, 25]). For thermal neutrons, also the reactions in the Cadmium housing of the Albedo sensor plays a role (see figure 3.8). The situation is different for $E_n = 100\,\mathrm{eV}$ and $E_n = 10\,\mathrm{keV}$, where the $B + n$ cross section is lower already, and the neutrons can pass the dosemeter filling more unresisted. As expected, for $E_n = 10\,\mathrm{MeV}$, almost all energy depositions are due to events with the original position in the sensor area, as these correspond to direct reactions.[4]

[4] In figure 4.18b, the position marker are just concealed by the markers belonging to $E_n = 1\,\mathrm{eV}$.

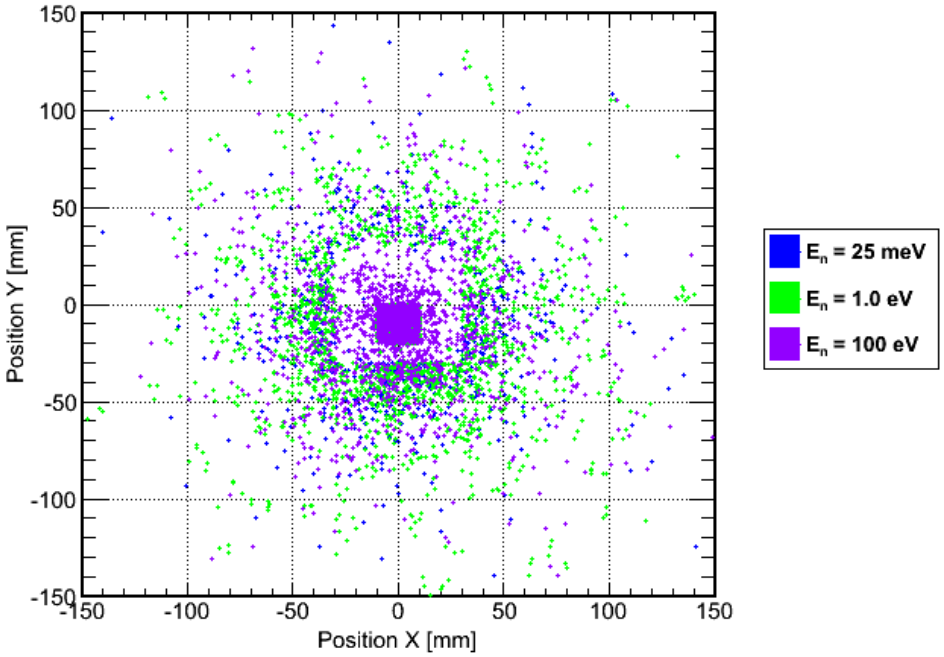

(a) Position distribution for $E_n = 25\,\mathrm{meV}$, $E_n = 1\,\mathrm{eV}$ and $E_n = 100\,\mathrm{eV}$, acquired *without* thermal scattering and $\Phi_n = 500 \cdot 10^3\,\mathrm{cm}^{-2}$

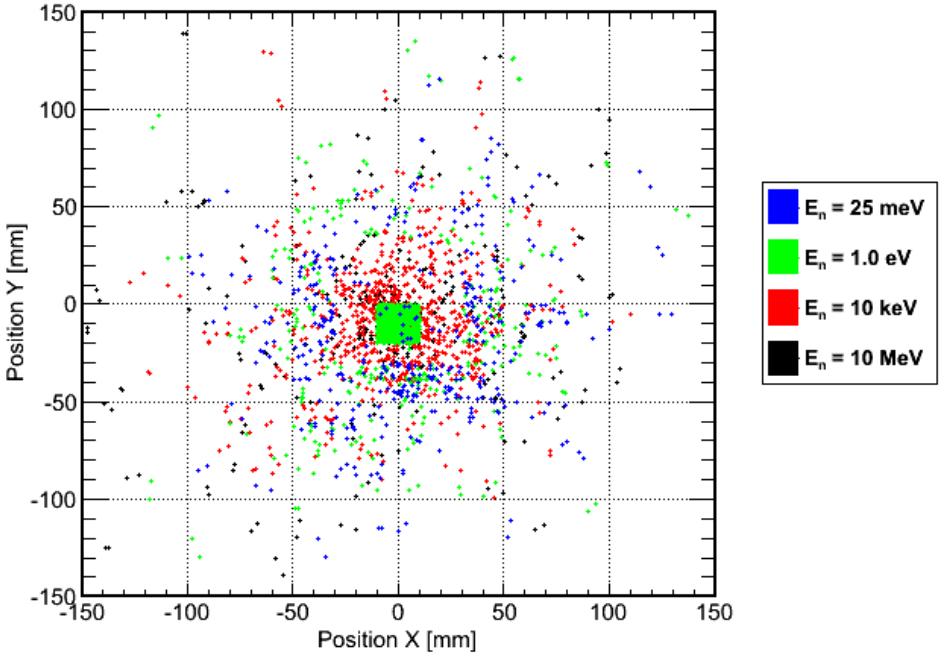

(b) Position distribution for $E_n = 25\,\mathrm{meV}$, $E_n = 1\,\mathrm{eV}$, $E_n = 10\,\mathrm{keV}$ and $E_n = 10\,\mathrm{MeV}$, acquired *with* thermal scattering enabled and $\Phi_n = 200 \cdot 10^3\,\mathrm{cm}^{-2}$ (scaled to the same fluence as in 4.18a)

Figure 4.18.: Primary neutron positions of the events leading to a energy deposition $E_{dep} > 1000\,\mathrm{keV}$ in the Albedo detector for three and four different primary neutron energies, respectively. In 4.18a, thermal scattering was not activated, whereas 4.18b was acquired with enabled $S(\alpha, \beta)$ matrix

The difference between thermal scattering being activated and not can be inferred best when comparing the distributions for $E_n = 1\,\mathrm{eV}$ in the figure. With the $S(\alpha, \beta)$ matrix, considerably fewer neutrons that enter the phantom outside the sensor and dosemeter area and still create a significant signal are observed. This is of course due to the altered cross sections, which obviously result in a slightly lower probability for these neutrons to enter the sensor. The outcome is a lowered pulse height spectrum as can be seen in figure 4.17. In how far this affects the number of *counts* and thus the response of the Albedo calculated from the simulations is described in the next section.

4.2. Calculation of response functions

In the previous sections, the focus of the described simulations and the discussion of the results had been on the pulse height spectra. From the shape of these spectra, a lot of information on the reaction mechanisms leading to detectable signals, and in the case of the Fast sensor even on the charge collection efficiency of the Silicon detectors (see page 44), can be inferred. As explained in supplement A.3, the analysis of the simulation results however involves a second step, which is the calculation of each individual sensor´s *response function* from the pulse height spectra, whose acquisition from the raw data in the MySQL table (figure on page 139) constituted the first step.

The creation of these spectra is outlined in listing A.3; using ROOT ([78]), also the integration of the spectra could be accomplished easily. According to equation (A.5), such an integration of the energy collection spectrum from the corresponding threshold E_{thresh} yields the response η, i.e. the number of *counts* per number of neutrons incident on the sensor, or, when multiplied with the sensor area A, the response R, which is the number of counts divided by the neutron *fluence*.

For the simulation of the *Albedo* sensor, which included the whole dosemeter geometry with a phantom as shown in figure 4.1c on page 44, the four sensors of the HMGU dosemeter had been implemented already. The aim of the following simulations was to create pulse height spectra for all sensors, not only at arbitrary neutron energies for individual analysis, but over a wide energy range. By using an automatic analysis procedure implemented in ROOT, the necessary steps, i.e. reading of the data, creation of pulse height spectra and their integration as well as the output of the inferred response, could be done for a given *SimID* range (see supplement A.2) all at once. For later re-analysis, e.g. with other threshold values than given in table 3.1, the pulse height spectra were stored in data files, which allowed of a skip of the time-consuming reading step in the analysis procedure after the first time.

Generally, the response of the dosemeter, or the sensors it is made up, was calculated for the two situations *with* phantom and *without*. From previous results, i.e. the comparison of pulse height spectra, it is clear that the addition of a phantom to the simulation geometry alters the result of the Albedo sensor only. However, since such a change in geometry made it necessary to create a different GEANT4 application anyway, two different runs were conducted.

Simulation without phantom			Simulation with phantom		
E_n [keV]	Φ_n [cm^{-2}]	Physics models	E_n [keV]	Φ_n [cm^{-2}]	Physics models
0.000025	$1 \cdot 10^6$	Binary, HP	0.000025	$500 \cdot 10^3$ and $200 \cdot 10^3$	Binary, HP, TS
0.001	$1 \cdot 10^6$	Binary, HP	0.001	$500 \cdot 10^3$ and $200 \cdot 10^3$	Binary, HP, TS
0.1	$1 \cdot 10^6$	Binary, HP	0.1	$500 \cdot 10^3$	Binary, HP
1	$1 \cdot 10^6$	Binary, HP	1	$500 \cdot 10^3$	Binary, HP
10	$1 \cdot 10^6$	Binary, HP	10	$1.875 \cdot 10^6$ and $200 \cdot 10^3$	Binary, HP, TS
50	$1 \cdot 10^6$	Binary, HP	50	$1.875 \cdot 10^6$	Binary, HP
100	$1 \cdot 10^6$	Binary, HP	100	$1.875 \cdot 10^6$	Binary, HP
200	$1 \cdot 10^6$	Binary, HP			
250	$1 \cdot 10^6$	Binary, HP	250	$1.875 \cdot 10^6$	Binary, HP
350	$1 \cdot 10^6$	Binary, HP	350	$1.875 \cdot 10^6$	Binary, HP
500	$1 \cdot 10^6$	Binary, HP	500	$1.875 \cdot 10^6$	Binary, HP
1000	$1 \cdot 10^6$	Binary, HP	1000	$1.875 \cdot 10^6$	Binary, HP
2000	$1 \cdot 10^6$	Binary, HP	2000	$1.875 \cdot 10^6$	Binary, HP
3000	$1 \cdot 10^6$	Binary, HP	3000	$1.875 \cdot 10^6$	Binary, HP
4000	$1 \cdot 10^6$	Binary, HP	4000	$1.875 \cdot 10^6$	Binary, HP
6000	$1 \cdot 10^6$	Binary, HP	6000	$1.875 \cdot 10^6$	Binary, HP
7500	$1 \cdot 10^6$	Binary, HP	7500	$1.875 \cdot 10^6$	Binary, HP
10000	$1 \cdot 10^6$	Binary, HP	10000	$1.875 \cdot 10^6$ and $200 \cdot 10^3$	Binary, HP, TS
12000	$1 \cdot 10^6$	Binary, HP	12000	$1.875 \cdot 10^6$	Binary, HP
16000	$1 \cdot 10^6$	Binary, HP	16000	$1.875 \cdot 10^6$	Binary, HP
21000	$1 \cdot 10^6$	Binary, Bertini, HP	21000	$1.875 \cdot 10^6$	Binary, HP
25000	$1 \cdot 10^6$	Binary, Bertini, HP	25000	$1.875 \cdot 10^6$	Binary, HP
40000	$1 \cdot 10^6$	Binary, Bertini, HP	40000	$1.875 \cdot 10^6$	Binary, HP
60000	$1 \cdot 10^6$	Binary, Bertini, HP	60000	$1.875 \cdot 10^6$	Binary, HP
75000	$1 \cdot 10^6$	Binary, Bertini, HP	75000	$1.875 \cdot 10^6$	Binary, HP
100000	$1 \cdot 10^6$	Binary, Bertini, HP	100000	$1.875 \cdot 10^6$	Binary, HP
200000	$1 \cdot 10^6$	Binary, Bertini, HP	200000	$1.875 \cdot 10^6$	Binary, HP
500000	$1 \cdot 10^6$	Binary, Bertini, HP			
1000000	$1 \cdot 10^6$	Binary, Bertini, HP			

Table 4.1.: Parameters used for the simulation runs to calculate the dosemeter response functions

For the simulations without the phantom, four (virtual) CPU cores on a local computer were used. The energy range applied there was $E_n = 25\,\mathrm{meV} \ldots 1\,\mathrm{GeV}$, based on the evaluation at 29 distinct energies. The fluence was $\Phi_n = 1 \cdot 10^6\,\mathrm{cm}^{-2}$, corresponding to a number of incident neutrons of around $36.5 \cdot 10^6$, per energy. For the physics, of course the *High Precision* neutron model (HP) was used at the energies of $E_n < 20\,\mathrm{MeV}$. At higher energies, both cascade models, i.e. *Bertini* and *Binary* INC (see A.1), were applied in two distinct runs, in order to compare the results. The energy points at which the response was evaluated, as well as the corresponding physics models, are given in table 4.1.

The simulations with plexiglass phantom were conducted partly on 24 CPU nodes at the Technische Universität München and partly on the four nodes on the local PC. 26 distinct neutron energies were used, ranging from $E_n = 25\,\mathrm{meV}$ to $E_n = 200\,\mathrm{MeV}$, with the parameters also given in table 4.1. One can see that in most cases, a rather high neutron fluence of $\Phi_n = 1.875 \cdot 10^6\,\mathrm{cm}^{-2}$ could be afforded due to the 24 cores available that time. For the low energies, the fluence was $500 \cdot 10^3\,\mathrm{cm}^{-2}$, since those runs were considered more time-consuming due to the higher cross sections corresponding to shorter interaction lengths (equation (2.3)). Generally, only the Binary cascade model with HP neutron package was utilized. At four energies, also thermal scattering (TS) was enabled, as described in section 4.1.3 for the Albedo sensor. In those cases, the fluence was reduced to $200 \cdot 10^3\,\mathrm{cm}^{-2}$, in order to achieve a reasonable computation time.

Response without phantom

In figure 4.19, the calculated response $\eta = \frac{R}{A}$, i.e. the probability for a incident neutron to create a count, is depicted for the sensors of the HMGU dosemeter. The calculations shown here were conducted without a phantom and with the Binary model, according to table 4.1. For the threshold settings, the values given by [25] and on page 28 were applied. This means that for the Delta D and Delta G sensors, all in all four virtual sensors are shown in the figure, since according to sections 3.3 and 3.3.2, these sensors are equipped with to different thresholds each, yielding of course two distinct count numbers corresponding to different response functions.

For the Fast sensor it can be seen that the response is zero up to a neutron energy of $E_n = 1\,\mathrm{MeV}$, which is of course due to the threshold at that value. At higher energies, the response rises quickly, until around $E_n \approx 10\,\mathrm{MeV}$ the maximal value of $R \approx 3574 \cdot 10^{-6}\,\mathrm{cm}^2$ is reached. Then, a small dip in the response occurs, because the cross section for the interaction of neutrons with hydrogen decreases, and moreover protons that are still produced deposit less energy in the active zone of the detector due to their higher range (see section 4.1.1). With further rising neutron energy however, reactions on carbon play a greater role, and also the reactions of neutrons in the Silicon detector itself, which leads to a new increase in the response.

The response of the Albedo sensor is very low for the thermal neutron energy $E_n = 25\,\mathrm{meV}$, which seems surprising considering that the cross section of reaction (3.7) according to figure

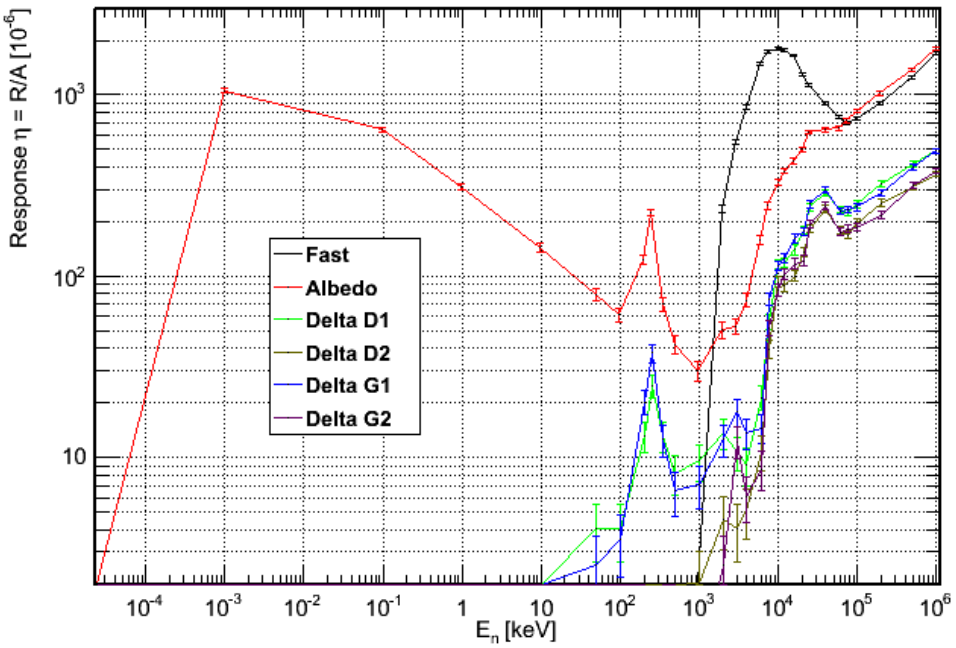

Figure 4.19.: Response functions for the sensors of the dosemeter (Deltas divided in two) obtained without phantom and the Binary cascade model. The points where the response was evaluated are indicated by the error bars; in between, a linear interpolation (on a logarithmic scale) was applied.

3.9 is very high at low energies. The reason is that in the simulated geometry, neutrons enter the sensor mainly from the front, since no phantom is present for backscattering. The hole in the Cadmium housing however is at the back side; neutrons from the front are thus effectively shielded off by the Cadmium, which has a high interaction cross section with neutrons at thermal energies (see page 35). At the next simulated energy, $E_n = 1\,\mathrm{eV}$, this cross section is already more than two orders of magnitude lower, so only the high reaction probability with ^6Li plays a role here, resulting in very high response of $R = 2086 \cdot 10^{-6}\,\mathrm{cm}^2$. With increasing neutron energy, the response decreases, since also the cross section gets lower; its excess around $E_n \approx 250\,\mathrm{keV}$ is also emulated by the response. The minimal response is around $E_n \approx 1\,\mathrm{MeV}$ with a value of $R \approx 59 \cdot 10^{-6}\,\mathrm{cm}^2$; from that energy, the response increases again, because then also scattering reactions in the converter, and at higher energies $Si+n$ reactions predominate. For $E_n \gtrsim 100\,\mathrm{MeV}$, the responses for the Fast and Albedo sensor are almost equal, as here only reactions in Silicon are important, and the threshold settings for the two sensors are the same.[5]

The response functions in figure 4.19 shown for Delta D1 and Delta G1 are very similar, since of course these correspond to the same threshold settings in two equal sensors (see description on page 35). Their response starts at neutron energies around $E_n = 10 \ldots 100\,\mathrm{keV}$

[5] In fact, the Albedo response is even slightly higher because for that sensor, less material (converter etc.) is in front of the sensor.

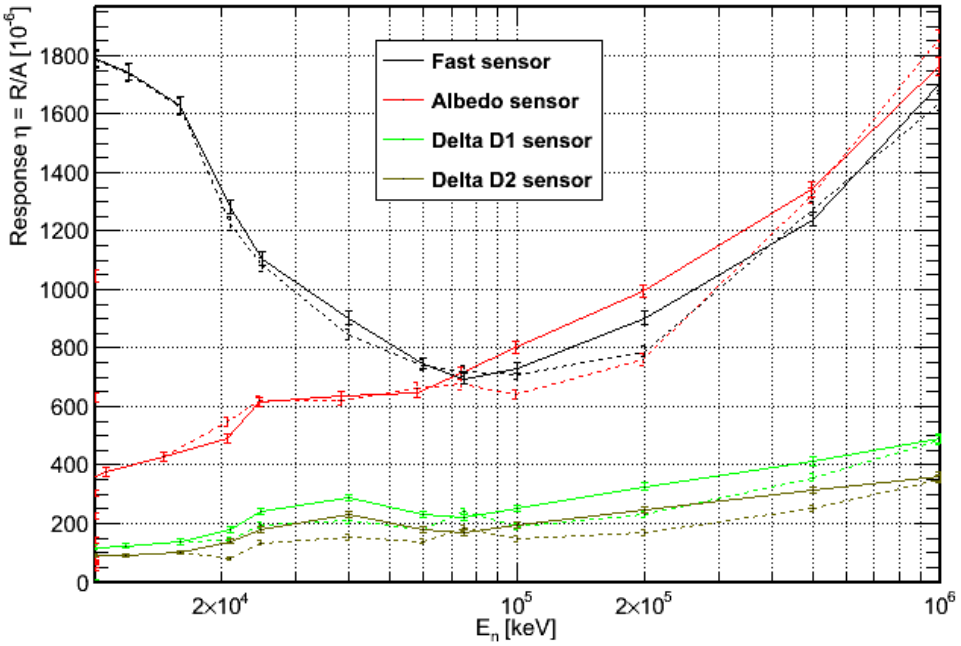

Figure 4.20.: Response functions of the Fast, Albedo and Delta sensors, obtained without phantom and two different physics models above $E_n = 20\,\mathrm{MeV}$. The solid lines corresponds to the *Binary* model, the dotted lines to the *Bertini* one.

only, since below the kinetic energy of the produced tritium ions in the ${}^6Li\,(n,\alpha)\,{}^3H$ reaction does not exceed the threshold value $E_{thresh} = 2.8\,\mathrm{MeV}$, which can be seen from equation (3.8) and the figure on page 37. At about $E_n \approx 250\,\mathrm{keV}$, a peak in the response like for the Albedo sensor is observed, because the excess in the cross section for the above reaction applies here as well. For increasing neutron energies, more and more events result in counts due to the increasing kinetic energy of the reaction products, yielding a rising response. For high energies, scattering in the converter and also direct reactions in Silicon play the main role; thus, one can see that for neutron energies higher than $E_n \gtrsim 100\,\mathrm{MeV}$, the progress for the Delta D and Delta G sensors is the same as for Fast and Albedo. The total response of the Deltas is however lower, which is of course due to the higher threshold leading to less counts.

For the second threshold setting of the Deltas, corresponding to Delta D2 and G2, the responses follow the ones of Delta D1 and G1; the overall level is lower because of the increased threshold. The main difference is that they start to create counts at around $E_n \approx 1\,\mathrm{MeV}$ only, since below no signals with $E_{coll} > E_{thresh} = 3500\,\mathrm{keV}$ can be created.

As indicated in table 4.1 on page 67, for the simulations without the phantom included in the geometry, not only the GEANT4 *Binary* cascade model ([79]) was used, but also the *Bertini* model ([80, 81, 79]),yielding different cross sections above 20 MeV. A comparison in terms of the calculated response of the Fast, Albedo and Delta D sensor (The situation for Delta G is quite the same.) is shown in figure 4.20. One can see that up to $E_n = 1\,\mathrm{GeV}$,

only small differences occur. The highest disagreement is observed for the Albedo sensor in the energy range $E_n = 100 \ldots 500\,\mathrm{MeV}$. In general, the outcome using the Bertini model is lower in almost all cases. Special attention has to be paid to the transition from cross section based calculations at energies below $E_n = 20\,\mathrm{MeV}$ with the HP model to intra-nuclear cascade model calculations above that value. The response functions for the Delta sensors in figure 4.20 already show that with the Bertini model, the transition is not as smooth as with Binary. This, along with the need for a high response in order to accurately reproduce measured data at high energies, lead to a decision in favor of the Binary model for the simulations with the phantom included.

According to current understanding, the choice of the appropriate model for a given problem is up to the user anyway, since in most cases no model fits best to measured data ([5, 41, 18]).

Response with phantom

The responses calculated from the simulations with phantom presented in the table on page 67 are shown in figure 4.21 for the six virtual sensors of the HMGU dosemeter. As expected, the only important difference can be seen for the Albedo sensor, because the others are not affected by backscattered neutrons much, as described in section 4.1. Below an incident neutron energy of about $E_n \approx 10\,\mathrm{MeV}$, these neutrons play a dominant role and enhance the response of the Albedo sensor considerably. From $E_n \approx 1\,\mathrm{eV}$ to around $E_n \approx 350\,\mathrm{keV}$, the response is almost uniformly at a high value of $R > 2000 \cdot 10^{-6}\,\mathrm{cm}^2$. The decline with higher energies in that region as well as the excess around 250 keV observed in the simulations without phantom is no longer visible here. This is of course due to the huge amount of scattering that occurs in the phantom; i.e., the neutrons entering the phantom with a incident energy of E_n do no longer enter the sensor with about that energy, so characteristics like the peak in figure 4.19 above vanish. Neutrons with relatively high energy, i.e. $E_n \geq 100\,\mathrm{eV}$, are scattered down to thermal energies before they reach the sensor, and so the response in this energy region is greatly enhanced. For low neutron energies however, the range in the phantom is smaller as well, which affects the number of particles reaching the sensor. Thus, the response for $E_n = 1 \ldots 100\,\mathrm{eV}$ is not enhanced as greatly as for $E_n > 100\,\mathrm{eV}$.

Neutrons with thermal energy, $E_n = 25\,\mathrm{meV}$, do only seldom enter the sensor directly because of the Cadmium shielding with its high absorption cross section to low-energetic neutrons, displayed in figure 3.8. Here, however, the neutrons scattered in the phantom can reach the converter through the hole at the back side (see pages 33 and 39); the response at that incident energy thus benefits much from the presence of a phantom a lot.

At several hundreds of keV, the response of the Albedo begins to decrease as in figure 4.19; this is because here, the neutrons leaving the phantom after scattering have higher energies, resulting of course in a lower cross section of the conversion reaction (3.7) and thus fewer counts. The lowest response is found at around $E_n \approx 4\,\mathrm{MeV}$ with a values of $R \approx 650 \cdot 10^{-6}\,\mathrm{cm}^2$.

Just as without phantom, at higher neutron energies scattering in the converter and direct

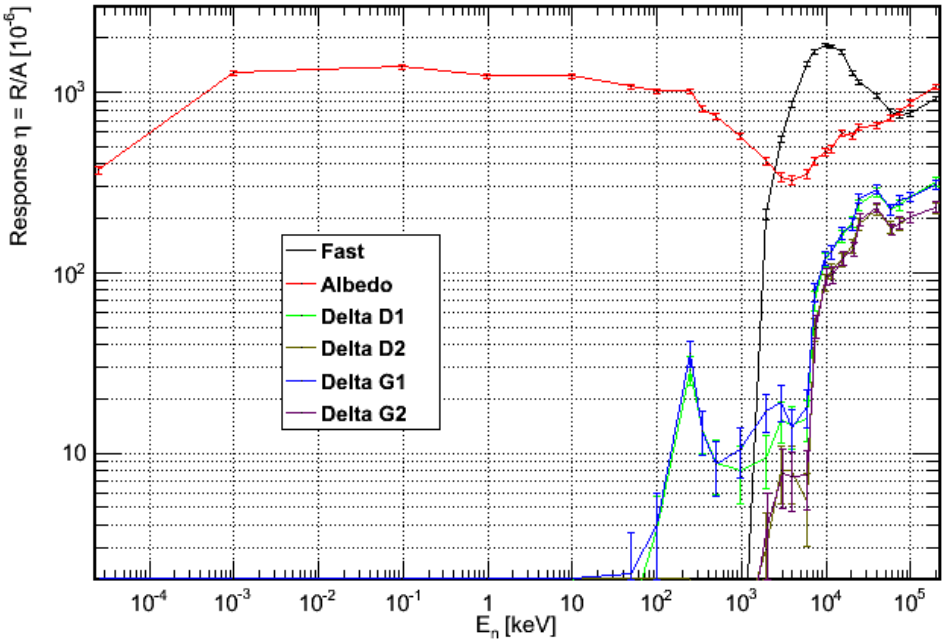

Figure 4.21.: Response functions for the sensors of the dosemeter (Deltas divided in two) obtained with phantom and the Binary cascade model (but without thermal scattering). The points where the response was evaluated are indicated by the error bars; in between, a linear interpolation (on a logarithmic scale) was applied.

reactions in Silicon become more and more important; at $E_n \geq 100\,\mathrm{MeV}$, these direct $Si + n$ interactions are dominant, and thus the responses for the Fast and Albedo sensor are almost equal again.

As outlined in table 4.1, responses have been calculated from the pulse height spectra obtained with activated thermal scattering (TS) physics in the phantom as well. The corresponding spectra have been described in the discussion of the Albedo sensor already; here, mainly the influence on the response is of interest. It has been shown thoroughly that the Albedo sensor is the only one on whose count number and hence its response the phantom has a significant influence. Since the TS cross sections were applied for the material the phantom consists of, that is, plexiglass (which is a rough approximation only; see supplement A.2), only a difference in that response can be expected.

Figure 4.22 shows again the response functions of the Albedo sensor at various incident neutron energies, acquired both with and without phantom. The outcome calculated with the $S(\alpha, \beta)$ matrix is displayed, too, that is the response found at the four neutron energies $E_n = 25\,\mathrm{meV}$, $E_n = 1\,\mathrm{eV}$, $E_n = 10\,\mathrm{keV}$ and $E_n = 10\,\mathrm{MeV}$. The TS cross sections apply for the interactions of neutrons below 4 eV ([76, 77]); it was thus expected that the response at the two higher incident energies is not altered very much. Instead, the outcome of the analysis indicates that the discrepancy between calculations with and without TS enabled is highest at around

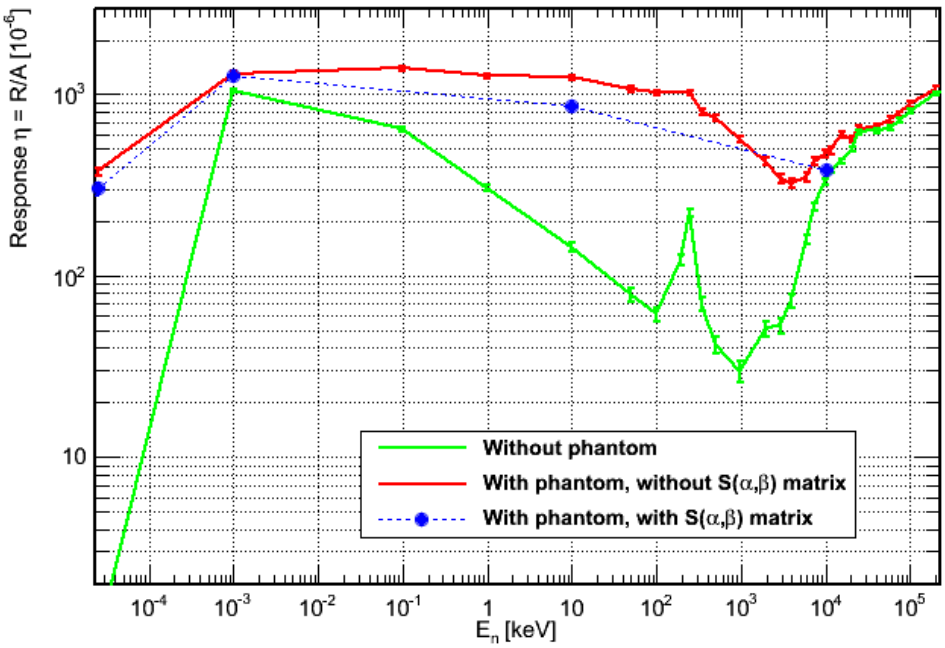

Figure 4.22.: Response functions for the Albedo, obtained without phantom (green), with phantom and the the standard high precision neutron package (red) and with thermal scattering (blue). The energies where the response was evaluated are indicated by error bars or points; in between, a linear interpolation (on a logarithmic scale) was applied.

$E_n = 10\,\mathrm{keV}$, in accordance with the pulse height spectra on page 64. This is understandable, since in that energy region, the influence of the phantom is highest. Neutrons entering it with $E_n = 10\,\mathrm{keV}$ are scattered down to thermal energies very effectively according to the HP physics; that behavior is obviously slightly altered with thermal scattering. For $E_n = 1\,\mathrm{eV}$, the phantom influence in contrast is small; thus, also the TS cross sections change not much on the calculated response. The same is true for $E_n = 10\,\mathrm{MeV}$. Here, neutrons undergo most of the scattering steps in an energy range where the TS physics is not applicable anyway.

At $E_n = 25\,\mathrm{meV}$, the influence of the phantom is huge; nevertheless, the change in cross sections caused by the TS model is also unimportant here. This is because the great discrepancy in response between the simulation with phantom and the one without in figure 4.22 is merely caused by the presence of the scattered neutrons at all; the composition of the phantom, and thus also the application of the $S(\alpha, \beta)$ matrix, plays a relatively small role in comparison. Moreover, only very few scattering steps occur in this situation due to the low range of thermal neutrons in the phantom; thus, small deviations in the cross section of each scattering event do not accumulate as much as for example with $E_n = 10\,\mathrm{keV}$. The third reason for the little influence of the TS model at thermal energies however is that with $E_n = 25\,\mathrm{meV}$, the neutrons incident on the phantom are in thermal equilibrium with the latter. In inelastic scattering processes, the energy gain and loss of the neutrons are roughly balanced then.

Considering that the $S(\alpha, \beta)$ matrix is designed to describe such processes (which e.g. involve molecular vibrations etc.), it is clear that here its overall impact is marginal.

The similarity observed in the calculation both with and without thermal scattering puts forward that for a qualitative, and over a wide energy range also quantitative, discussion of the dosemeter´s response this augmented physics is not needed. Basic features as well as the most important characteristics of all sensors, including the Albedo one, can be investigated in Monte Carlo simulations applying the procedure described in A.2 without the $S(\alpha, \beta)$ matrix. Given that the application of polyethylene cross sections to plexiglass is a rough approximation only as well, which needs not even be better than the one provided by just using the High Precision neutron package down to thermal energies, spending additional computation time on the energy points not yet considered in figure 4.22 can be regarded unnecessary.

5. Experimental validation and investigation

Besides the simulations of the HMGU dosemeter described exhaustively in chapter 4, in this work several measurement campaigns with the dosemeter prototypes (figures on page 14) were conducted. On the one hand, these measurements served for the acquisition of data that could then be compared to the simulations described above; in order to do that, the *calculated* response for a spectrum yielded by equation (A.7) is compared to the *measured* response, which is given by the number of counts registered and the fluence of neutrons, according to (A.5). As mentioned in the introduction of chapter 4, the comparison of measured results obtained with a neutron energy spectrum to the simulated responses serves as a verification of those simulations, which is necessary if one wants to rely on the data produced by the same simulations that is not accessible via measurement. For the three different neutron fields presented in this chapter, the comparison with simulation is described in section 5.4.

All experiments in this work were done with the new generation dosemeter prototypes described in [25]. The output was thus just the number of *counts* acquired in each sensor Fast, Albedo, Delta D1, G1, D2 and G2 over the measurement time. Although with this configuration no pulse height spectra could be acquired for the single sensors (unless the method in [25] was applied), the comparison with simulations in terms of response as done here is adequate for a thorough verification.

On the other hand, all of the measurements conducted and explained in this thesis served a special purpose. The three experimental setups were at least partly dedicated to the investigation of interesting properties of the dosemeter. The experiment at the Helmholtz-Zentrum Berlin (HZB) was designed to test the linearity of the dosemeters in a pulsed neutron field. Measurements with the Americium-Beryllium (AmBe) neutron source of the HMGU were conducted in order to check the results given in [25] and to investigate the influence of a different experimental setup on the sensor readings. And, in the experiment done at the Zugspitze mountain, it was possible to get an impression of the dosemeters´ response to cosmic radiation, including also other particles beside neutrons.

5.1. Dosemeter test in pulsed fields

The problem of pile-ups in electronic dosemeters which work in pulse-counting mode was shortly described in section 3.1 already. For most devices, including REM counters, these

pile-up events reduce the response to radiation in fields with a very high fluence rate ([16, 17, 18, 19, 11]). This issue is especially important when dealing with *pulsed* radiation fields, that is with fields in which the total fluence is concentrated in short time intervals with very high *fluence rate* and relatively long time gaps in between, when the fluence rate can be considered zero. Such a time interval with high fluence rate is denoted as a *burst*. Pulsed radiation fields can for example be present during the operation of medical or scientific accelerators. It is thus very important to characterize the behavior of the HMGU dosemeters at pulsed radiation and high fluence rate, since this is one of the intended fields of application for those devices.

In the frame of the EURADOS working group 11,[1] an experiment at the Helmholtz-Zentrum Berlin für Materialien und Energie (HZB) was organized, which was designed as an intercomparison of the behavior of both ambient and personal dosemeters in a pulsed neutron field of high energy. The whole experiment as well as the results are described in detail in [18]. For this thesis, only the performance of the HMGU dosemeter is of interest. Thus, for all sensors of this dosemeter, both the response and the linearity between the count rate and the fluence rate is investigated.

5.1.1. Experimental setup at the Helmholtz-Zentrum Berlin

The neutron field that was used in the measurement campaign at the HZB was produced by a proton accelerator, which is actually employed in hadron radiotherapy of eye cancers ([82]). The protons in the emitted beam had an energy of $E_p \approx 68\,\mathrm{MeV}$. They hit a tungsten target included in a holding geometry, which is shown in figure 5.1. The diameter as well as the thickness of the tungsten target itself were 20 mm; it was fastened by a copper holder, which had been plugged in a polyethylene cylinder. The holder was situated in a Aluminum vessel which was mounted on the beam tube coming from the accelerator.

By (p, n) reactions in the tungsten target, the incident protons produced a neutron field with non mono-energetic energy distribution, but a maximal kinetic energy of the neutrons of $E_n \approx E_p \approx 68\,\mathrm{MeV}$. The dosemeters that were irradiated with that field were attached to a plexiglass phantom as can be seen in figure 5.2. Four devices were taken for the measurements, with the prototype numbers 106, 108, 102 and 114. Those four dosemeters show only negligible differences in response at high energies ([25]). In the analysis of the experiment, thus, not the number of the device but the position on the phantom surface is of interest. These positions are numbered HMGU 1 to 4; figure 5.2 is labeled accordingly. The phantom was placed in a distance $d = 50\,\mathrm{cm}$ from the target with help of a laser.

As already mentioned, the predominant aim of this experiment was to determine the behavior in pulsed fields; the primary proton beam was thus of course also pulsed with a repetition frequency of the bursts of $f = 100\,\mathrm{Hz}$. The pulsed characteristics of the beam was achieved by a deflection technique described in more detail in [18]. The available burst durations were $t_B = 1\,\mu\mathrm{s}$ and $t_B = 10\,\mu\mathrm{s}$. By varying the burst current I_B (i.e., the proton fluence rate) and

[1] http://eurados.org/en

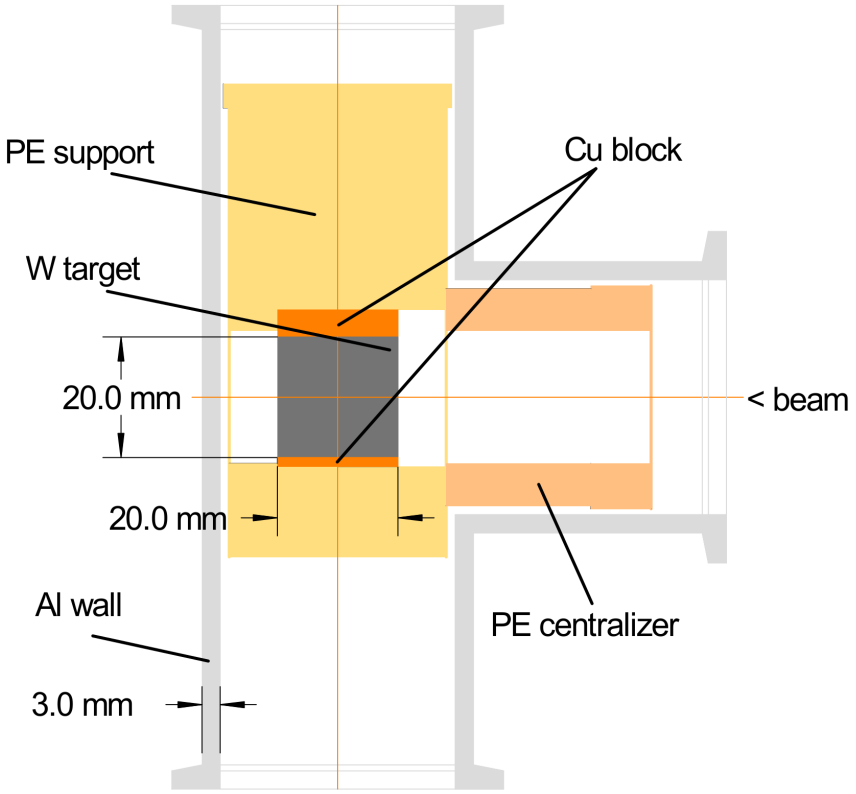

Figure 5.1.: Schematic drawing of the target holder used in the HZB experiment (from [18])

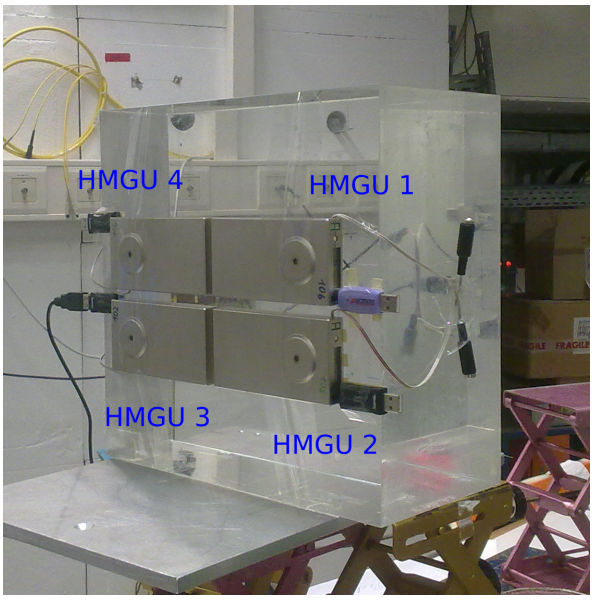

Figure 5.2.: Photo of the HMGU dosemeters attached to a plexiglass phantom at the experimental location. The positions one to four are indicated with labels corresponding to the ones in [18]

Setting	t_B [μs]	I_B [nA]	$\dot{\Phi}_n$ [$\mathrm{cm^{-2}s^{-1}}$]	t_m [s]
1	1	4.741	20.13	900 ± 5
3	1	30.266	128.49	1080 ± 5
5	1	121.575	516.12	600 ± 5
7	1	476.501	2022.88	360 ± 5
8	1	710.348	3015.63	360 ± 5
9	1	1004.657	4265.05	360 ± 5
12	10	1037.999	44065.96	360 ± 5

Table 5.1.: Beam settings, i.e. burst duration t_B, burst current I_B, neutron fluence rate $\dot{\Phi}_n$ at the phantom position, and irradiation times $t_m \pm \Delta t_m$ used for the HMGU dosemeters at the HZB experiment. The bust duration was fixed, the burst current was taken from a log-file. The neutron fluence rate was calculated according to section 5.1.2.

t_B, it was possible to achieve different fluence rates of neutrons and thus different dose rates. Distinct combinations of those two parameters were available for measurement in so-called beam settings; the measurement duration at each beam setting was up to the experimentalist. For the irradiation of the HMGU dosemeters, seven out of twelve beams settings were used, which are given in table 5.1 along with the applied irradiation times; the uncertainty in the latter is an estimated value.

During measurement, the proton current was constantly monitored with a Faraday cup and the obtained values were stored in a log-file. The burst current I_B in table 5.1 is the mean of the values in this log-file, corresponding to the appropriate beam setting. The neutron *fluence rate* $\dot{\Phi}_n$ also shown in the table was derived from a Monte Carlo simulation, which is described in the next section.

5.1.2. Simulation of the experiment

For the discussion of the linearity $\dot{N}_c \overset{?}{\propto} \dot{\Phi}_n \propto \dot{H}^\star(10)$ as done in [18], only the calibration factor $\frac{\mathrm{d}H^\star(10)}{\mathrm{d}Q_p}$, i.e. the dose per amount of proton charge is required. For a thorough analysis however, as well as for a comparison of the acquired response with simulation results, more information on the neutron field is necessary. Thus, it was decided to simulate the experiment with Monte Carlo methods, that is with GEANT4.

With the simulation, both the neutron fluence distribution on the phantom surface and the energy spectrum of the neutrons were investigated. In order to do that, the geometry depicted on the preceding page was implemented as far as it was considered necessary in an appropriate C++ class. That is, the tungsten target, the target holders made of copper and polyethylene and the tube containing the setup were modeled; a visualization of this implementation is given in figure 5.3. As a scorer, a new class was constructed, reading out both position and kinetic energy of neutrons passing a $30 \times 30\,\mathrm{cm}^2$ layer which was positioned 50 cm from the target, just like the phantom in the experiment. These values were written to a table in the MYSQL database (just as depicted on page 139).

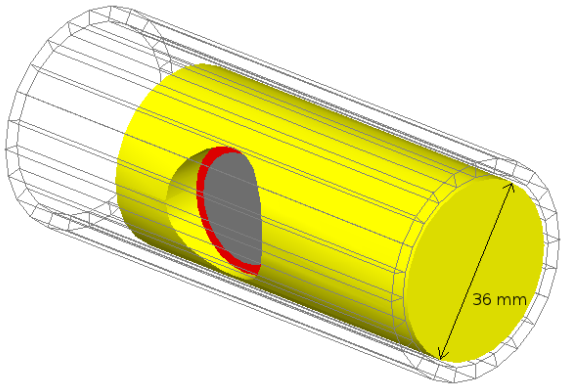

Figure 5.3.: View of the geometry used for the simulation of the HZB experiment, created with the GEANT4 OpenGL renderer ([27])

The choice of the appropriate physics list for this simulation is not an easy task. Unlike for neutrons, the interactions of protons (in this case with tungsten) are governed by the intra-nuclear cascade models, as well as the attached evaporation model, see [79], completely, that is down to very low energies. Although the HP package was employed in order to correctly simulate the interactions of the secondary neutrons with the material surrounding the target, the main differences in the simulation results are expected to stem from the choice between *Bertini* and *Binary* INC model. Thus, two separate applications were created, containing both variations of the physics list outlined on page 141, i.e. both of the models were tried.

The remaining implementation of the GEANT4 applications followed the principles also applied in the case of the dosemeter simulations. That is, also user interface commands, visualization, parallelization and a *Monitor* class were added. For a detailed description of these classes, see supplement 3.3.

The simulations were run on four (virtual) CPU nodes on a local computer. For the simulation with the Bertini model, $300 \cdot 10^6$ primary protons were used; the one with the Binary model was run with $100 \cdot 10^6$ protons. Using ROOT, the data was retrieved from the MYSQL table and analyzed with a dedicated script.

The result given in figure 5.4, which can also be found in [18], shows the simulated spatial fluence distribution on the phantom surface. This outcome was acquired with the Bertini model. One can see that in the center of the area, a fluence exceeding $\frac{\mathrm{d}\Phi_n}{\mathrm{d}N_p} \approx 6.8\,\mathrm{cm}^{-2}$ per proton can be achieved. To the edges, this value decreases slightly to around $\frac{\mathrm{d}\Phi_n}{\mathrm{d}N_p} \approx 5.2\,\mathrm{cm}^{-2}$ per proton. This distribution is of course dominated by the different distances to the phantom; at the edges, this distance is higher, so the solid angle corresponding to a unit area is lower. Moreover, the emission of neutrons in the (p, n) reactions with tungsten in forward direction

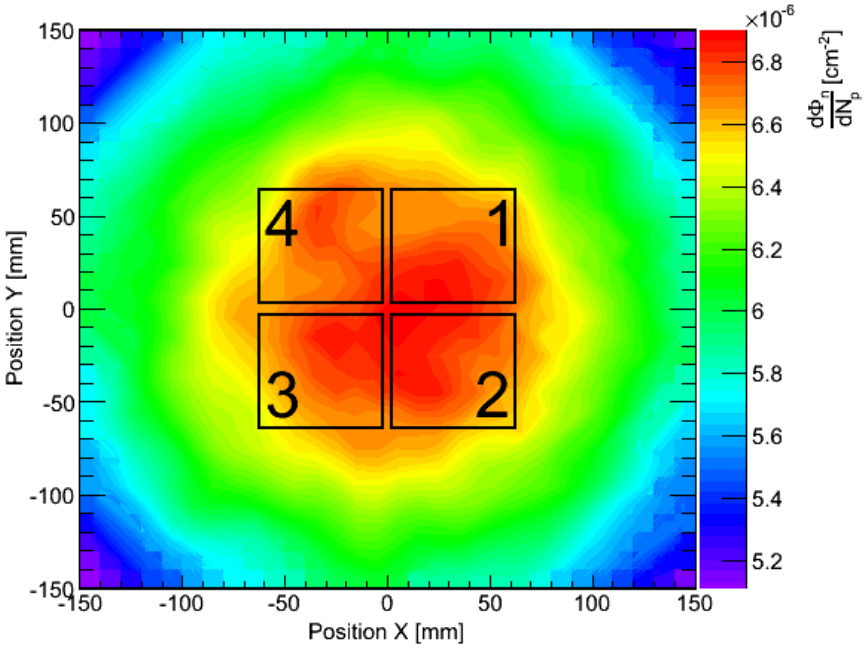

Figure 5.4.: Spatial neutron fluence distribution per incident proton at the HZB experiment on the $30 \times 30\,\mathrm{cm}^2$ phantom surface in a distance $d = 50\,\mathrm{cm}$ from the target. The positions of the four dosemeters during measurement (see figure 5.2) are labeled.

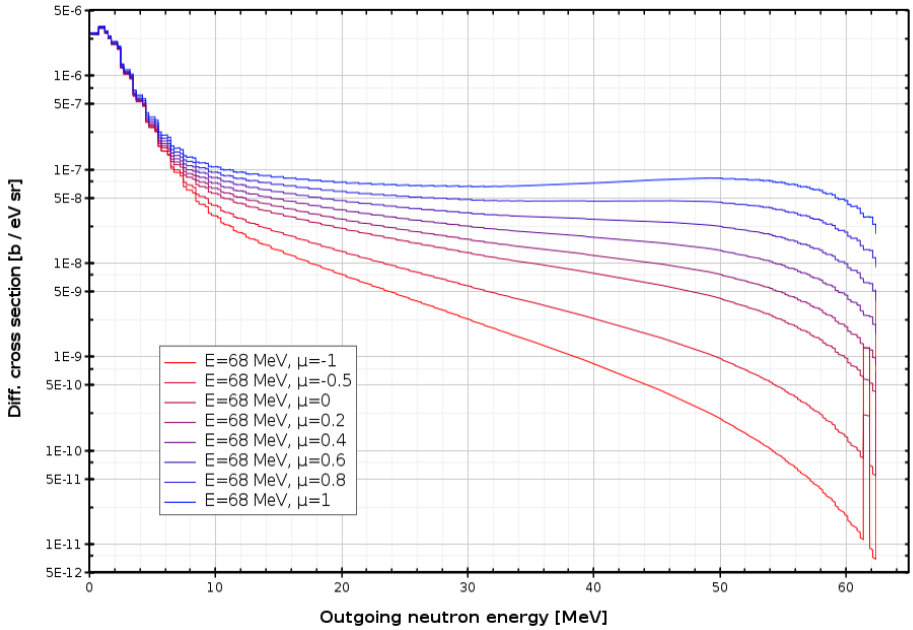

Figure 5.5.: Differential cross sections $\frac{\mathrm{d}^2\sigma_{p,n}}{\mathrm{d}E_n \mathrm{d}\Omega}$ for the emission of neutrons in the (p, n) reaction on the tungsten isotope ^{184}W, for a incident proton energy of $E \equiv E_p = 68\,\mathrm{MeV}$. μ denotes the cosine of the emission angle.

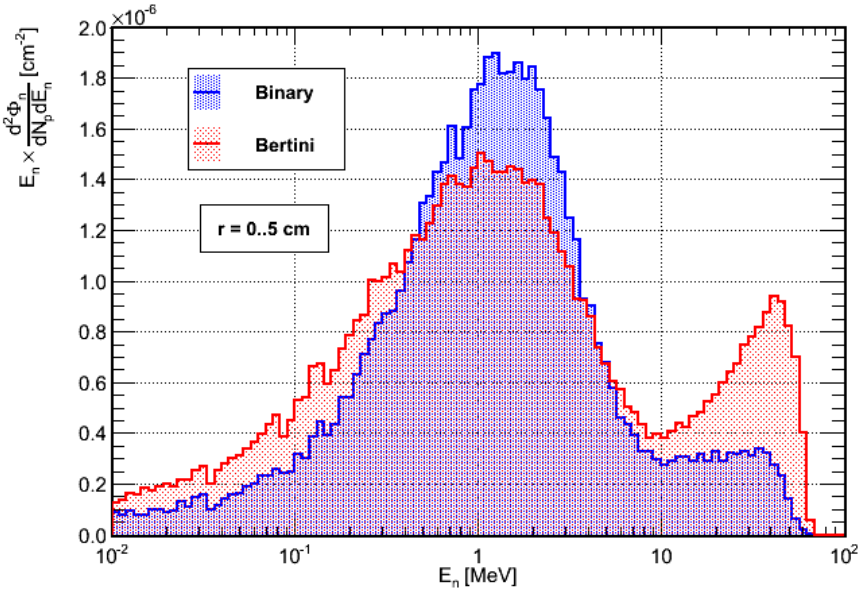

Figure 5.6.: Neutron energy spectra (lethargy representation) in the central circular area of figure 5.4 calculated with both Binary and Bertini INC model and scaled with the number of incident protons on the target.

is slightly preferred over the emission in other directions. This can be estimated from the *differential cross section* shown in figure on the preceding page at the example of ^{184}W, which is the main tungsten isotope with an abundance of around 30.67 %. As shown there, the emission of the created neutron at an angle $\arccos(\mu = 1) = 0°$ is the likeliest case. Although the emission angle corresponding to the very edge of the phantom surface is around 23° only, i.e. $\mu \approx \cos(23°) \approx 0.92$, this effect along with the variation in distance explains the distribution of fluence in 5.4.

Within a circular area of radius $r = 5\,\mathrm{cm}$, the fluence can be considered almost constant. The seemingly lower values at the HMGU 4 position in the picture must be regarded a statistical effect. By integration, the mean fluence in the central circle with $r = 5\,\mathrm{cm}$ is found to be $\frac{\mathrm{d}\Phi_n}{\mathrm{d}N_p} = 6.802\,\mathrm{cm}^{-2}$ per incident proton. The corresponding value calculated with the Binary model is $\frac{\mathrm{d}\Phi_n}{\mathrm{d}N_p} = 5.956\,\mathrm{cm}^{-2}$, as with this physics list, the overall fluence is slightly lower. The shape of the spatial fluence distribution however looks exactly the same as shown for the Bertini model in figure 5.4 and is therefore not displayed separately. The total fluence rates in the central area tabulated in table 4.1 on page 67 were obtained by multiplying the number of protons per second (given by the burst current I_B, the burst duration t_B and the burst repetition rate $f = 100\,\mathrm{Hz}$) with the fluence per proton, i.e.

$$\dot{\Phi}_n = \frac{\mathrm{d}\Phi_n}{\mathrm{d}t} = \frac{\mathrm{d}N_p}{\mathrm{d}t} \cdot \frac{\mathrm{d}\Phi_n}{\mathrm{d}N_p} = f \cdot \frac{I_B \cdot t_B}{e} \cdot \frac{\mathrm{d}\Phi_n}{\mathrm{d}N_p} \tag{5.1}$$

For that, the value $\frac{\mathrm{d}\Phi_n}{\mathrm{d}N_p} = 6.802\,\mathrm{cm}^{-2}$ calculated with the Bertini model was used.

Method	$\frac{\mathrm{d}H^\star(10)}{\mathrm{d}Q_p}$	$\frac{\mathrm{d}H_p(10)}{\mathrm{d}Q_p}$
Bertini	$14.67\,^{\mathrm{nSv}}/_{\mathrm{pC}}$	$15.06\,^{\mathrm{nSv}}/_{\mathrm{pC}}$
Binary	$12.87\,^{\mathrm{nSv}}/_{\mathrm{pC}}$	$13.31\,^{\mathrm{nSv}}/_{\mathrm{pC}}$
PHITS	$17.1\,^{\mathrm{nSv}}/_{\mathrm{pC}}$	$17.5\,^{\mathrm{nSv}}/_{\mathrm{pC}}$
Experimental	$15.4 \pm 1\,^{\mathrm{nSv}}/_{\mathrm{pC}}$	—

Table 5.2.: Ambient and personal dose equivalent per proton charge obtained by Monte Carlo simulation and measurement for the HZB experiment. Value obtained with the PHITS code ([83]) and experimental value ([84]) taken from [18].

Results for the energy distributions also scored in the simulation of the experiment and analyzed with the same ROOT script are shown in figure 5.6. These distributions are given in lethargy representation, that is the energy bins are equidistant on a logarithmic scale and each bin content is scaled with its mean energy. Thus, a certain area under the graph corresponds directly to the fluence portion in that area, if the energy axis is drawn logarithmically. This representation gives more details on the energy spectrum if the energy range to be drawn is very wide and reveals characteristics that would not be noticeable in a representation with linear energy but logarithmic fluence axis.

Such a characteristic is for example the peak at high neutron energies in the spectrum calculated with the Bertini model, which is shown in figure 5.6. The energy spectra depicted there correspond to the central circular area on the phantom, as shown on page 80. One can see that with the Binary model, the fluence at high neutron energies is much lower, as well as the overall fluence. The *Evaporation Peak* around $E_n \approx 1\,\mathrm{MeV}$ is however higher with this model.[2] The two spectra were multiplied with the h_p and $h^\star$ fluence-to-dose conversion factors and integrated according to equation (2.5). This yielded values both for the ambient and personal dose equivalent at the dosemeters´ position per incident proton on the target. In table 5.2, the calculated values $\frac{\mathrm{d}H_p(10)}{\mathrm{d}Q_p}$ and $\frac{\mathrm{d}H^\star(10)}{\mathrm{d}Q_p}$ for both INC models are given. As a comparison, also some of the results presented in [18] are shown. One can see that for the ambient dose, the value simulated with the Bertini model fits very well to the measured one gained with the LUPIN ([84]) device. Moreover, the spectrum created with that model shows similar characteristics than the one calculated with the PHITS code ([83]), as in the latter also a peak at high neutron energies is observed.[3] Therefore, for the analysis in 5.1.3 as well as for the comparison with the dosemeter simulation on page 107, the results calculated with the Bertini model were chosen.

When looking at the spatial neutron fluence distribution on page 80, it can be questioned whether fluence rate and energy spectrum can be regarded the same at all the positions of the sensors in the four HMGU dosemeters attached to the phantom. In figure 5.7, the spectra are shown for the three different positions within the dosemeter head; they were averaged among the four dosemeters in order to gain a better statistics. Since the spatial distribution is radially

[2] For a description of the origin of that peak, see e.g. [28]
[3] M. Luszik-Bhadra (PTB), private communication

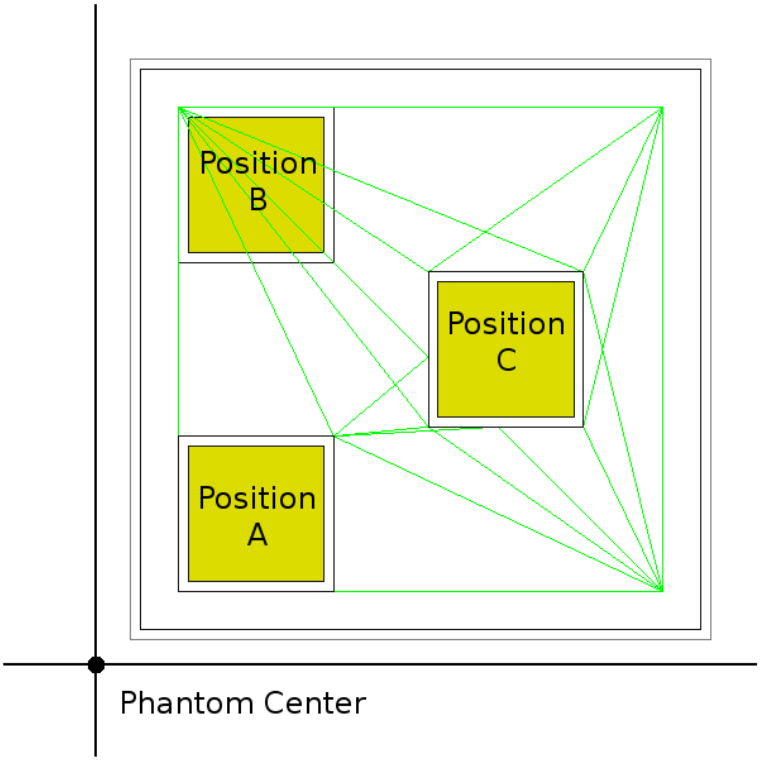

(a) Positions of the sensors labeled A, B and C in 5.7b below, with respect to the phantom center for HMGU 1.

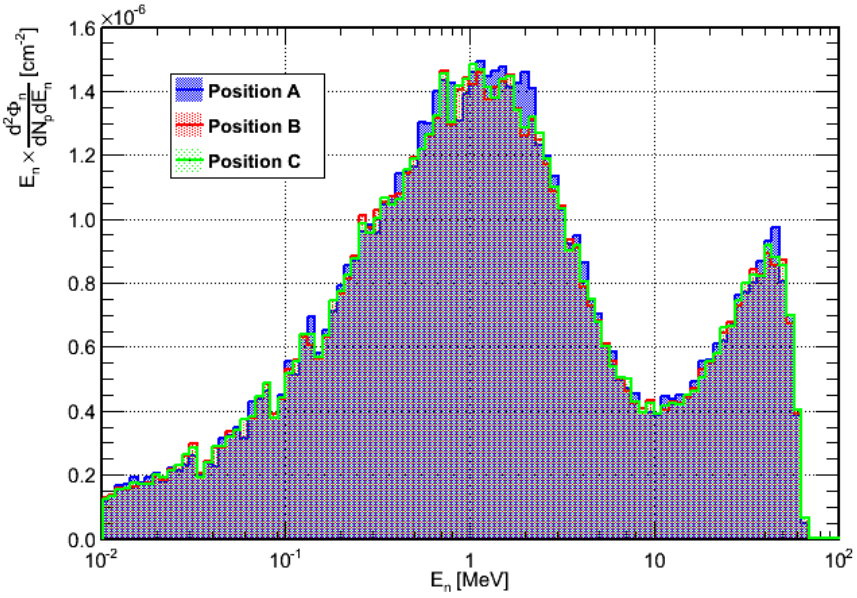

(b) Mean neutron energy spectra (lethargy representation) at the positions of the sensors in the HMGU dosemeter, calculated with the Bertini model and scaled with the number of incident protons on the target.

Figure 5.7.: Positions of the sensors in the HZB experiment and corresponding neutron energy spectra

symmetric, this procedure is valid. The positions A, B and C in the figure denote the three different placements a sensor can have with respect to the beam center. As an illustration of that, in 5.7a the three sensor positions are shown at the example of the HMGU 1 dosemeter position indicated on page 77. In that case, A corresponds to the Fast sensor, B to Delta D and C to Albedo and Delta G. For the dosemeters at HMGU 2, 3 and 4, the situation is of course different, but the corresponding distances of A, B, and C to the phantom center are equal.

When comparing the spectra given in figure 5.7b, it becomes obvious that the distributions can be considered equivalent at the three sensor positions. Also the totally enclosed area, i.e. the neutron fluence per incident proton, is almost the same among the spectra. This result means as well that no attention has to be paid to imaginable misalignments of the beam center in the order of several millimeters and that the same fluence and dose rate per beam setting can be ascribed to each sensor and each dosemeter in this measurement.

5.1.3. Results and discussion

Unlike in [18], not only the behavior of the dose reading H^m of the HMGU dosemeters in pulsed neutron fields was analyzed in the present work, but the linearity of each individual sensor. Here, the relationship between the count rate $\dot{N}_c$ and the mean fluence rate $\dot{\Phi}_n$ of neutrons in the various fields is investigated. In an ideal case, these quantities are proportional, i.e.

$$\dot{N}_c \overset{!}{\approx} R \cdot \dot{\Phi}_n \tag{5.2}$$

with the proportionality constant R being the *response* of the sensor in question (see page 146). $\dot{\Phi}_n$ is thereby given by the beam setting parameters and the simulated spectrum according to equation (5.1).

The graphs in figures 5.8, 5.9 and 5.10 show the relationship between $\dot{N}_c$ and $\dot{\Phi}_n$ for all sensors for the dosemeter. The linearity of equation (5.2) is analyzed independently for each position of the dosemeter on the phantom, as indicated on page 80. Additionally, the *expected* behavior of the count rate with respect to the fluence rate is given, which was obtained by multiplying the energy spectrum shown in figure on page 81 (acquired with the Bertini model) with the appropriate response function from the dosemeter simulations according to equation (A.7). The result is a purely theoretical response value, which is multiplied with the fluence rates calculated according to (5.1) - and thus also based on the simulated spectrum - to yield count rates that can be compared with the measured ones.

In most cases, the measured relationship $\dot{N}_c \propto \dot{\Phi}_n$ follows the calculated one quite closely. Especially noticeable is the outcome for the Albedo sensor in figure 5.8b; here, the linear dependency is obvious, and the discrepancies between the four positions are of minor importance. The situation is different for the Fast sensor as shown in figure 5.8a. In that case the dosemeter in position three, i.e. HMGU 3, displays a considerable excess in count rate at most measured fluence rates. During the measurement campaign, that observation was investigated

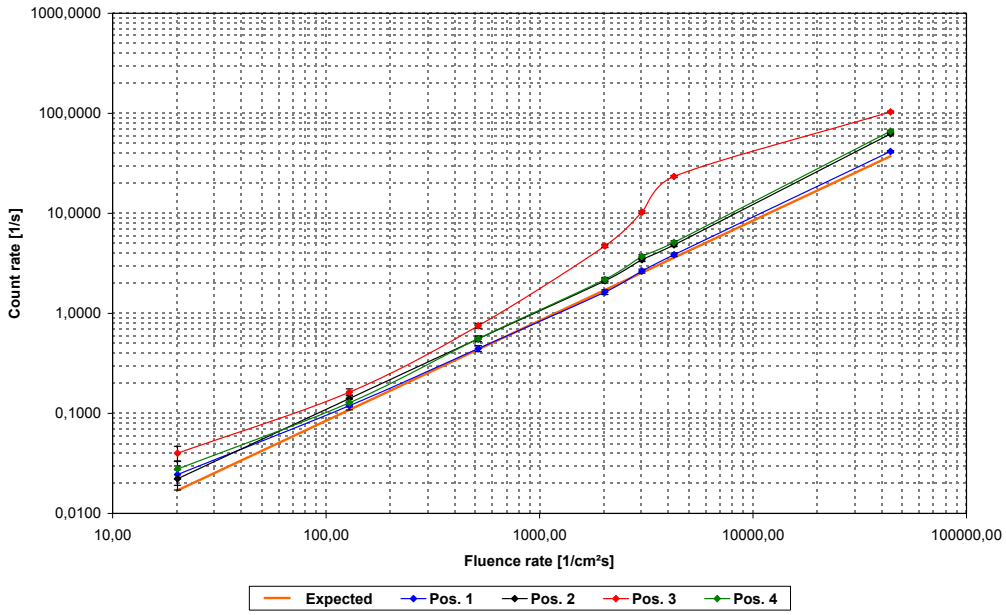

(a) Fast sensor

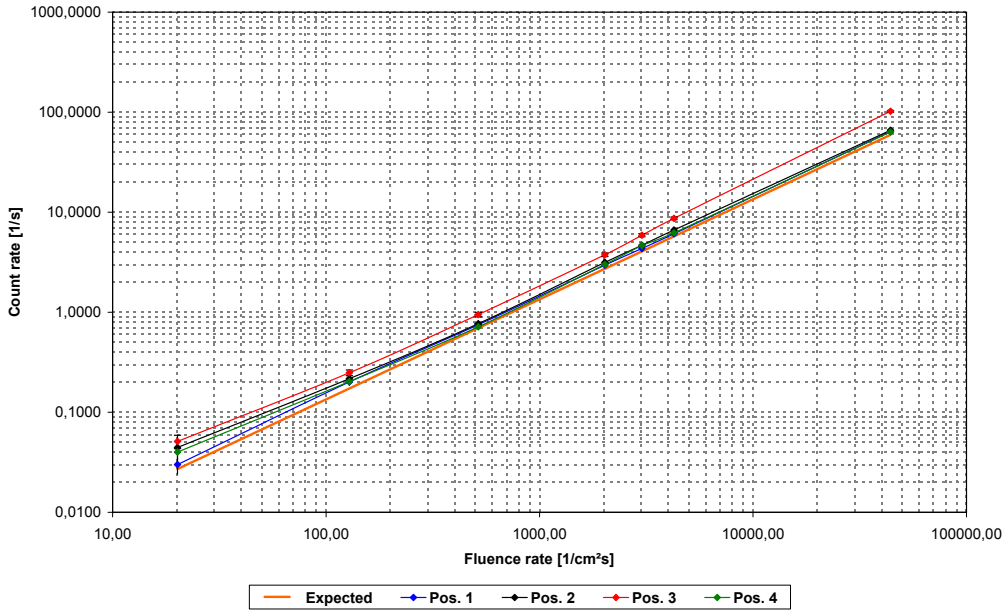

(b) Albedo sensor

Figure 5.8.: Measured count rates $\dot{N}_c$ of the Fast and Albedo sensor of the HMGU dosemeters at four positions on the phantom versus neutron fluence rate $\dot{\Phi}_n$ in the HZB experiment.

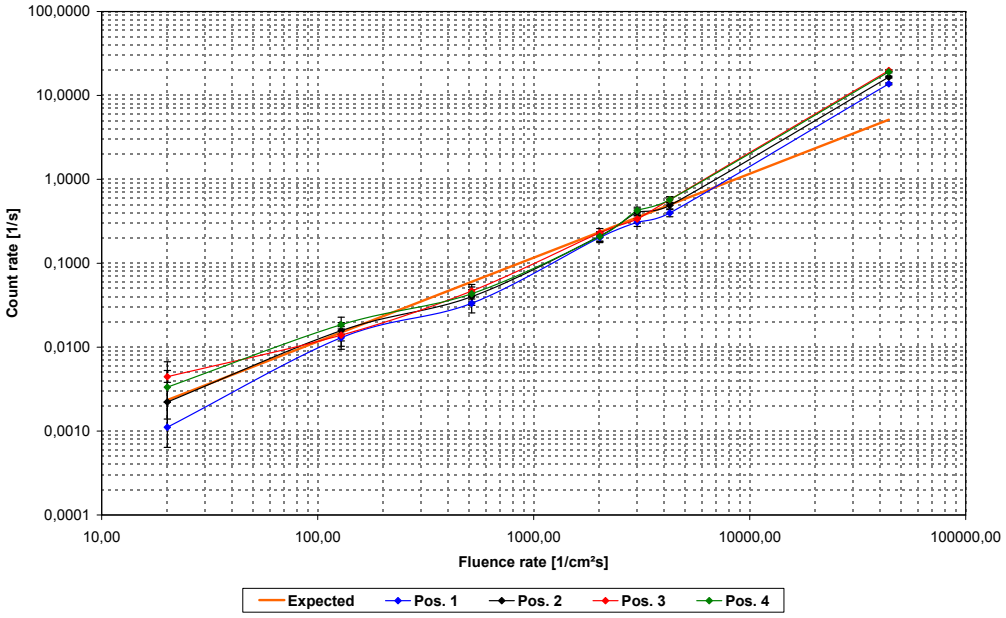

(a) Delta D1 sensor

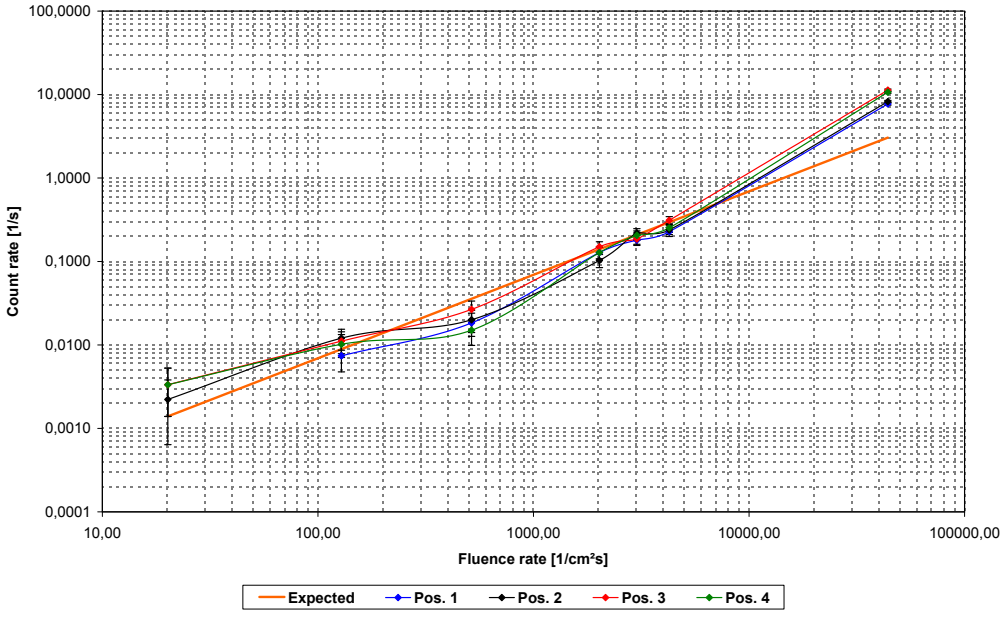

(b) Delta D2 sensor

Figure 5.9.: Measured count rates $\dot{N}_c$ of the Delta D sensors of the HMGU dosemeters at four positions on the phantom versus neutron fluence rate $\dot{\Phi}_n$ in the HZB experiment.

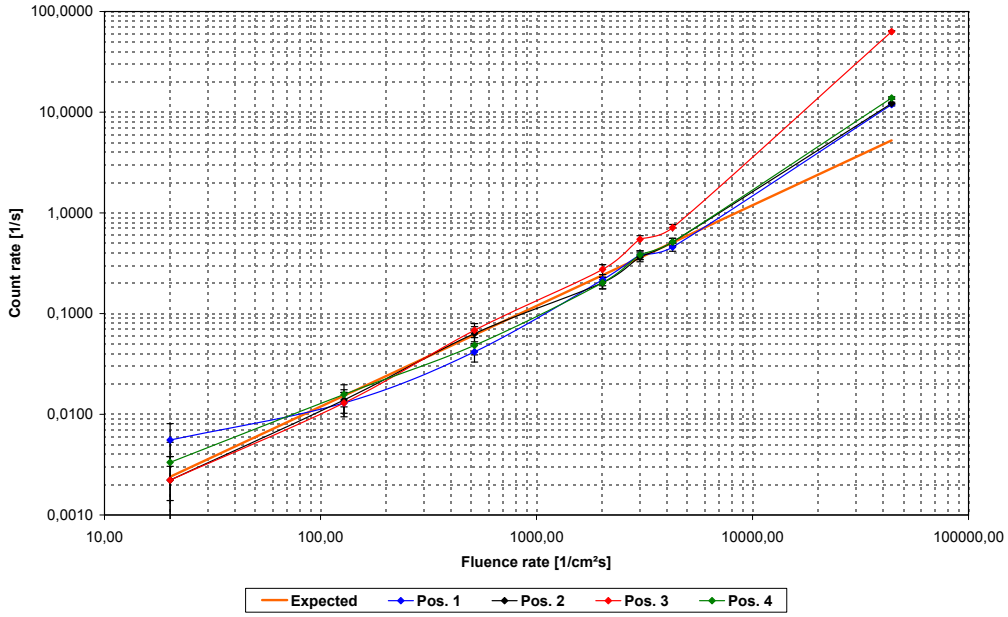

(a) Delta G1 sensor

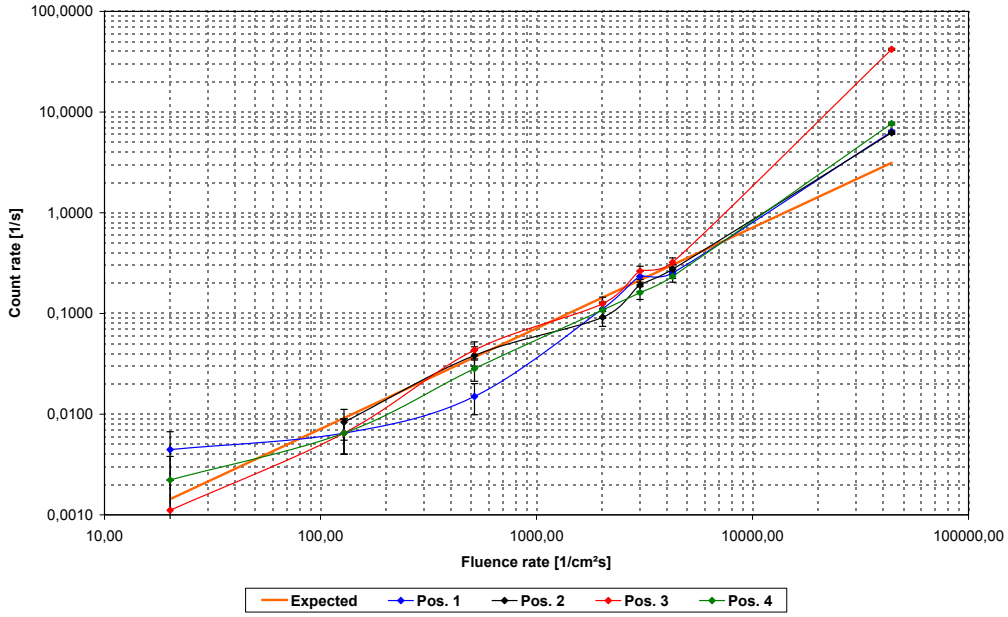

(b) Delta G2 sensor

Figure 5.10.: Measured count rates $\dot{N}_c$ of the Delta G sensors of the HMGU dosemeters at four positions on the phantom versus neutron fluence rate $\dot{\Phi}_n$ in the HZB experiment.

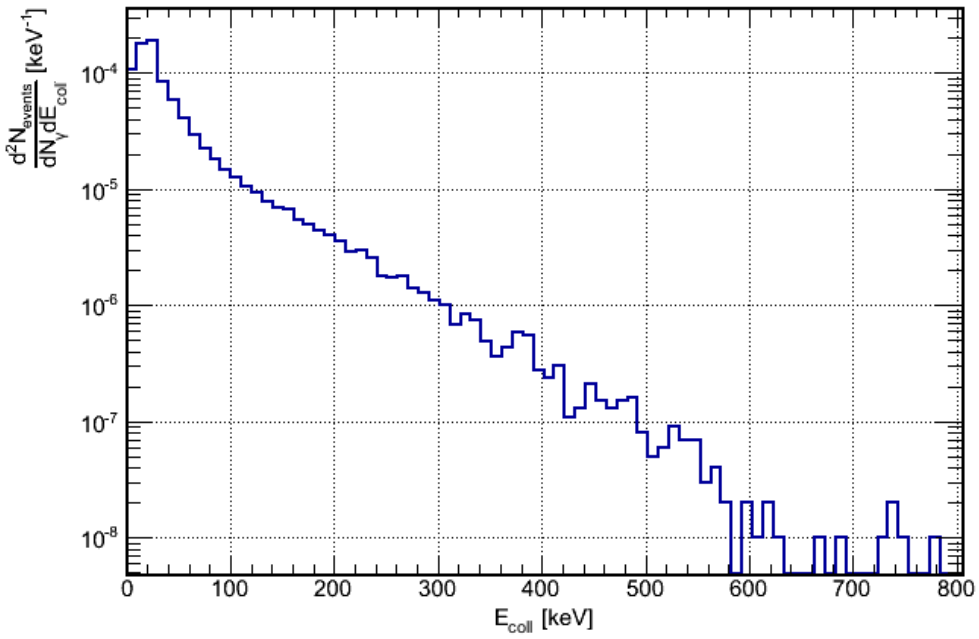

Figure 5.11.: Simulated pulse height spectrum cased by 4.5 MeV photons incident on the Fast sensor, created with $100 \cdot 10^6$ incident gamma particles. The spectra for the others sensors look similar.

more closely, since a malfunction of one of the dosemeters was anticipated. The phantom was thus rotated by 180°, so that the devices on position one and position three were swapped. Then however, still the prototype on position three showed a count rate excess in its Fast sensor. A technical fault in the dosemeter, e.g. in the electronics, is therefore considered unlikely, also taking into account that the same prototypes worked reliably in other measurements, e.g. with the AmBe source as presented on page 91. A dependency of the observed effect on the fluence rate is not visible in the figure as well, since the excess is less definite at the highest rate. It must be noted however that this beam setting, i.e. setting twelve, differs from the others in the burst duration t_B (see the table on page 78).

All in all, the reason for the behavior of the Fast count rate at position three must be ascribed to the characteristics of the experimental setup. These are probably not realized completely in the simplified simulation as presented in section 5.1.2. The latter can however be adapted to investigate the influence of the non-neutron radiation field produced by the accelerator. In the experiment, mainly the photon field is of importance, which has been analyzed in [18] by means of Monte Carlo simulations as well. In order to eliminate the idea of a possible influence of that radiation field, the simulations presented in this work were altered to score photons instead of neutrons. The resulting energy distribution, which needs not be shown here, is characterized by a broad peak around $E_\gamma \approx 1\,\mathrm{MeV}$, with the highest photon energies around $E_\gamma \approx 4 \ldots 5\,\mathrm{MeV}$. For a test, gamma particles with a energy of $E_\gamma = 4.5\,\mathrm{MeV}$

were used instead of neutrons as incident particles in a dosemeter simulation as described in chapter 4. By that, the *pulse height spectrum* in the Fast sensor created by photons could be acquired; it is shown in figure 5.11. It is obvious that for low photon fluence rates, the signals caused by incident gammas are well discriminated by the threshold setting $E_{thresh} = 1000\,\mathrm{keV}$, as already discussed in section 3.1. In [59] it has been demonstrated experimentally however that at high fluence rates pile-ups can cause signals above the threshold value and thus lead to the registration of additional counts. If this is the reason for the excess of the Fast count rate however is questionable, since such a effect can hardly be attributed to a specific position on the phantom, nor it would affect the Fast sensor only.

In accordance with [18], the excess at position three, as shown in figure 5.8a, must thus remain unexplained here. Further experimental research has to be conducted by the HZB in order to clarify that issue. Unlike in the citation, for the discussion of linearity and dose HMGU 3 is not considered in this thesis.

Figures 5.9 and 5.10 show the measured relationship between count and fluence rate for the two Delta D and Delta G sensors, respectively. A very good agreement with the expected behavior, which was again estimated from the simulation results given in 5.1.2, can be attributed for most beam settings except setting twelve, i.e. the one with the highest fluence rate. Even at other positions than HMGU 3, the count rates are significantly higher than expected at that point, which seems contradictory to the characteristics of the ambient dose meters tested in the same study ([18]), which show a lowered response at very high dose or fluence rates in most cases. Nevertheless, the increase in response of the Delta sensors is caused by pile-ups, too. In their case, signals with $E_{coll} < E_{thresh}$, which would not create counts on their own, are combined to signals with $E_{coll} > E_{thresh}$. Thus, additional counts from events below the corresponding threshold are registered in each sensor. Because of the longer shaping time, the Delta sensors are more sensitive to this effect than the Fast and Albedo sensors. The break of linearity observed for Delta D and Delta G in figures 5.9 and 5.10 is however not so severe that this experiment can be accounted a proof of a malfunction of the HMGU dosemeters at fluence rates above $\dot{\Phi}_n \approx 40 \cdot 10^3\,\mathrm{cm^{-2}s^{-1}}$. Instead, the incidence of pile-ups depends very much on the time structure of the neutron field and also on the energy of the neutrons.[4] Further measurements in pulsed fields have to be conducted for the determination for the limiting parameters on the functionality of the dosemeter prototypes.

In [18], a very good linearity between the the measured dose rate $\dot{H}^m$ and the reference dose rate $\dot{H}^\star$ (10), which scales with the fluence rate of course, is found for all dosemeters including the HMGU devices. This is due to the fact that the slight increase in the response of the Delta sensors observed on pages 86 and 87 can not be discussed in terms of dose. With the energy distributions given in figure 5.6, the sum of the responses in the first channel, i.e. $R_{D1} + R_{G2}$, is less than $c = 2.2$ times higher than $R_{D2} + R_{G2}$. Since with a fixed fluence the response

[4] The energy determines the response of the sensor in question, which according to (A.5) can be considered the probability for counting an incident neutron. The higher the response in a specific energy collection range, the higher is thus the probability for measuring two events at the same time with signal heights in that range.

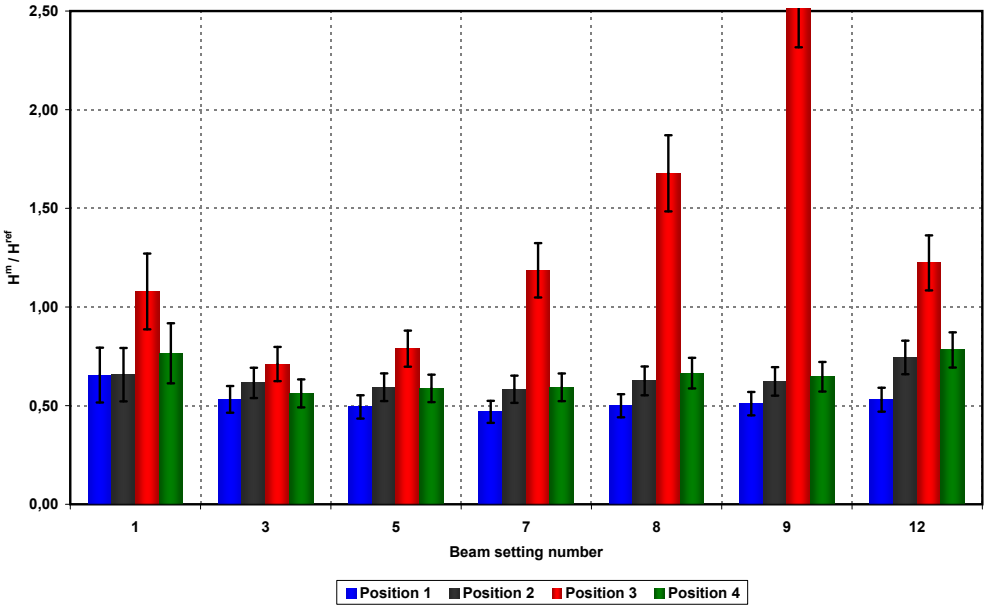

Figure 5.12.: Ratio of measured dose H^m and calculated reference dose H^{ref} for the nine tested beam settings and four dosemeter positions at the HZB experiment.

scales with the number of counts given by each sensor, the number of intermediate counts would be less than zero according to equation (3.10). The Delta sensors are thus *switched off* and are not considered in the dose assessment (3.11) at all. This behavior is triggered by the high-energetic neutrons in the HZB field, which bring forth a relatively high response of Delta D2 and G2 in comparison to D1 and G1. As given in figure 6.1a on page 115 below, the overall response of the HMGU dosemeters is very low around $E_n \approx 1\,\mathrm{MeV}$ in situations where the Delta sensors are switched off. With the HZB energy spectrum from page 81, where most of the fluence is concentrated in the evaporation peak at neutron energies just about 1 MeV, a considerable underestimation of the dose is expected.

For the various beam settings the prototypes were tested with (see table 5.1) and the four dosemeter position (figure 5.2), the dose readings H^m divided by the reference doses H^{ref} are depicted in figure 5.12. That reference dose was acquired with the value for $\frac{\mathrm{d}H_p(10)}{\mathrm{d}Q_p}$ given in table 5.2 and the appropriate proton currents for the individual beam settings. The error of the measured dose was calculated from the statistical uncertainties in the count values F_1 and A_1; for the uncertainty in the ratio, also $\Delta t_m = 5\,\mathrm{s}$ was included as a systematical error.

In the figure, one can clearly see the excess in the response of the Fast sensor at position three, which is most significant at beam setting nine. The Fast sensor has a very high influence on the complete dose reading here due to the relatively high mean energy of the neutron spectrum, as shown on page 81. At position HMGU 3, its share in the complete dose reading,

Sensor	Fast	Albedo	Delta D1	Delta D2	Delta G1	Delta G2
$R\ \left[10^{-6}\,\mathrm{cm}^2\right]$	1107.6	1528.4	116.0	61.1	113.6	58.0
$\Delta R\ \left[10^{-6}\,\mathrm{cm}^2\right]$	48.1	63.5	8.9	6.0	8.7	5.6

Table 5.3.: Mean values and uncertainties of the response R of the dosemeters´ sensors at positions two and four in beam settings three to nine at the HZB experiment

i.e. $\frac{k_1 \cdot F_1}{H^m}$, is around 88 %; in the other positions, the ratio is about 84 %. The behavior of H^m is thus essentially characterized by the response of the Fast sensor, R_{F1}. This works well for the positions different than HMGU 3, where the ratio of measured and reference dose is relatively uniform. On pages 85 to 87 above it can however be observed that at position one, i.e. HMGU 1, the response is always slightly lower than at HMGU 2 and 4. This is also visible in the dose, as indicated in figure 5.12, and must be attributed to the same unknown anisotropy in the experimental setup which also lead to the excess of the Fast count rate. For the remaining two positions, the mean ratio between measured and calculated dose is $\frac{H^m}{H^{ref}} = (62.6 \pm 2.6)$ %. For the averaging, beam setting twelve (with the highest reference dose rate) was not taken into account, since there pile-ups cannot be completely excluded.

According to equation (5.2), the responses of the several sensors were calculated from the measurement results as well. For that, again only HMGU 2 and 4 were considered; additionally, beam settings one and twelve were excluded from the averaging, because of pile-ups with the high fluence rate and insufficient statistics with the lowest. The resulting values of R are given in table 5.3. Obviously, the response of the Albedo sensor is still higher than the one of the Fast, in spite of the high neutron energies at that experiment. The low influence of the Albedo on the dose reading H^m is due to the low calibration factor k_2, as given on page 41.

In section 5.4 on page 107, a comparison of the measured response values, as presented here, with the ones calculated from the Monte Carlo simulations in chapter 4 is done, along with the results of the other measurements conducted in the frame of this work.

5.2. Measurements with the AmBe source of the HMGU

The Americium-Beryllium (AmBe) source is a wildly used kind of neutron source, whose field is often utilized for the calibration of and measurement with both ambient and personal neutron dosemeters ([85]). The Helmholtz-Zentrum München is equipped with such an AmBe source, which has been used for the irradiation of REM counters ([86]), Bonner Spheres ([73, 87, 4], see also section 5.3) and of course the HMGU dosemeter prototypes ([25, 23, 21]) for several years now. The measured pulse height spectrum for a comparison with the Fast sensor on page 46 has been acquired with the AmBe source, as well as some of the factors given in table 3.3 for the calculation of the measured dose H^m from the number of counts in the different sensors. It plays a great role in the determination of the thresholds settings for the sensors, too, as described e.g. in section 3.3.2 and [25].

The energy spectrum of the AmBe source is well-known and can be found for example

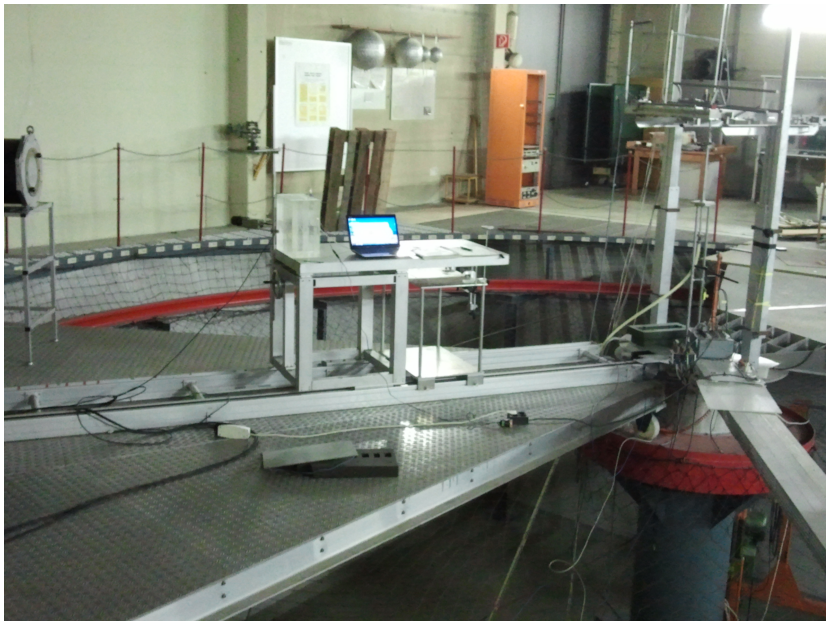

Figure 5.13.: Photograph of the neutron laboratory of the HMGU. The measurement position is on the table near the center of the hall.

in [72, 73, 25]. It is depicted in figure 4.2 on page 45. The corresponding fluence-to-dose conversion factor $h_p^{AmBe} = 411\,\mathrm{pSv}\cdot\mathrm{cm}^2$ can of course be calculated by applying equation (2.5), but due to its practical importance it is also tabulated in [85, 46, 47].

For an estimation of fluence and dose rates of the HMGU AmBe source depending on the date and distance to the source, the program MOSES has been implemented in Excel in the frame of [73]. This program was used in the present work as well to yield the desired quantities for the various measurements. When calculating uncertainties, the outputs of MOSES were considered to contain no systematical error.

5.2.1. Experimental setup

In this work, measurements in two different experimental setups containing the AmBe source were conducted. The first one stands for the measurement on a wheel, where ten dosemeter prototypes could be irradiated at the same time. Such kinds of measurements were already done in [25]. The second setup was the irradiation of dosemeter devices on a standard $30 \times 30 \times 15\,\mathrm{cm}^3$ plexiglass phantom.

All measurements with the AmBe source were carried out in the neutron laboratory of the HMGU. This building is dedicated to experiments with neutrons, since walls and huge amounts of materials are several meters away from the measurement position; for that, also the hall´s floor is excavated. The amount of unwanted scattered radiation can thus be reduced significantly. A photo of the HMGU neutron hall is shown in figure 5.13; for a schematic, see [73].

The so-called *"wheel"* used for the first measurement campaign with the AmBe source is

Figure 5.14.: Wheel for the simultaneous irradiation of ten dosemeters (from [25]). The AmBe source is placed on the holder in the middle; the black cubes are the polyethylene phantoms used in this setup.

depicted in 5.14. For the irradiation, ten prototypes are attached to the Aluminum holders at the rim, whereas the neutron source is positioned on the holder in the center of the wheel. Thus, the distance of all devices to the source is equally $d = 52.3\,\mathrm{cm} \pm 0.5\,\%$ (estimated uncertainty); in [25], the equivalence of the ten positions has also been tested. At a distance of several centimeters behind the dosemeters, polyethylene phantoms with dimensions $25 \times 10 \times 10\,\mathrm{cm}^3$ can be attached to the wheel, as shown in the figure.

For the measurement, ten dosemeters were randomly chosen and irradiated; the total measurement time was about four days, i.e. $t_m = 345540 \pm 200\,\mathrm{s}$. The uncertainty in this values is the time interval after which the acquired values were written to the internal memory of the dosemeters at this measurement. According to MOSES, that measurement time corresponds to a total fluence of $\Phi_n = 124.147 \cdot 10^6\,\mathrm{cm}^{-2}$, and a personal dose equivalent of $H_p\,(10) = 51.024\,\mathrm{mSv}$.

Since it must be doubted that the small polyethylene phantom applied for the measurement on the wheel can be used to acquire both personal dose and response of the Albedo sensor correctly, further measurements with the AmBe source were carried out using a $30 \times 30 \times 15\,\mathrm{cm}^3$ phantom made of plexiglass. One or two dosemeters were attached to the phantom surface, which was positioned at a distance $d = 105 \pm 3\,\mathrm{cm}$ from a the AmBe source. Altogether, five devices were examined in this way. Among the irradiations, the measurement duration t_m, and thus of course the total fluence and personal dose varied. Table 5.4 gives an overview of these parameters in the experiment presented here. Since dosemeters 102, 108 and 105, 106 were irradiated together, the corresponding values are the same of course. For the uncertainty

Prototype	102 and 108	105 and 106	113
t_m [s]	63060 ± 300	61620 ± 600	497580 ± 600
Φ_n [cm^{-2}]	$(5.617 \pm 0.350) \cdot 10^6$	$(5.489 \pm 0.369) \cdot 10^6$	$(44.33 \pm 2.59) \cdot 10^6$
$H_p(10)$ [mSv]	2.309 ± 0.144	2.256 ± 0.152	18.22 ± 1.06

Table 5.4.: Measurement times t_m, total fluence Φ_n and personal dose equivalent $H_p(10)$ for the measurements on a plexiglass phantom with the AmBe source. Devices 102 and 108 as well as 105 and 106 were irradiated together.

$\Delta\Phi_n$, both the statistical error as well as the systematical one given by

$$(\Delta\Phi_n)_{syst} = \Phi_n \cdot \left[\frac{\Delta t_m}{t_m} + 2 \cdot \frac{\Delta d}{d}\right] \tag{5.3}$$

were taken into account. The result was then translated to $\Delta H_p(10)$ using the fluence-to-dose conversion factor given above and equation (2.4).

In the context of the measurements with the plexiglass phantom, it was decided also to apply a second threshold for the Fast and Albedo sensor. In principle, this is possible just as with the Delta sensors. Thus, from the Fast sensor, two virtual sensors F1 and F2 were derived, with separate count values for each; the same was done for the Albedo. The counts in the original Fast and Albedo channel with a threshold setting $E_{thresh} = 1000\,\mathrm{keV}$ are not altered by this change, and therefor also the formula for dose assessment (3.11) had not to be augmented. The reason for the second sensor channel was merely to acquire more points for comparison with the simulation results, as presented in section 5.4 below. The comparator setting for the Fast F2 and Albedo A2 was channel 56; according to table 3.1 on page 28, this roughly corresponds to $E_{thresh} = 3500\,\mathrm{keV}$.

5.2.2. Results and discussion

For the analysis of the experimental results, the *response* R is calculated for each dosemeter, both for the setup on the wheel and on the phantom, since this is a quantity independent of measurement time and distance to the source. Mean values among the devices corresponding to one setup were calculated in the end; in order to ascribe the overall uncertainty, statistical and systematical uncertainties of the individual outcomes were treated separately.

With the irradiation of the ten dosemeters on the *wheel*, mainly the results given in [25] could be reproduced. Figure 5.15 summarizes the outcomes for the Fast and the Albedo sensor by showing the measured responses for each tested device. The response of the Albedo sensor is significantly lower than the one of the Fast, since the neutron energy spectrum of the AmBe source is a high-energetic one. Both sensors show a very uniform behavior, except the Fast one in devices 107 and 104. It has been already observed in [25] that for these two dosemeters, the response of the Fast sensor is lower; it is believed that an air bubble in the converter is the reason for that.[5]

[5] M. Wielunski (HMGU), private communication

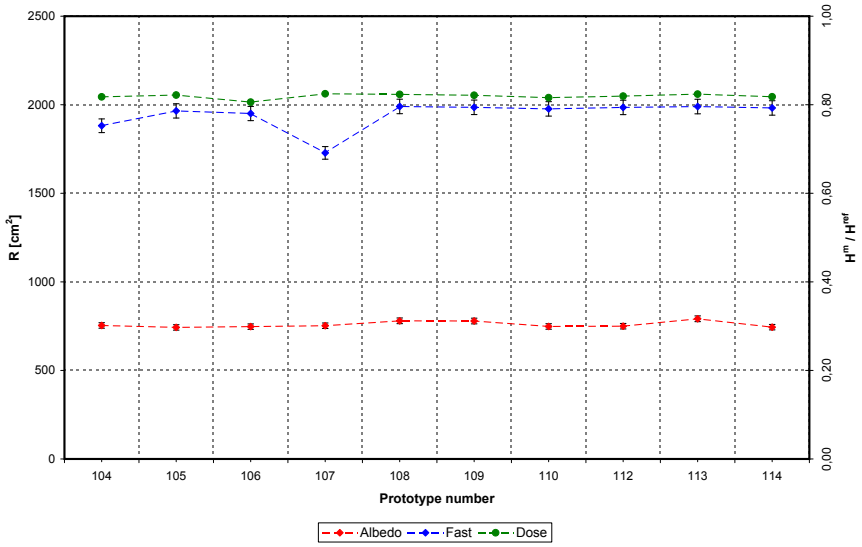

Figure 5.15.: Results acquired by the irradiation of ten dosemeters on the wheel. The red and blue points give the response of the Albedo and Fast sensors, respectively, and map to the left axis; the green points show the ratio of the measured dose H^m and the calculated dose H^{ref} and map to the right axis.

In the neutron field of the AmBe source, the counts of the Fast sensor make up around 94 % of the *dose reading* H^m, because of both the higher response and the higher calibration factor, as given on page 41. In the figure, the ratio of this dose reading and the personal dose equivalent calculated with MOSES for the present setup, i.e. $\frac{H^m}{H^{ref}}$, is shown by the green curve. For the devices 104 and 107, for which the number of counts from the Fast sensor is lower, no dips in the ratio are observed. This is because in [25] the factors for dose assessment have been altered for these two prototypes. Thus, the dose ratio shows a uniform behavior regardless of the actual response of the Fast sensor.

The values of $\frac{H^m}{H^{ref}}$, however, are for all dosemeter lower than one. In fact, the average value (with standard deviation among the devices) for this ratio is $\frac{H^m}{H^{ref}} = (81.9 \pm 0.6)$ %; the underestimation of the dose is thus around 18 %. This has already been reported in [25], too, where however a underestimation of 16 % is given. The slight difference comes from the fact that in the cited work, $H^\star(10)$ instead of $H_p(10)$ has wrongly been used as a reference. The reason for the underestimation is, just as with the measurement at the Helmholtz-Zentrum Berlin described in section 5.1, the deactivation of the Delta sensors. Because of the high-energetic neutrons present in the field of the AmBe source, the difference (3.10) is less than zero, so the Deltas do not contribute to the dose assessment (3.11). According to figure 6.1a on page 115, this leads to a dip in the sensitivity of the whole dosemeter at around $E_n \approx 1\,\mathrm{MeV}$, so the contribution of the lower part of the energy spectrum in figure 4.2 is undervalued.

R $\left[10^{-6}\,\mathrm{cm}^2\right]$	Setup on wheel	Setup on phantom
Fast F1	1943.5 ± 41.2	1996.7 ± 153.8
Fast F2	—	21.1 ± 2.3
Albedo A1	758.9 ± 16.4	1146.9 ± 89.7
Albedo A2	—	35.4 ± 3.9
Delta D1	68.9 ± 1.7	71.7 ± 6.7
Delta D2	32.8 ± 0.8	33.3 ± 3.4
Delta G1	74.5 ± 1.8	75.1 ± 7.0
Delta G2	35.6 ± 0.9	36.0 ± 3.7

Table 5.5.: Mean values and uncertainties of the responses R of the dosemeters´ sensors, measured both on the wheel and with a phantom

Although Delta D and Delta G do not account for the measured dose, their count values can be analyzed yielding a result for the response in the AmBe field. For all virtual sensors, the calculated response values are given in table 5.5 as mean values among the ten dosemeters. The outcomes for Fast and Albedo have been discussed above already. For the Delta sensors, of course the response in D1/G1 is higher than in D2/G2. One can see however that $2.2 \cdot (R_{D2} + R_{G2})$ is only *slightly* higher than $R_{D1} + R_{G2}$. Under certain circumstances, it can thus happen that even with the AmBe source, the Delta sensors are not deactivated, because (3.10) remains positive. This has been a frequent source of confusion in former experiments ([25]).

For the measurements with the plexiglass phantom, mainly the responses of the various sensors were of interest. As devices 104 and 107 were not used in this experiment any more, no huge differences in between the single prototypes can be expected. Thus, only the mean values are presented in table 5.5. The uncertainties given here are higher than for the irradiation on the wheel. This is only partly due to the lower number of devices tested; the main contribution comes from the (systematical) error Δd. The treatment of such uncertainties however is obligatory. Clearly, an analysis based on statistical uncertainties as in [25] is not sufficient.

Comparing the resulting responses for the various sensors in the table, no differences within the error ranges are observed, except for the Albedo sensor. This is in very good agreement with the basic result of the dosemeter simulations described in chapter 4, as it was discovered there that with the current threshold settings, a phantom has huge influence on the Albedo only. Since the effective differences among the two experimental setups presented here were the size, composition and alignment of the phantoms, a disagreement in the Albedo response was expected. Of course, the measured value for R_{A1} is higher in the second measurement campaign by around 51 %, since in that case the phantom dimensions were taller. According to the spatial distribution on page 62, which gives an impression on the amount of neutrons that are scattered in the phantom and still create counts in that sensor, it becomes clear that a $25 \times 10 \times 10\,\mathrm{cm}^3$ polyethylene phantom as used in the wheel measurement is not appropriate, especially if a gap of several centimeters is between the phantom surface and the dosemeter

holder. Also, because of this gap more scattered neutron radiation from the walls, the floor, etc. can enter the Albedo sensor through the hole in the back side of the Cadmium housing and thus make the experimental results more unreliable.

Nevertheless, even with the plexiglass phantom, the result concerning the measured *dose* is not very much different to the former measurements on the wheel. This is of course due to the fact that the deviation from the reference dose calculated with MOSES stems from the deactivation of the Delta sensors. Since the contribution of the Albedo is only a small percentage of the total dose reading, its increased response with the phantom does not change the ratio $\frac{H^m}{H^{ref}}$ significantly. The value here is $\frac{H^m}{H^{ref}} = (84.0 \pm 1.0)\ \%$, so the underestimation is about 16 %.

The responses for the newly configured sensors Fast F2 and Albedo A2, both with a threshold set to $E_{thresh} = 3500\,\mathrm{keV}$, are given in table 5.5, too. Of course, the actual values are rather small, in comparison to the corresponding F1 and A1 outcomes, due to the high threshold. With the high-energetic neutrons of the AmBe source, events with $E_{coll} > 3500\,\mathrm{keV}$ in the Fast sensor mainly come from the scattering of Carbon ions and direct $Si + n$ reactions in the detector. For the Albedo, the contribution of the conversion reaction (3.7), i.e. the tritium and alpha particles, is present as well, hence the higher response. Considering this, it is not surprising that the responses for A2, D2 and G2 are almost equal; all three sensors are equipped with the same converter and are employed with a similar threshold set to around 3500 keV. As in the simulations in chapter 4, the differences between the Albedo and the Deltas is restricted to the energy range $E_{coll} \lessapprox 2.7\,\mathrm{MeV}$, i.e. to the sensors A1, D1 and G1.

5.3. Measurement of neutrons from cosmic radiation

Neutrons, as mentioned in the introduction to this thesis already, play a very important role in secondary cosmic radiation. For the dose assessment in aircrafts, the contribution of neutrons is essential, as they make up around 50 % of the total dose at typical flight levels ([40, 6]). The HMGU has been investigating the neutron component of the cosmic radiation by both simulation and measurement for many years now. The measurements are conducted at two locations, that is on *Spitsbergen* and on the *Zugspitze mountain*; on both locations, a so-called *Bonner Sphere Spectrometer* (BSS) is constantly running, by which both fluence rate and energy spectrum of the neutrons can be determined. ([9, 10, 88]) The choice of these places is of course governed by the need for a relatively high count rate in every measurement. The Zugspitze, being the highest mountain in Germany, is a very well-suited location to investigate cosmic radiation, whose fluence in general decreases with decreasing altitude. Since Spitsbergen is situated near the North Pole, where the geomagnetic field strength is lower and thus the primary cosmic radiation is less effectively shielded, this location is appropriate also.

The energy spectrum of the cosmic radiation neutrons is a very wide one ranging from thermal neutrons to energies of several hundreds of MeV. Correct dose measurement in such a field is a complicated task, even with sophisticated devices. In this work, eight of the HMGU

dosemeters were positioned at the location of the BSS on the Zugspitze mountain, i.e. at the Umweltforschungsstation Schneefernerhaus (UFS) in an altitude of around 2660 m. There, the counts of the dosemeters´ sensors were acquired in a long-term experiment lasing nearly three months. In that irradiation, not only the response to neutron could be measured and compared to the simulation results, but also the influence of the other components of the cosmic radiation, i.e. protons, pions, muons, electrons etc., on the performance of the dosemeter could be estimated.

For the comparison with the simulation results, equation (A.7) is applied; that is, the energy spectrum of the neutrons present at the measurement location is folded with the appropriate response curve calculated in the Monte Carlo simulations in chapter 4 for each sensor. Multiplying the resulting value with the total neutron fluence yields a number of counts that can directly be compared to the corresponding number acquired in the measurement itself. This procedure however requires the results obtained with the BSS during the measurement time, i.e. fluence and energy spectrum of the neutrons, as an input.

5.3.1. Neutron spectroscopy with Bonner spheres

The principles of Bonner Sphere Spectrometers and on how such a device is utilized to acquire the fluence and energy distribution of a given neutron field is covered in detail in [37, 38, 5]. Here, only a brief description on the HMGU spectrometer operated at the UFS is given.

A Bonner Sphere Spectrometer, as the name suggests, is composed of several individual neutron-moderating spheres with gas-filled detectors in the centers. These gas detectors are in principle operated as proportional counters ([19, 45, 42, 73]). In order to measure neutrons, the gas filling is composed mainly of the helium isotope ^3He with a small amount of a *quenching gas*. If a neutron enters the gas-filled detector, it can interact with the ^3He according to

$$^3He + n \rightarrow ^3H + p \tag{5.4}$$

Just like in the reaction with Lithium, charged particles are produced here, namely tritium ^3H and a proton. Both further interact with the gas and create *electron-ion-pairs*, which eventually result in a signal in the detector electronics. Reaction (5.4) has a very high cross section of $\sigma_{n,p} \approx 5330\,\mathrm{b}$ at thermal kinetic energies ([44, 73, 5]); it is thus considered optimal for the detection of low-energetic neutrons ([89]). The Q-value here is $Q = 764\,\mathrm{keV}$ ([44], see section 2.2).

The role of the spheres surrounding the detectors in a BSS is to moderate down the incident neutrons to very low energies, so that reaction (5.4) can happen with a high probability. For that, these spheres consist of polyethylene, i.e. $(CH_2)_n$; the high amount of Hydrogen in this material provides a very effective moderation via scattering, as described on page 19. The basic idea for using such spheres with inbuilt detectors as a spectrometer is to apply several ones with varying diameter of the polyethylene. Since the response of a single sphere to a given neutron field is greatly influenced by the thickness of the moderating layer, the energy spectrum and

fluence of the field can be determined in an *unfolding* procedure taking into account the *count rates* yielded by the various detectors. The HMGU BSS consists of 13 spheres made of polyethylene as described, with diameters from 2.5 inch to 15 inch ([9, 4, 5]). One detector filled with the counting gas is operated without surrounding $(CH_2)_n$ sphere; naturally, this one is especially sensitive to thermal neutrons with its response mainly governed by the cross section of the ${}^3H\,(n,p)\,{}^3H$ reaction (5.4). Additionally, two detectors are equipped not only with 9 inch polyethylene moderators but with Lead shells of 0.5 inch and 1 inch thickness. As shown in the cross sections on page 35 already, *neutron multiplication reactions* like $(n, 2n)$, $(n, 3n)$ etc. can occur in Lead at high neutron energies. These reactions of course enhance the response of the corresponding spheres.

So altogether, 16 spheres make up the BSS operated at the Zugspitze. It is capable of measuring the neutron energy spectrum over an energy range from thermal energy up to 10 GeV. For the unfolding, as already mentioned, the count rates of the 16 spheres, denoted as ζ_i with $i = 1 \ldots 16$, are collected in the so-called *measurement vector* $\boldsymbol{\zeta}$. The individual count rates are thereby given by the incident fluence rate $\frac{\mathrm{d}^2\Phi_n}{\mathrm{d}t\mathrm{d}E_n}$ and the response function of the corresponding sphere $R_i\,(E_n)$:

$$\zeta_i = \int \mathrm{d}E_n \cdot R_i\,(E_n) \cdot \frac{\mathrm{d}^2\Phi_n}{\mathrm{d}t\mathrm{d}E_n} \tag{5.5}$$

In the unfolding procedure, relationship (5.5) is inverted; i.e. the spectral fluence rate $\frac{\mathrm{d}^2\Phi_n}{\mathrm{d}t\mathrm{d}E_n}$ is calculated from the measurement vector $\boldsymbol{\zeta}$ containing the count rates of the Bonner Spheres. This is a computationally demanding task, since the dependencies of the responses R_i on the neutron energy E_n are highly non-linear. These response functions have thus been calculated for various BSS spheres using Monte Carlo methods, e.g. in [90, 5, 87, 77, 40]. For the actual unfolding, a program called MSANDB is commonly applied, which utilizes an iterative procedure starting from an initially assumed spectrum ([91, 92]).

5.3.2. Experimental setup at the Schneefernerhaus

For the measurement of cosmic radiation with the HMGU dosemeters, eight prototypes were positioned in the experimental shed at the UFS, near the Zugspitze summit. The BSS being used for the determination of $\frac{\mathrm{d}^2\Phi_n}{\mathrm{d}t\mathrm{d}E_n}$ is located in that shed as well. Figure 5.16 shows photographs of both the measurement location[6] and the spectrometer. The devices were placed in between the Bonner Spheres, according to no specific pattern.

Due to the relatively low fluence rate of neutrons in comparison with the former experiments, the measurement time at the UFS had to be scheduled to several weeks. A change in the firmware of the prototypes was ordered for that, and additional chargers for the devices were constructed to enable a save run over a longer period. These chargers are based on an ordinary pluggable power supply and a LM-317 voltage regulator ([93]) ensuring that the

[6] from `http://www.schneefernerhaus.de/forschungsstation/bildergalerie.html`

(a) Experimental shed at the UFS in an altitude of approximately 2660 m

(b) Bonner Sphere Spectrometer operated at the UFS

Figure 5.16.: Experimental shed and BSS of the HMGU located at the Schneefernerhaus near the top of the Zugspitze mountain

	Φ_n $[10^3\,\mathrm{cm}^{-2}]$	$H_p\,(10)$ $[\mu\mathrm{Sv}]$	$H^\star\,(10)$ $[\mu\mathrm{Sv}]$
Period 1	61.73 ± 6.76	13.49 ± 1.42	13.36 ± 1.41
Period 2	556.30 ± 32.27	116.42 ± 6.60	115.17 ± 6.53

Table 5.6.: Fluence, personal and ambient dose equivalent in the two measurement periods at the UFS, calculated from the energy spectra shown in figure 5.17

charging current does not exceed the allowed value. Recharging was triggered every day by a clock timer.

The measurement with the eight devices was conducted in two time periods, which lasted nine days and around 74 days, respectively, that is $t_{m,1} = 777600\,\mathrm{s}$ (in April 2012) and $t_{m,2} = 6474600\,\mathrm{s}$ (from April to July 2012). The energy spectra, obtained with the BSS as described shortly in the previous section on page 98, corresponding to the two time periods are displayed in figure 5.17.[7] These spectra, like e.g. the ones presented on page 81, are given in *lethargy representation*. Each bin is thus scaled with the corresponding mean energy so that the area under the graph directly correlates to a fluence (or, in this case, fluence *rate*) value. In between the two periods, only slight differences in the energy distribution can be observed, which are ascribed to changes in the snow cover at the UFS.

The spectra shown in the figure are representative for measurements at the Zugspitze mountain, since the three peaks visible there are found in other measurements as well ([88, 87, 4, 5, 10]). The first one around $E_n \approx 25\,\mathrm{meV}$ shows the thermal neutrons that have already interacted with the material surrounding the BSS. The second peak between $E_n \approx 1\,\mathrm{MeV}$ and $E_n \approx 10\,\mathrm{MeV}$ is the *Evaporation Peak* that was also observed in the simulation of the HZB experiment (see figure 5.6). At around $E_n \approx 100\,\mathrm{MeV}$, the so-called *Cascade Peak* is observed ([88, 4, 5]). Similar distributions of neutron energies to the depicted ones can be calculated by analytical or Monte Carlo models, e.g. [5, 94, 95].

By integration of the spectra in figure 5.17, the mean fluence rates in the two measurement

[7] V. Mares (HMGU), private communication

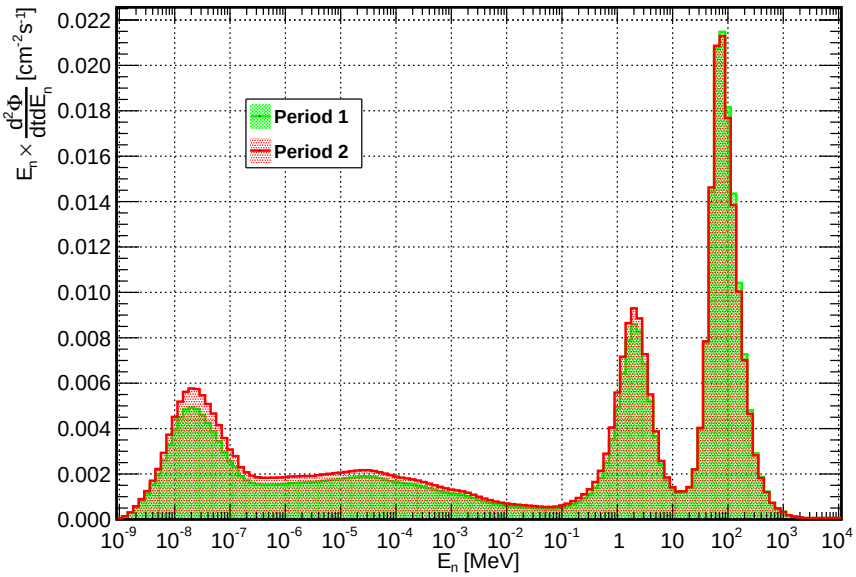

Figure 5.17.: Neutron energy spectra (in lethargy representation) for the two measurement periods; obtained with the Bonner Sphere Spectrometer at the UFS on Zugspitze mountain

periods can be obtained; in these, a systematical uncertainty of $^{\Delta\dot{\Phi}_n}/_{\dot{\Phi}_n} = 5\,\%$ was estimated. By multiplying the results for the two periods with the corresponding measurement times, the total neutron fluence was calculated. The numerical values are given in table 5.6. For the uncertainty in the measurement times, a conservative value of $\Delta t_m = 43200\,\mathrm{s}$ was taken for both measurement periods. Additionally, the dose rates were determined according to equation (2.5) by using the appropriate fluence-to-dose conversion coefficients h_p and $h^\star$ for personal and ambient dose equivalents, respectively. The personal dose equivalent $H_p\,(10)$, as described in section 2.3, is defined for a beam incident on a slab phantom actually; for cosmic radiation, it can however be assumed that the high energetic part, i.e. neutrons except thermal ones, are incident mainly from above, that is from the sky. Thus, the calculation of $\dot{H}_p\,(10)$ from the given fluence is a good approximation. The ambient dose rate $\dot{H}^\star\,(10)$ was however also calculated. In the table, these values in the two time periods, multiplied with the corresponding measurement times, are also shown. One can see that there is only a slight difference between personal and ambient dose equivalent. Since the discussion below is done in terms of response and fluence, the dose equivalents serve as supplementary information only. $H_p\,(10)$ cannot be considered as a reference quantity in that experiment anyway, since for the measurements, no phantom was used. For a comparison of calculated and measured response, or a discussion of expected and registered counts, the simulation results obtained without phantom therefore have to be employed.

$R\ \left[10^{-6}\,\mathrm{cm}^2\right]$	Period 1	Period 2
Fast	1538.9 ± 233.7	1201.5 ± 96.5
Albedo	1646.3 ± 248	1425.0 ± 112.9
Delta D1	431.3 ± 79.4	356.8 ± 32.7
Delta D2	303.7 ± 59.9	253.0 ± 24.4
Delta G1	435.4 ± 80.0	350.5 ± 32.2
Delta G2	309.8 ± 60.8	250.1 ± 24.2

Table 5.7.: Mean values and uncertainty of the response of the sensors in the two measurement periods.

5.3.3. Results and discussion

For the analysis of the experiment at the UFS, the two measurement periods are treated separately. The values obtained by the various dosemeters are taken into account in terms of a mean value with appropriate uncertainty. The latter is calculated from the statistical uncertainty in the count values of all eight devices and the systematical errors Δt_m and $\Delta\dot{\Phi}_n$. For the calculation of the response, the overall uncertainty is thus assigned according to

$$\Delta R = \frac{\sqrt{\sum_{k=1}^{8}\left(R^{(k)}\right)^2}}{8} + R \cdot \left[\frac{\Delta t_m}{t_m} + \frac{\Delta\dot{\Phi}_n}{\dot{\Phi}_n}\right] \tag{5.6}$$

The measured response values are given in table 5.7. As usual, the response gives the number of registered counts per unit neutron fluence, i.e. the ratio

$$R = \frac{N_c}{\Phi_n} \tag{5.7}$$

With the simulation results in chapter 4, the theoretical response R^{sim} for each sensor can be determined. Rearranging definition (5.7) - which is of course equivalent to the one given on page 146 - the number of counts N_c^{sim} and N_c^{meas} can be determined for each sensor, using the simulated and measured responses, respectively, and the total fluence yielded by integrating the neutron energy spectra in figure 5.17. In table 5.8, the simulated number of counts N_c^{sim} is compared to the mean value of the measured counts N_c^{meas} over the two periods. A huge discrepancy can be observed for all sensors of the dosemeter. On average, the ratio between simulated and measured counts is $\frac{N_c^{sim}}{N_c^{meas}} \approx 58\,\%$.

This disagreement can by no means be explained with uncertainties in the measurement process, nor with inaccurate simulation. Instead, it must be ascribed to the interaction of other particles of the cosmic radiation with the dosemeters´ sensors. In [5], the energy spectra of protons, neutrons, electrons, pions, muons and photons, as well as the fluence in various atmospheric depths has been calculated. As a first rough estimation, the contribution of *muons* and *protons* to the counts is roughly calculated, since these two types of particles, after neutrons, make up most of the dose rate at such altitudes ([5, 6]).

	Period 1		Period 2	
Counts	N_c^{meas}	N_c^{sim}	N_c^{meas}	N_c^{sim}
Fast	95	55	668	461
Albedo	102	61	793	526
Delta D1	27	14	199	116
Delta D2	19	10	141	84
Delta G1	27	15	195	123
Delta G2	19	10	139	82

Table 5.8.: Mean values of the counts registered in the two measurement periods in each sensor and number of counts calculated from simulations for the same periods and sensors.

In order to achieve this, the simulations without phantom geometry as described in chapter 4 and supplement A.2 were augmented for incident particles other than neutrons. The analysis ROOT scripts from supplement A.3 were applied in order to yield pulse height spectra for the new simulations and to calculate the response from them. By use of equation (5.7), with the calculated responses to protons and muons as well as the appropriate fluence instead of Φ_n, the number of counts originating from these components of the cosmic radiation could be estimated.

For the muon component, a energy distribution similar to a logarithmic normal distribution around $E_\mu \approx 1\,\mathrm{GeV}$ is given in [5], with a range of $E_\mu \approx 0.01 \ldots 100\,\mathrm{GeV}$. The fluence rate at the Zugspitze mountain, which corresponds to a atmospheric depth of roughly $750\,\mathrm{g/cm^2}$, is given as $\dot{\Phi}_\mu \approx 5 \cdot 10^{-2}\,\mathrm{cm^{-2}s^{-1}}$. The muon radiation field is comprised of μ^+ and μ^- in about equal shares. For the simulations, only the positive muons were used as incident particles. Five muon energies from $E_\mu = 0.01\,\mathrm{GeV}$ to $E_\mu = 100\,\mathrm{GeV}$ were simulated, with an incident number of particles of around $3.6 \cdot 10^6$ (i.e. a fluence of $\Phi_{\mu^+} = 1 \cdot 10^5\,\mathrm{cm^{-2}}$. The corresponding pulse height spectra for the Albedo and Fast sensors are shown in figure 5.18. As expected, the number of signals drops steeply towards higher collected energies E_{coll}. For all histograms, no significant number of signals above the threshold values $E_{thresh} = 1000\,\mathrm{keV}$ (see table on page 28) can be observed, except for the incident muon energy of $E_\mu = 0.01\,\mathrm{GeV} = 10\,\mathrm{MeV}$. This is due to the fact that for a very small kinetic energy, the range of the muons in the sensor materials is lower, so that a higher share of the energy can in principle be deposited.

All in all however, it must be noted that muons cannot be responsible for a substantial amount of the additional counts observed in the measurement at the UFS. The main reason it that only low energetic muons create signals above the threshold, which then result in counts. The fluence at $E_\mu \approx 10\,\mathrm{MeV}$ is only a very small fraction of the one at higher energies, though. The situation is even worse at the Zugspitze altitude than at an atmospheric depth of $250\,\mathrm{g/cm^2}$ for which the spectra in [5] are given; since muons reach lower altitudes only because of time dilatation due to their high velocity, it is suspected that the energy spectrum is shifted to higher energies with decreasing fluence. Even if this effect was neglected, muon contribution could only explain additional counts in the Albedo and Fast sensors; for the Deltas, the first

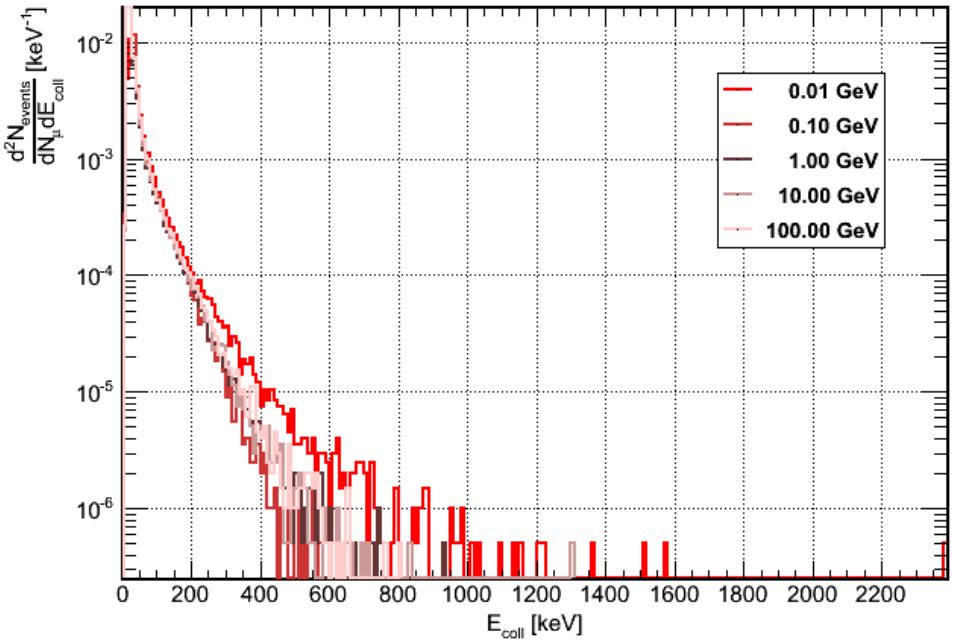

(a) Albedo sensor

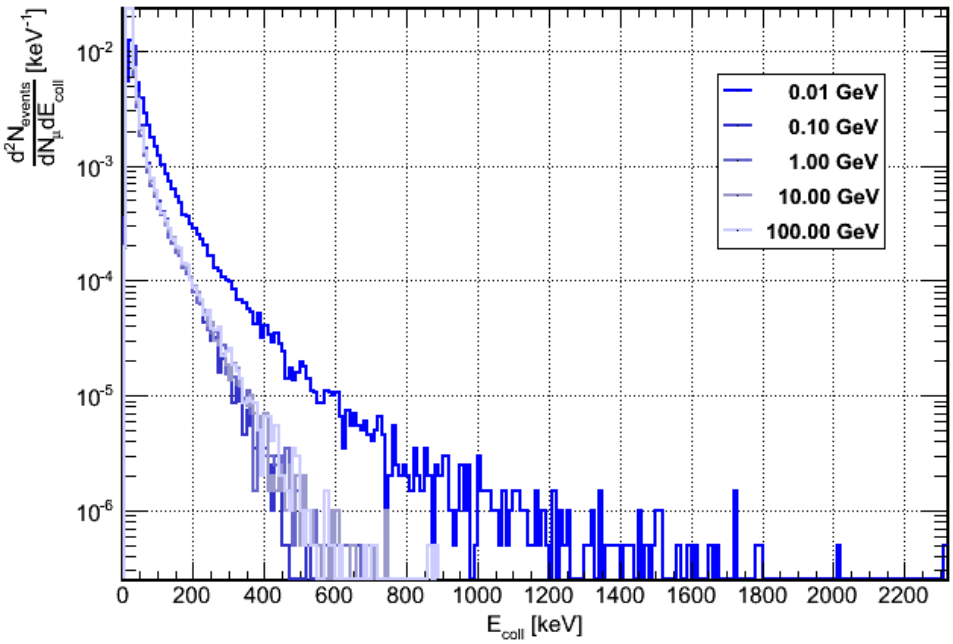

(b) Fast sensor

Figure 5.18.: Simulated pulse height spectra for the Albedo and Fast sensor, created by around $3.6 \cdot 10^6$ incident μ^+ particles at each of the five given energies $E_\mu = 0.01 \ldots 100\,\mathrm{GeV}$.

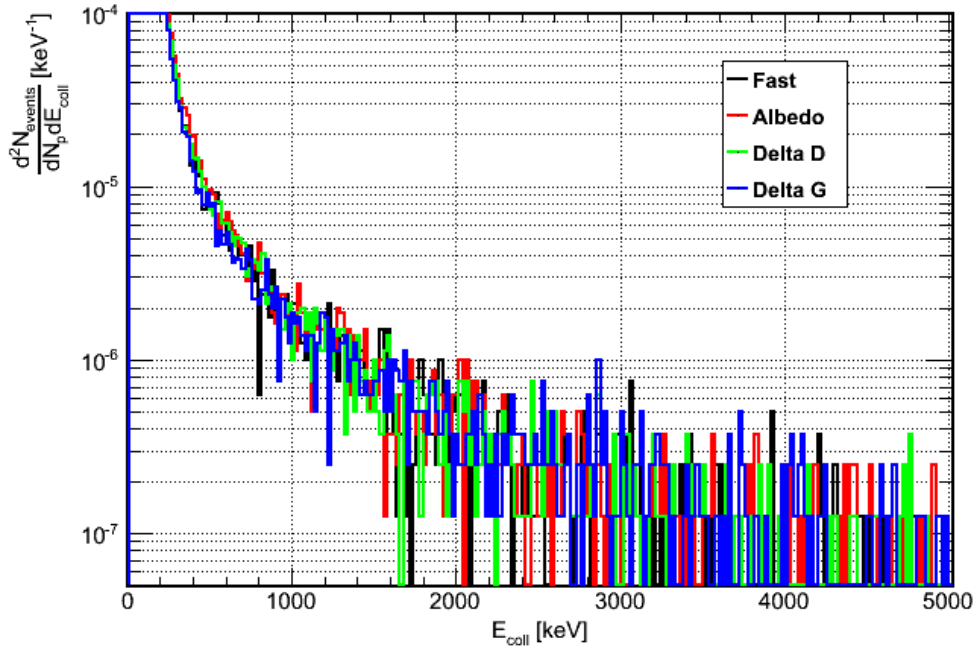

Figure 5.19.: Simulated pulse height spectra for all sensors of the HMGU dosemeter, created by around $7.2 \cdot 10^6$ incident *protons* with a specific energy spectrum.

threshold is at around $E_{thresh} = 2800\,\text{keV}$ only, so that the response even to 10 MeV muons would be nearly zero.

For the estimation of the number of counts created by *protons*, also fluence rate and spectrum according to [5] were taken into account. The energy distribution again resembles a logarithmic normal distribution. For the mean, a energy of $E_p = 500\,\text{MeV}$ is estimated. Unlike with the simulation of muons, it was not tried to reproduce the proton distribution with a number of energy points only; instead, the *PrimaryGenerator* class of the GEANT4 simulations (see figure A.1 and description on page 138) was altered in order to not only produce protons instead of neutrons, but also apply an uncertainty in energy on a logarithmic scale. For the width of the distribution, a value of 12.3 % was taken then, so that the spectrum depicted in [5] was roughly resembled. The simulation was run with about $7.2 \cdot 10^6$ incident particles, i.e. a proton fluence of $\Phi_p = 2 \cdot 10^5\,\text{cm}^{-2}$. In figure 5.19, the resulting pulse height spectra for all four sensors are displayed, which obviously do not differ substantially among each other. Although a very steep drop in number can be observed with increasing energy collection here as well, considerable more events with signals higher than the corresponding thresholds are shown than with the simulation of muons. This holds even for Delta D2 and G2, for which $E_{thresh} = 3500\,\text{keV}$.

From the simulated pulse height spectra, the *response* to protons can be calculated for each sensor, following the procedures usually applied in the case of incident neutrons (see section A.3). The resulting values, $R^{(p)}$, are then multiplied with the proton fluence to yield a number

	$R^{(p)}$ $\left[10^{-6}\,\mathrm{cm}^2\right]$	Period 1		Period 2	
		$N_c^{(p)}$	$\frac{N_c^{(p)}}{N_c^{meas}}$	$N_c^{(p)}$	$\frac{N_c^{(p)}}{N_c^{meas}}$
Fast	3170	12	13.0 %	103	15.4 %
Albedo	3285	13	12.6 %	106	13.4 %
Delta D1	765	3	11.2 %	25	12.5 %
Delta D2	495	2	10.3 %	16	11.4 %
Delta G1	850	3	12. 6%	28	14.1 %
Delta G2	520	2	10.6 %	17	12.1 %

Table 5.9.: Simulated response to protons, number of proton counts as well as fraction of proton counts in total number of measured counts, for each sensor

of counts. This fluence is calculated from the measurement time and the proton fluence rate $\dot{\Phi}_p \approx 5 \cdot 10^{-3}\,\mathrm{cm}^{-2}\mathrm{s}^{-1}$, which is given in [5] for the Zugspitze altitude. The resulting number of proton counts, $N_c^{(p)}$, for each of the sensors in each measurement period, are outlined in table 5.9. Although the fluence of protons is only around 6 % of the neutron fluence, the number of counts is considerable due to the high response to protons. On average, protons make up about $\frac{N_c^{(p)}}{N_c^{meas}} \approx 12.3\,\%$ of the measured counts. This value however may exceed 20 % considering that the proton fluence rate given above is only very roughly known. Moreover, the protons were incident on the sensors directly from above in the simulations, i.e. at an angle of 0°. In reality, the angle of incidence might be higher for a huge amount of the proton fluence, so that the average path length in the detectors is longer; this leads to a higher average deposition of energy in the active zone, so that the response is further enhanced.

Considering all this, it becomes evident that the unexpectedly high count rate of all sensors in the experiment at the UFS must be attributed to a contamination of the neutron field present there with all the other particles of the secondary cosmic radiation. In this work, only a rough estimation of the influence of protons on the number of counts is given; however, the principle is shown how the other components can be treated as well. For a thorough discussion, the response of the dosemeter over a wider energy range, to protons as well as to muons, pions, electrons, photons etc. would have to be calculated with the Monte Carlo simulations described in supplement A. Moreover, accurate energy spectra of the particles in question must be obtained, which can be either created with GEANT4 simulations according to [5] or by means of analytical methods ([94, 95]). With the spectra and the corresponding response of the devices, the exact number of additional counts can in principle be determined.

Measurements like this are of great interest, since the neutron energy spectrum at the Zugspitze is similar to the one created during the operation of heavy ion accelerators,[8] e.g. at the GSI HELMHOLTZZENTRUM FÜR SCHWERIONENFORSCHUNG ([96]). Since such accelerators are used in heavy ion radiotherapy as well, for example at the University Hospital in Heidelberg,[9] they are clearly within the range of applications intended for the HMGU neutron

[8] W. Rühm (HMGU), private communication
[9] http://www.klinikum.uni-heidelberg.de/Heidelberger-Ionenstrahl-Therapie-HIT.106580.0.html

dosemeter. In the long term, methods have to be developed therefore to effectively discriminate between the counts created by neutrons and by other particles. Any such means can however be tested at the UFS on Zugspitze mountain, since there the energy distribution and fluence of the cosmic radiation is very precisely known.

5.4. Comparison of measurements and simulations

The three experiments conducted in the present work, that is the measurement in pulsed fields at the HZB, the tests with an AmBe source and the investigation of secondary cosmic radiation effects, which have been described in the previous sections, have so far been analyzed for several quantities of interest already. Here, mainly the measured *response* in the various fields is taken into account, for a comparison with the simulation results presented in chapter 4. This serves as a verification of the simulation applications and is the basis for the credibility of calculated results in energy ranges where no measurements have been possible so far. Furthermore, the optimization of the dosemeter´s response outlined on page 113 is only feasible if the data this procedure relies on is thoroughly validated.

In order to yield a good agreement, special care is taken for the threshold setting of the six sensors of the dosemeter. For a further check of the outcome of the GEANT4 applications also for mono-energetic neutrons, preliminary results acquired at the PHYSIKALISCH-TECHNISCHE BUNDESANSTALT (PTB), which will be part of a forthcoming Master´s thesis, are presented in supplement B.

5.4.1. Realistic threshold settings

The dependence of the response $\eta \propto R$ on the neutron energy E_n, which has been shown in figures 4.19 and 4.21, has so far been calculated with the threshold settings outlined on page 28. In [25], these settings are considered optimal, and the energy value the comparators are adjusted to are estimated to fit quite well to the desired ones. This must be questioned in the present work, however.

As described above, the threshold in the collected energy, E_{thresh}, is set by using a *comparator* with a certain reference voltage U_{thresh}; that voltage is compared to the signal height output after the post-amplifier. It is thereby assumed that the signal processing chain consisting of pre-amplifier, shaper and post-amplifier (see figure 3.2 on page 27) establishes a linear amplification of the voltage drop U_{Drop} in the detector capacitor caused by the collection of charges. The relationship between collected energy and U_{thresh} is determined by the edge in the pulse height spectrum corresponding to the maximal kinetic energy of tritium ions produced in the reaction ${}^6Li\,(n,\alpha)\,{}^3H$ with thermal neutrons, which is $E_t \approx E_{coll} \approx 2.7\,\mathrm{MeV}$ according to equation (3.9). The procedure of threshold setting is outlined in sections 3.1 and 3.3.2 as well as in [25].

For the comparison of the measurement results presented in this work to the simulations, response values for the various sensors are calculated from the simulated pulse height spectra

Sensor	Mean channel	Ratio to 2640 keV	Threshold E_{thresh}
Fast	15.77	0.36	950 keV
Albedo	16.15	0.37	970 keV
Delta D1	42.85	1.02	2700 keV
Delta G1	41.62	1.03	2700 keV

Table 5.10.: Realistic threshold settings for the various sensors, i.e. the average channel number, the ratio of that channel number to the one at $E_{coll} = 2640\,\text{keV}$ and the corresponding threshold values in terms of energy.

using slightly adjusted thresholds, which are given in table 5.10. One can see that these values are below the optimal ones given formerly by around $50 \ldots 100\,\text{keV}$. It is feasible to apply these settings for comparison, mainly because the accuracy of the threshold-to-channel relationship given in [25] must be doubted. This concern is justified for several reasons:

- The thermal neutrons used in order to obtain the edge in the pulse height spectrum indicating a collected energy of $E_{coll} \approx 2.7\,\text{MeV}$ were produced by moderation in polyethylene layers around the AmBe source presented on page 91. Since this source emits very high-energetic particles, it is not clear whether the thermalization ran effectively and thus if the observed edge was not blurred due to a superposition of effects caused by the interaction of fast neutrons with the converter or detector.

- At the measurements conducted in the vicinity of Castor containers at Kernkraftwerk Isar described in [25], the threshold settings of the Delta sensors had to be incremented for several devices; the optimal values given in table 3.1 therefore tend to be too low.

- The shaping time of the Delta sensors is with $60\,\mu\text{s}$ six times higher than the one of the Fast and Albedo sensors.[10] The resulting difference in the output signal height of the shapers is balanced by different levels of the post-amplifiers. The channel settings for the Delta comparators are however still different from the ones of Fast and Albedo. For the latter two, even though they are operated with the same shaping time, the channel settings are not equal as well.

- Even in [25], an uncertainty of one channel in the setting of the thresholds is admitted, which must be assumed higher because of the sources of error given in the previous points. Generally, the adjustment of thresholds to fit certain experimental requirements has been a frequent practice in [25]. The believed agreement of the energy values E_{thresh} with the comparator channels must thus be regarded rather flexible.

Especially due to the last point, it is considered save to assume a previous mis-estimation of the Lithium-edge by one channel only. As one channel roughly corresponds to 60 keV, it was for simplicity assumed that the mean channel found to be commensurate with $E_{thresh} \approx 2.7\,\text{MeV}$ corresponds to $E_{coll} = 2640\,\text{keV}$ instead. The mean channels set for the various sensors are in

[10] M. Wielunski (HMGU), private communication

a certain ratio $\frac{\text{Channel set}}{\text{Channel 2640 keV}}$ to the former, which is also given in the table on the preceding page. Realistic thresholds E_{thresh} can be calculated then according to

$$E_{thresh} = 2640\,\text{keV} \cdot \frac{\text{Channel set}}{\text{Channel 2640 keV}} \tag{5.8}$$

This yields the values shown in 5.10 for Fast, Albedo and Delta D1, which are further used in the analysis of the simulations for comparison with measured results. In order to be consistent with the principle to treat both Delta sensors equivalently, the threshold for Delta G1 is set to $E_{thresh} = 2700\,\text{keV}$ as well (The calculated value would be 20 keV higher.); the thresholds for Delta D2 and G2 were not augment, i.e. $E_{thresh} = 3500\,\text{keV}$ is assumed.

5.4.2. Comparison of measured and simulated responses

The experiments conducted in the frame of this work involved neutron energy *spectra* over a possibly wide energy range; for all measurements, these spectra as well as the integrated neutron fluences or fluence rates are known. Thus, for each experiment and sensor, by applying equation (A.7) with the corresponding spectrum $\frac{\mathrm{d}\Phi_n}{\mathrm{d}E_n}$ and the simulated response function $R(E_n)$, the mean response $\bar{R}$ can be calculated:

$$\bar{R} = \frac{\int \mathrm{d}E_n \cdot R(E_n) \frac{\mathrm{d}\Phi_n}{\mathrm{d}E_n}}{\Phi_n} \tag{5.9}$$

The obtained result can be used to be compared with the response yielded by the measurement itself, which is equivalent to comparing count numbers, according to equation (A.8). The appropriate response values have been outlined in the corresponding sections for each experimental condition, i.e. with the AmBe source, at the HZB and at the UFS, and each sensor. For the calculation of the *simulated* response, above formula is applied on the response functions shown in figures 4.19 and 4.21.

In case of the AmBe source, of course the response curves simulated with phantom geometry are taken into account. As an experimental comparison, only the measurements conducted with the $30 \times 30 \times 15\,\text{cm}^3$ plexiglass phantoms (see section 5.2.1) were considered, since, as described earlier, the setup on the ´wheel´ with the smaller polyethylene phantoms is not sufficient for an accurate estimation of the Albedo response. In the measurements on the plexiglass phantoms, the thresholds for the virtual Fast F2 and Albedo A2 sensors were set to $E_{thresh} = 3500\,\text{keV}$. Since with given pulse height spectra by means of simulations it was simple to estimate the corresponding responses theoretically as well, these sensors are also used for comparison here.

A specialty of the AmBe source is that its energy spectrum, which is shown on page 45, was applied as an input to dosemeter simulations *directly*; that is, for each bin a suitable number of neutrons with the corresponding kinetic energy was simulated, and the summed up pulse height spectra for all sensors were acquired. The responses calculated from them differs slightly from values calculated according to (A.7), since the $R(E_n)$ curves on page 72 rely on a linear

interpolation of relatively few data-points in the range of the AmBe energy spectrum. All in all however, a huge discrepancy of simulation and measurement is not expected for either method of calculating $\bar{R}$, since that energy interval is well covered by the PTB measurements presented in supplement B, for which a good agreement is found.

The HZB measurements in pulsed fields were described and discussed in section 5.1; there, problems with two dosemeter positions of the plexiglass phantom were reported. As indicated, the mean responses given in the table on page 91 were calculated from the remaining two positions, with the measurements in all beam settings excluding the ones with the highest and lowest fluence rates. The simulated results were obtained by applying the "Folded spectrum" method, i.e. by utilizing equation (A.7) with the neutron energy spectrum at the HZB (acquired with the Bertini model, figure 5.6) and the response functions obtained with phantom geometry.

For the measurement of cosmic radiation at the Zugspitze mountain, the two measurement periods are treated independently. For both, the calculated responses based on the plain count values and the neutron fluences are given in table 5.7 on page 102. For the calculation of the theoretical response, R^{sim}, again formula (A.7) was applied, with the energy spectra given in figure 5.17. In order to at least partly account for the fact that a huge portion of the counts measured at the Zugspitze were not caused by neutrons but protons and other particles of the secondary cosmic radiation, the raw count values were reduced by the amount estimated to stem from protons, as outlined in table 5.9. With the remaining numbers, again the responses were calculated according to (5.7).

Figure 5.20 shows the ratio of responses based on simulation to the responses obtained in the measurements, that is $\frac{R^{sim}}{R^{meas}}$, which is equal to comparing *counts* as stated above. For an ideal agreement between simulation and experiment, the ratio would be $\frac{R^{sim}}{R^{meas}} \approx 1$, of course. It can be seen that in general, the discrepancies are rather small. In most cases, the over- or underestimation of the measured response by the simulations lies within 20 %, at least if the uncertainties are considered. The latter, besides, were simply calculated from the individual uncertainties of R^{sim} and R^{meas} according to

$$\Delta\frac{R^{sim}}{R^{meas}} = \frac{R^{sim}}{R^{meas}} \cdot \left[\frac{\Delta R^{sim}}{R^{sim}} + \frac{\Delta R^{meas}}{R^{meas}}\right] \tag{5.10}$$

The ratio for the Zugspitze is in most cases less than $\frac{R^{sim}}{R^{meas}} = 0.8$, for the uncorrected data as well as the data corrected for protons. The reasons for that have been discussed in section 5.3.3; obviously, the impact of protons on the dosemeters´ count rates is higher than yielded by the rough estimation presented there. Moreover, the influence of other particles has to be taken into account, as well as the exact fluence and energy distribution of protons at the UFS. A need for further investigation is obvious in that case; for a evaluation of the simulation results presented in this work however, the experimental data acquired in the Zugspitze measurements are not suitable. This, in turn, means that the disagreement of the responses observed in the figure do not imply faults in the Monte Carlo calculations.

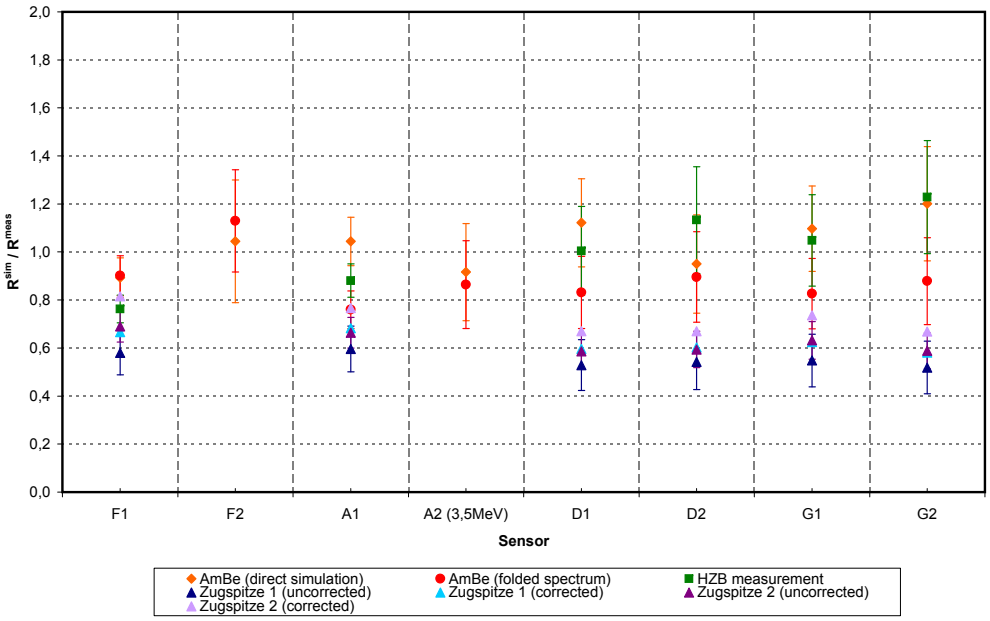

Figure 5.20.: Ratio of the response calculated from simulation results and from experimental results for each sensor and for three different measurement campaigns. For the AmBe measurements, two different methods of calculating R^{sim} were used; for the Zugspitze measurements, the "uncorrected" ratio refers to the response given by the plain count number, whereas for the "corrected" ratio that number was reduced to partly account for protons.

In contrast to the Zugspitze results, the ratios for the AmBe source and the HZB experiment are consistent with $\frac{R^{sim}}{R^{meas}} \approx 1$ generally. This especially holds for the Delta sensors. The outcomes with the AmBe energy spectrum obtained with the "folded spectrum method", i.e. equation (A.7), and the direct simulation are very similar as well. Even for the newly created sensors Fast F2 and Albedo A2, the ratio of the responses is around one.

For the Fast F1, i.e. the ordinary Fast sensor, the simulated response tends to be slightly lower than the measured one according to figure 5.20. Problems with the threshold setting as described in section 5.4.1 might account for the small discrepancy. Still, it cannot be expelled that undiscovered systematical errors are causing the deviation. In that case, mainly the agreement of the geometry implemented in the simulations with the real sensor in terms of material compositions, densities and dimensions must be questioned. A need for further investigation must be stated here as well; however, since, considering the uncertainties already included in the given ratios, the values for the AmBe and HZB experiments are consistent with a value of $\frac{R^{sim}}{R^{meas}} = 1 \pm 0.2$, the discrepancy is not considered prohibitive for some final conclusions in chapter 6 based on simulated data.

6. Conclusions, summary and perspectives

In this work, a profound understanding of the functional principles of the HMGU dosemeter prototypes has been gained. This was accomplished by both Monte Carlo simulations with the GEANT4 framework and experimental investigations in three different exposure conditions. The results derived from simulated data showed a very good agreement with the measurements.

6.1. Application of simulated data

The design principle of the HMGU dosemeter is intended to overcome the serious drawback many electronic personal neutron dosemeters must cope with, which is the under-response at neutron energies of around $E_n \approx 100\,\mathrm{keV} \ldots 1\,\mathrm{MeV}$ ([12, 11, 15, 14, 2, 50, 51] etc.). For that, the Delta D and G sensors were created (see section 3.3.2), which, due to their threshold setting, are insensitive to very low-energetic neutrons with $E_n \lessapprox 10\,\mathrm{keV}$, whereas at high energies, their deactivation according to equations (3.10) and (3.11) should prevent an overestimation of the dose. This concept works well if no neutrons with energies above $E_n \gtrapprox 5 \ldots 10\,\mathrm{MeV}$ are present. In this work however, by the measurements at the HZB and with the HMGU AmBe source, it was found that this switch-off constitutes a problem on its own, since the high-energetic neutrons in these experiments trigged the deactivation of the Deltas, which then still lead to a very low response of the devices around 1 MeV. Since in some situations a considerable portion of total fluence is concentrated in the evaporation peak at about that energy, a significant underestimation of the dose can occur. For the AmBe source, the ratio of measured and reference dose found in this work was $\frac{H^m}{H^{ref}} \approx 84\,\%$ (see section 5.2.2), and at the HZB measurement it was $\frac{H^m}{H^{ref}} \approx 63\,\%$ (section 5.1.3). Although values in the range $\frac{H^m}{H^{ref}} = 50 \ldots 200\,\%$ may be considered acceptable ([12, 13, 50]), this is clearly a point for improvement.

Since the response R of the various sensors of the dosemeter and its dependence on the neutron energy E_n has been simulated over a wide energy range in this work (and the simulation results showed a good agreement with experimental outcomes), the ratio in question, i.e. $\frac{H^m}{H^{ref}}\big|_{E_n}$, can be optimized with help of the simulated data. At first, the dependence of this value on E_n is clarified for the current dosemeter design; this will point out the energy regions where a need for improvement exists. On the basis of that, optimization methods can be applied.

6.1.1. Estimation of displayed dose

As stated earlier, the response R of a sensor is the number of counts of that sensor, N_c, divided by the neutron fluence, Φ_n. The dose assessment given by formula (3.11), is also based on the number of counts:

$$H^m = k_1 \cdot F + k_2 \cdot A + k_3 \cdot [(D_1 + G_1) - c \cdot (D_2 + G_2)]$$

This of course holds only if $(D_1 + G_1) - c \cdot (D_2 + G_2)$ is not less than zero, in which case the last term is canceled. Dividing the whole formula by the fluence Φ_n, the responses of the various sensors are introduced:

$$\begin{aligned} H^m &= k_1 \cdot \frac{F}{\Phi_n} + k_2 \cdot \frac{A}{\Phi_n} + k_3 \cdot \left[\left(\frac{D_1}{\Phi_n} + \frac{G_1}{\Phi_n} \right) - c \cdot \left(\frac{D_2}{\Phi_n} + \frac{G_2}{\Phi_n} \right) \right] \\ \frac{H^m}{\Phi_n} &= k_1 \cdot R_F + k_2 \cdot R_A + k_3 \cdot [(R_{D1} + R_{G1}) - c \cdot (R_{D2} + R_{G2})] \end{aligned} \tag{6.1}$$

As long as the dose assessment formula is *linear* in the count values of the sensors, this step is possible.

According to equation (2.4), the reference dose at a certain neutron energy is given by the neutron fluence multiplied with the corresponding fluence-to-dose conversion factor, i.e. $H^{ref} \equiv H_p(10) = h(E_n) \cdot \Phi_n$. Dividing (6.1) by the conversion factor, the desired ratio is obtained:

$$\left. \frac{H^m}{H^{ref}} \right|_{E_n} = k_1 \cdot \frac{R_F}{h} + k_2 \cdot \frac{R_A}{h} + k_3 \cdot \left[\left(\frac{R_{D1}}{h} + \frac{R_{G1}}{h} \right) - c \cdot \left(\frac{R_{D2}}{h} + \frac{R_{G2}}{h} \right) \right] \tag{6.2}$$

The quotient $\frac{R}{h}$ is equivalent to the quantity η' introduced in equation (A.6), i.e. the *response with respect to dose*. Its numerical values can be determined using the simulated response values R^{sim} for each sensor and the tabulated values for h ([47, 48, 49]). This was done for all energy points were simulations with phantom have been conducted. The obtained ratios were linearly interpolated on a linear energy scale. The values of R for a dosemeter sensor are usually influenced by the corresponding threshold setting E_{thresh}, as it was outlined earlier. This is taken into account in the calculations; that is, the ratio $\left. \frac{H^m}{H^{ref}} \right|_{E_n}$ was calculated with both the desired thresholds from table 3.1 and the actual ones given on page 108.

In figure 6.1a, the resulting functions for both threshold settings are given. The solid lines correspond to the realistic threshold settings also applied for the comparison with measurements. The light green line shows the situation in cases where the Delta sensors are activated. Then, obviously no underestimation of the incident dose in the region around $E_n \approx 1\,\mathrm{MeV}$ occurs. At higher energies, the deviation from unity is mostly within a factor of two. At neutron energies below $E_n \lessapprox 100\,\mathrm{keV}$ however, the dose is greatly over-estimated. In case of the realistic thresholds, the ratio $\left. \frac{H^m}{H^{ref}} \right|_{E_n}$ reaches a value of around $\left. \frac{H^m}{H^{ref}} \right|_{E_n \lessapprox 100\,\mathrm{keV}} \approx 80$. This is reduced by one order of magnitude if thresholds according to [25], as given in table 3.1, are

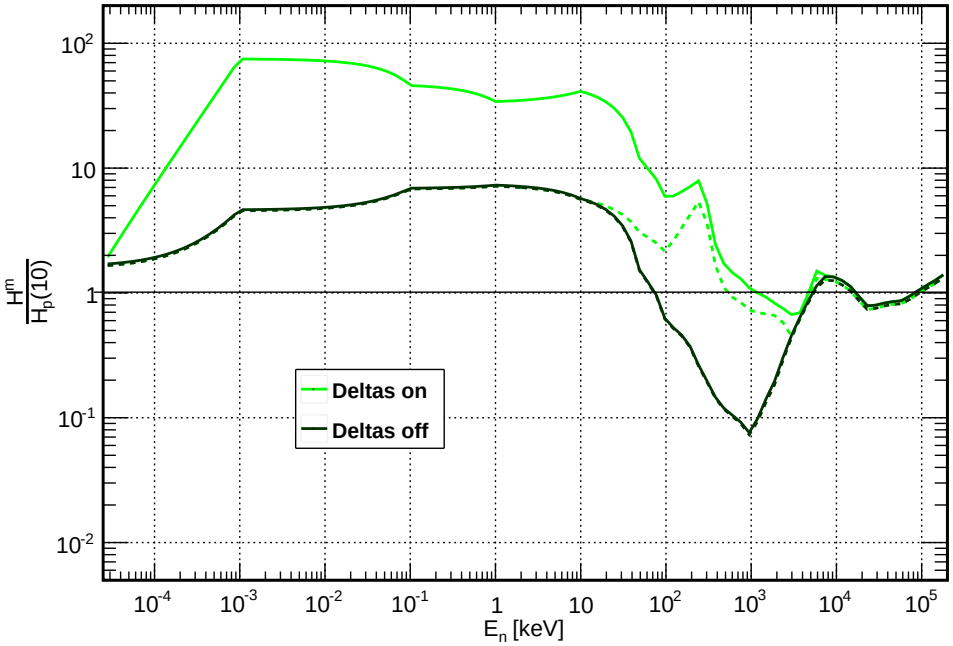

(a) $\frac{H^m}{H^{ref}}\Big|_{E_n}$ calculated for the whole dosemeter with the Delta D and G sensors switched on and off, respectively.

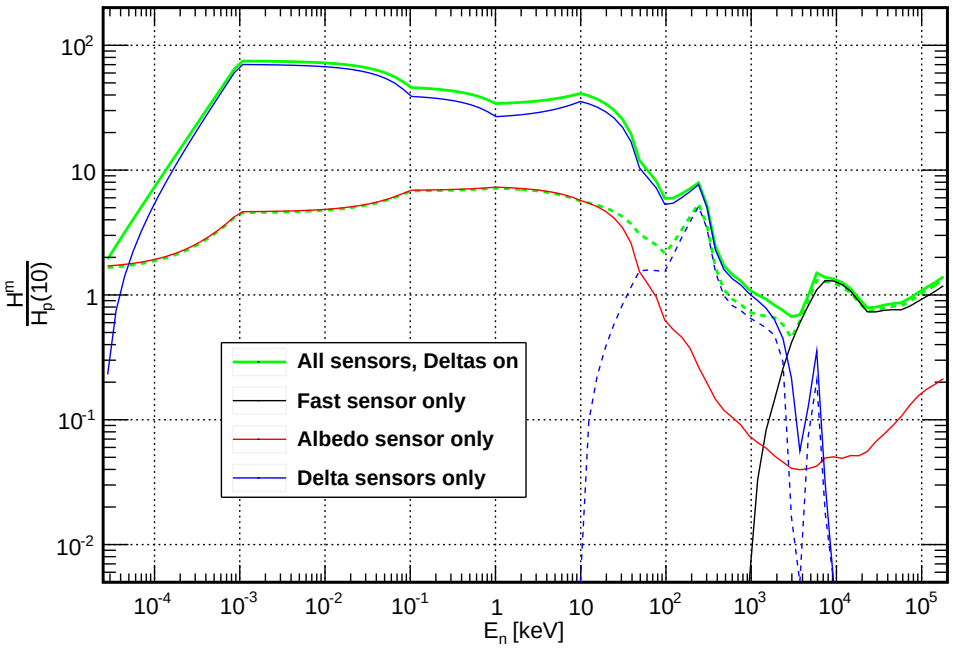

(b) $\frac{H^m}{H^{ref}}\Big|_{E_n}$ calculated for the whole dosemeter (with the Delta sensors activated) and for Fast, Albedo and the Deltas individually.

Figure 6.1.: Ratio of displayed and reference dose, both for the whole HMGU dosemeter and its individual sensors. The solid lines correspond to the realistic threshold settings given in table 5.10, whereas the dotted lines give the results for the threshold settings in table 3.1.

used for the calculations. A similar behavior of the dosemeter response has been reported for other devices as well ([12, 11, 15, 50]).

If the Delta sensors are deactivated (indicated by the dark green line), the considerable drop in the overall response, which was also observed in the measurements, is clearly visible. From $E_n \approx 100\,\mathrm{keV}$ to $E_n \approx 5\,\mathrm{MeV}$, the incident dose is underestimated, with a minimum of $\frac{H^m}{H^{ref}}\big|_{E_n \approx 1\,\mathrm{MeV}} \approx 0.1$ at around 1 MeV. Note that the adjustment of E_{thresh} obviously has a great influence on the Delta sensor group only; if the latter is switched-off, the behavior of $\frac{H^m}{H^{ref}}\big|_{E_n}$ is not affected any more.

Figure 6.1b shows the same ratio, but here also the influence of the individual sensors or sensor groups is displayed. The curve shown for all sensors is the one given in figure 6.1a as well, with the Delta sensors activated. The other curves give the dose ratio calculated for Fast, Albedo and the Delta sensors only, which is obtained by simply setting only the corresponding calibration factor k in (6.2) to its value. One can see that for the Fast and Albedo sensors, the dependence of the dose reading then just follows the response functions. The over-estimation at low energies is mainly due to the inappropriate threshold setting of the Delta sensors. With the actually set values according to section 5.4.1, the dose reading at low energies is mainly dominated by the Delta sensor counts. With the settings intended by [25], the influence of the Deltas is restricted to an energy of $E_n = 10 \ldots 10^4\,\mathrm{keV}$.

The analysis in this section clearly shows that by means of Monte Carlo simulation, not only the basic pulse height spectra and the response functions of the various sensors can be determined. The results obtained can also be combined further to provide a thorough understanding not only of the sensors´, but also the dosemeter´s behavior over a wide energy range. Of course, a comparison of experimental and theoretical results on the level of pulse height spectra and response functions, as done in this work, is essential first. Using verified data however, all features of the dosemeter can not only be reproduced, but also analyzed, understood and improved.

6.1.2. Improvement of response uniformity

In the previous section, the ratio $\frac{H^m}{H^{ref}}\big|_{E_n}$ for the current design of the dosemeter was given. From figure 6.1a, it becomes clear that two issues require improvement. The first one is the over-estimation of dose, with $\frac{H^m}{H^{ref}}\big|_{E_n = 1 \ldots 100\,\mathrm{keV}} \gg 1$ in the low-energy region in case of activated Delta sensors; the second and more severe one is the under-estimation around $E_n \approx 1\,\mathrm{MeV}$ if the Delta sensors are switched off. The drop in $\frac{H^m}{H^{ref}}\big|_{E_n < 1\,\mathrm{eV}}$ at thermal energies, which is also a drawback of the current design, cannot be corrected with the help of the so far simulated data alone. This drop directly comes from the Cadmium cross section (figure on page 35) and can be compensated by a bigger hole in the casing of the Albedo sensor (see section 3.3.3).

For the first two issues however, solutions can be found without changing the geometric design of the dosemeter at all. Adjustments simply have to be made on the threshold settings, which influence the response functions of the sensors, and on the calibration factors in the

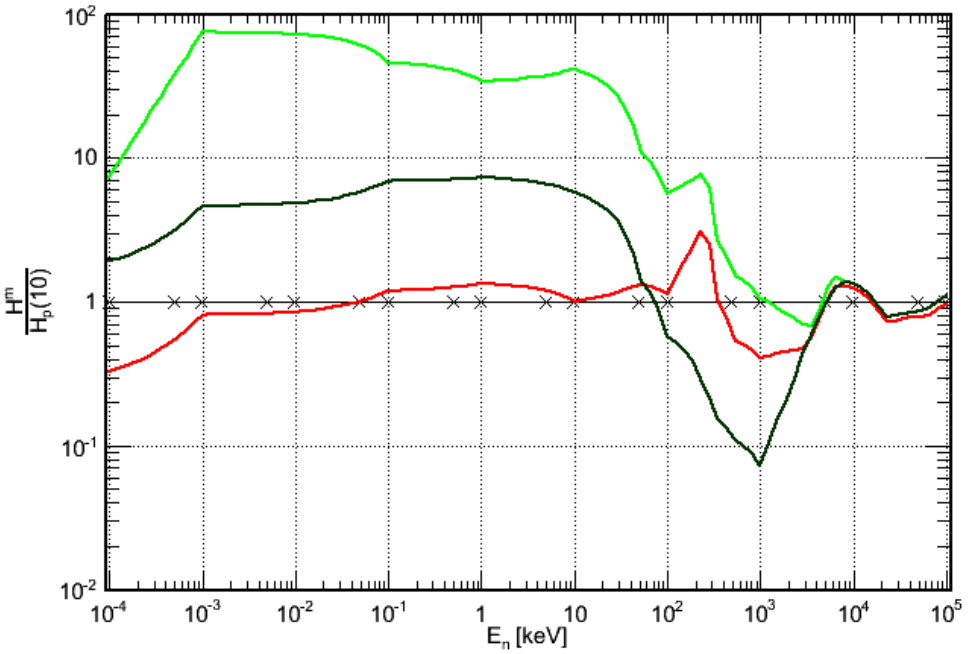

(a) $\frac{H^m}{H^{ref}}\Big|_{E_n}$ for the current design (Delta sensors on and off) and for optimized parameters in the current formula (3.11)

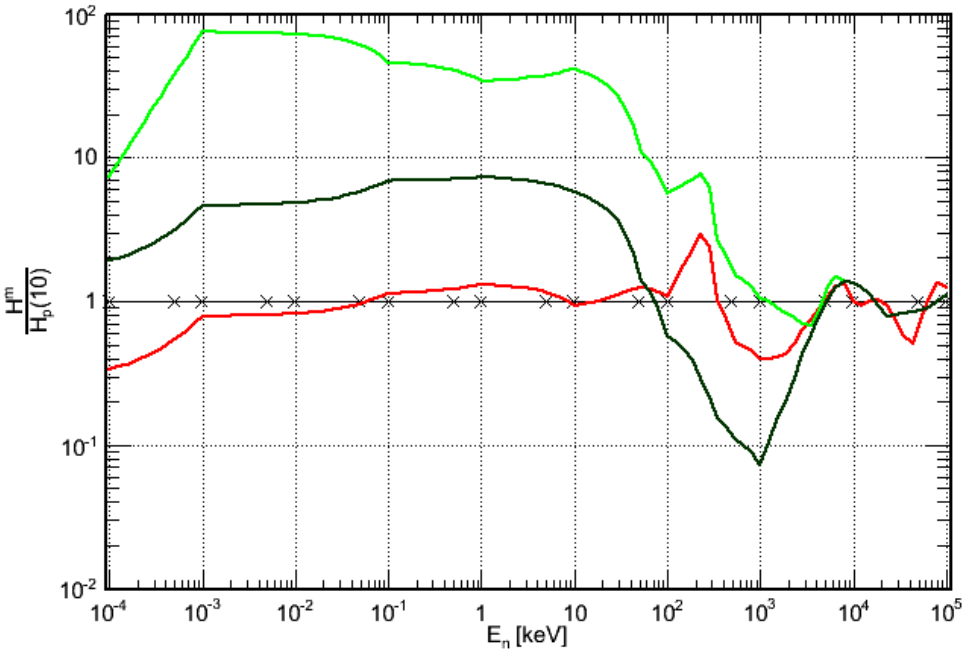

(b) $\frac{H^m}{H^{ref}}\Big|_{E_n}$ for the current design (Delta sensors on and off) and for optimized parameters in the proposed formula (6.3)

Figure 6.2.: Ratio of displayed and reference dose, both for the current design with Delta sensors activated (light green line) and switched off (dark green line) and for the optimized parameters (red line), all calculated with simulated data.

Parameter	Standard value	Realistic value	Fit with eq. (3.11)	Fit with eq. (6.3)
k_1	$0.1600\,\mu$Sv		$0.1548\,\mu$Sv	$0.2044\,\mu$Sv
k_2	$0.0256\,\mu$Sv		$0.0264\,\mu$Sv	$0.0195\,\mu$Sv
k_3	$9.0000\,\mu$Sv		$5.2890\,\mu$Sv	$5.0383\,\mu$Sv
k_4	—		—	$-6.2265\,\mu$Sv
c	2.2000		2.1233	—
$E_{thresh,F}$	1000 keV	950 keV	951 keV	1550 keV
$E_{thresh,A}$	1000 keV	970 keV	2461 keV	2396 keV
$E_{thresh,D1/G1}$	2800 keV	2700 keV	2780 keV	2780 keV
$E_{thresh,D2/G2}$	3500 keV	3500 keV	3500 keV	3458 keV

Table 6.1.: Overview of thresholds and calibration factors for the current design and fit outputs for improvement suggestions

dose assessment formula (3.11). The optimal values for the quantities in question can be determined with the simulated data.

The ratio $\frac{H^m}{H^{ref}}\big|_{E_n}$ in equation (6.2) should be around $\frac{H^m}{H^{ref}}\big|_{E_n} \approx 1$ over the whole energy range. Consequently, optimal values for thresholds and calibration factors can be found using *fitting procedures*, as implemented in ROOT ([78]). That is, the ratio $\frac{H^m}{H^{ref}}\big|_{E_n}$ is fitted to unity by optimizing the parameters controlling its energy dependence. The obtained results are preliminary and should be seen mainly as a starting point for further optimization; nevertheless, they clearly represent a considerable improvement over the current situation.

In figure 6.2a, the result of such an optimization procedure is displayed. For comparison, the energy dependences of $\frac{H^m}{H^{ref}}\big|_{E_n}$ for the cases with and without activated Delta sensors are also shown. The points to which the optimized ratio was tried to fit are indicated by markers. One can see that the optimized curve in the figure constitutes a significant improvement over the one with the current parameters. Compared to the case of activated Delta sensors, the over-estimation at low energies is corrected. At around $E_n \approx 250\,\text{keV}$, a peak in the ratio occurs, which can hardly be prevented because of the excess in the ${}^6Li\,(n,\alpha)\,{}^3H$ cross section (see figure 3.9). The underestimation at about 1 MeV is still present, but reduced to a minimal value of roughly $\frac{H^m}{H^{ref}}\big|_{E_n \approx 1\,\text{MeV}} \approx 0.4$. The optimization itself was done using the ROOT implementation of the Levenberg-Marquardt-Algorithm ([78, 97]). The fitted parameter values (plain rounded algorithm outputs without uncertainties) are given in table 6.1.

Using the common dose assessment according to equation (3.11), the switch-off of the Delta sensors is still a problem, even if the optimized parameters are used. The red line given in figure 6.2a shows only the ratio for the case of activated Delta sensors. A similar behavior can however be obtained if formula (3.11) is replaced by another one with no conditional elements, e.g.

$$H^m = k_1 \cdot F_1 + k_2 \cdot F_2 + k_3\,(D_1 + G_1) + k_4 \cdot (D_2 + G_2) \tag{6.3}$$

Using that formula, i.e. by replacing each count quantity with the appropriate η' and H^m with the ratio $\frac{H^m}{H^{ref}}\big|_{E_n}$ as above, the function shown in figure 6.2b (again with the old settings

for Deltas on and off as comparison) can be obtained. Here, the fitting was done using the *Simulated Annealing* method of the GSL ROOT-package ([98, 78, 99]). The general features are the same as for the curve obtained with the previous formula. Using (6.3) however, the same response function of the whole dosemeter is valid regardless of the spectrum, and spurious effects with the Delta deactivation are no longer problematic. The fitted values for the thresholds and calibration factors are again given in table 6.1.

Although the $\frac{H^m}{H^{ref}}\big|_{E_n}$ curve cannot be fitted to unity exactly, the use of simulated data as presented in this section allows a serious improvement in the accuracy of the HMGU dosemeter. The function (6.3) as well as the fitting procedures are mainly thought as suggestions; of course, there is need for more investigation in that field, and eventually the parameters derived from simulations must be implemented in the prototypes and tested in various neutron fields. With a dosemeter behavior as shown in figure 6.2b for example, one can expect that at least in non mono-energetic neutron fields the deviations of $\frac{H^m}{H^{ref}}\big|_{E_n}$ from unity will compensate.

6.2. Further activities

The points outlined in section 6.1.2 already show a main field of activity that must be covered by future research on the HMGU neutron dosemeter. That is, one should try to prevent the accuracy of the dose reading to depend on a deactivation of the Delta sensor group by choosing an appropriate dose assessment function. As shown here, the parameters of this function, i.e. the thresholds for each sensor as well as the calibration factors, can be optimized using the simulated data; subsequently, the obtained values must be implemented and the devices must be tested in neutron fields with various energy distributions.

In the present work, some additional points were identified where further investigation, both experimentally and by means of Monte Carlo simulation, is required:

- If data obtained by simulations is used extensively for an optimization of the HMGU dosemeter, the response of the Albedo sensor must be re-considered. Here, the influence of thermal scattering in the phantom must be calculated thoroughly, that is with more energy points and better statistics than could be done in the present work. In that case, it may seam feasible to not only apply massive parallelization of the GEANT4 application, but also use *variance reduction techniques* ([99, 75, 27]) when a phantom is included in the geometry. The spatial neutron distribution given e.g. on page 65 can be used as a starting point.

- The agreement of measurements and simulations can be further tested using more of the results that have been already acquired. An example is the PTB measurements (section B), where a final analysis is still to be given, and also the results for the irradiations under 60° must be included. For that, simulations with neutrons incident under that angle must be conducted.

- The dosemeter test in pulse fields described in section 5.1 revealed that for very high fluences, pile-ups in the Delta sensors might constitute a problem. This must be kept in mind, especially if a new dose assessment formula enhancing the Delta importance is applied. Further experimental work must be done to discover the limits of the various sensors regarding fluence rate and time structure of the neutron fields.

- In the experiment at the Zugspitze (section 5.3) a huge impact of particles other than neutrons on the sensor readings was discovered, especially of protons. In mixed fields, for example outside the shielding of medical accelerators, this effect may be an issue. Innovative means for the suppression of counts not created by neutrons must be developed for the determination of the pure neutron dose in such fields; another possibility is to investigate how far the dose created by the other particles can be accounted for in the dosemeter reading.

- The charge collection model, i.e. the dependence $\epsilon_q(z)$ of the charge collection efficiency (CCE) on depth, given on page 32 is so far only validated by the good agreement of the measured and simulated pulse height spectra of the Fast sensor, as shown e.g. in figure 4.3. A thorough justification of the CCE function, however, should rely on a measured dependence. For that, protons with various energies incident on the plain Silicon detectors can be utilized; the acquired relationship between pulse heights E_{coll} and proton energies E_p should follow a curve similar to the one given in figure 4.4. This, in turn, can then be used to deduce $\epsilon_q(z)$.

- In order to set the suggested threshold values from section 6.1.2, or other ones, more correctly, it may be necessary to decrease the energy interval one comparator channel corresponds to. This can be done by including another resistor in the sub-circuits with the comparator voltage divider.[1]

Many of the points given here, including the simulation of the dosemeter response under 60° and the comparison with PTB measurements, may be treated in a forthcoming Master´s thesis at the HMGU. For the experimental determination of the CCE, a measurement campaign at the Max-Plank-Institut für Plasmaphysik (IPP) in Garching is currently being prepared.

6.3. Resumé

In the frame of this thesis, investigation was done on the prototypes of the HMGU neutron dosemeters by means of both simulation and experiment. The dosemeters consist of four sensors with different characteristics, i.e. converter materials, dimensions and threshold settings. The counts of all sensors, that is the number of signals exceeding the corresponding threshold

[1] M. Wielunski (HMGU), private communication

value, are multiplied with specific factors and summed up to determine the dose reading of the device.

For the simulations, the Monte Carlo method was used; for that, several C++ applications were created utilizing the GEANT4 Monte Carlo framework, which was and is still being developed at CERN. Analysis of the simulation output was accomplished using the ROOT statistical package provided by CERN as well.

The first part of the simulations consisted of the determination of pulse height spectra of the four sensors at different energies of the incident neutrons. For that, the charge collection efficiency (CCE) of the Silicon detectors was accounted for by applying an innovative read-out scheme. In the program implementations, the detector was modeled as a stack of thin layers; during the analysis the energy deposition by each event and in each layer was weighted according to the assumed charge collection efficiency in the depth of that layer, in order to yield the total signal height. In the simulation of the Fast sensor, with an AmBe energy spectrum as an input, a good agreement with a measured pulse height spectrum was found when using an appropriate charge collection model. This model was then applied to the other sensors as well.

The acquired pulse height spectra for the Fast, Albedo and Delta sensors provided insight into the physical processes occurring in the converters and the ones leading to energy deposition in the detectors. For the Fast sensor, it was shown that both scattering on Hydrogen and Carbon leads to the creation of charged ions creating signals in the detector. For increasing energy of the incident neutrons, the contribution of Carbon becomes more important than that of Hydrogen. For the latter, it was shown that the energy collection by H ions, i.e. protons, is limited, depending on the CCE model. For the one used in the simulations, a *partial charge collection peak*, that is an accumulation of signals, formates at around a pulse height of 2.2 MeV.

For the Delta sensors, the influence of surrounding material was thoroughly studied as well. Here, it was shown that both scattering as well as the ${}^{6}Li\,(n,\alpha)\,{}^{3}H$ reaction in the converter play a role; the importance of the latter was found to increase with lower neutron energies. Additionally, it was shown that the presence of a phantom enhances that contribution, but has - with appropriate threshold settings - little influence of the number of counts.

When studying the Albedo sensor, special interest was placed on the influence of a phantom. It was shown that this is very important for the functionality of the Albedo, since neutrons are scattered in the phantom and may possess considerable path lengths in it. For low energies, it was shown that neutron absorption in the dosemeter materials plays a role. Moreover, the thermal scattering cross sections of GEANT4 were applied for the phantom at four energy points; a slight influence of that augmented physics was observed, but for this thesis, limited available computational power led to the decision to obtain further results without thermal scattering.

For all sensors, direct $Si+n$ reactions were identified to create signals. This contribution to the pulse height spectra becomes more visible at higher neutron energies. At several 10 MeV,

these are the most dominant reactions.

In the second part of the simulations, the response functions of the six (virtual) sensors were determined over a wide energy range from thermal to several hundred MeV neutrons, by simulating the pulse height spectra at distinct energy points and calculating the responses using the corresponding threshold values. Linear interpolation was done in between. The response dependencies on the neutron energy were discussed using the knowledge on the physical processes obtained in the previous simulations of the single sensors. The simulations were conducted both with and without phantom; as expected, only for the Albedo sensor a significant difference was observed.

In the experimental investigations, the dosemeter prototypes were tested in three different neutron fields.

At the first experiment at the Helmholtz-Zentrum Berlin (HZB), the behavior of the various sensors in pulsed fields was tested. Therefore, four dosemeters were irradiated in an accelerator-produced pulsed neutron field with constant burst frequency, but various fluence rates. In order to determine the fluence and the reference dose rate in the measurements, the basic experimental setup was also simulated using an augmented Geant4 application. Thus, the neutron spatial fluence and energy distributions were acquired. In the measurements themselves, a linear relationship between count rate and fluence rate was established for all sensors; only for the Deltas, a slight excess due to pile-ups at the highest fluence rate was observed.

A second irradiation was conducted with the AmBe source of the HMGU. In that experiment, ten devices on the measurement ´wheel´ as well as five devices on plexiglass phantoms were tested. A huge difference in the Albedo response was observed, showing that the smaller phantoms on the wheel are not appropriate for accurate measurements.

In both experiments, i.e. at the HZB and with the AmBe source, only little influence of the Albedo sensors on the dose readings was observed, due to the high-energetic neutrons present. The main contribution was from the Fast sensors. In both situations, the Delta sensors were switched off, so that the neutron fluence around 1 MeV was not measured correctly. Consequently, the reference dose was underestimated by about 40 % and about 20 %, respectively.

In the third experiment at the Zugspitze mountain, secondary cosmic radiation was measured with eight dosemeter prototypes. The neutron energy spectrum and fluence at the measurement location were provided by a Bonner Sphere Spectrometer. By comparison of the measured counts with expectations based on simulation results, it was shown that other components of cosmic radiation than neutrons have a considerable influence on the reading of the dosemeter. The number of counts created by protons was estimated with a dedicated Monte Carlo simulation to be more than around 12 % of the total counts.

The experimental results, i.e. the responses of the various sensors, were compared with the simulation outcomes using the neutron energy distributions and the acquired response functions. Thereby it was shown that the thresholds the comparators are set to may be not correct. Further comparison was done using preliminary results from a measurement at the

Physikalisch-Technische Bundesanstalt. With most energies and energy spectra, a good agreement of measured and simulated response of the sensors was observed. This can be considered a verification of the simulation programs and analysis procedures.

Using simulated data, the accuracy of the dose reading of the prototypes can be significantly improved. By fitting a new dose assessment formula to a unity ratio between measured and reference dose, better values for thresholds and calibration factors can be obtained, and the deactivation of the Delta sensors, along with the involved problems, can be prevented. As future activities, implementation and checking of the optimized formula, as well as some minor improvements for which a need was identified in the experiments, remain to be done.

Bibliography

[1] W.H. Chu, J.H. Lan, T.C. Chao, C.C. Lee, and C.J. Tung. Neutron spectrometry and dosimetry around 15 MV linac. *Radiation Measurements*, 46:1741–1744, 2011.

[2] H. Schuhmacher. Workplace monitoring of mixed neutron-photon radiation fields and its contribution to external dosimetry. *Radiation Protection Dosimetry*, 144:599–604, 2011.

[3] M. Silari, S. Agosteo, P. Beck, R. Bedogni, E. Cale, M. Caresana, C. Domingo, L. Donadille, N. Dubourg, A. Esposito, G. Fehrenbacher, F. Fernandez, M. Ferrarini, A. Fiechtner, A. Fuchs, M.J. Garcia, N. Golnik, F. Gutermuth, S. Khurana, Th. Klages, M. Latocha, V. Mares, S. Mayer, T. Radon, H. Reithmeier, S. Rollet, H. Roos, W. Rühm, S. Sandri, D. Schardt, G. Simmer, F. Trompier, C. Villa-Grasa, E. Weitzenegger, B. Wiegel, M. Wielunski, F. Wissmann, F. Spurny, A. Zechner, and M. Zielczynski. Intercomparison of radiation protection devices in a high-energy stray neutron field. Part III: Instrument response. *Radiation Measurements*, 44:673–691, 2009.

[4] C. Pioch. Messung und Analyse von Sekundärneutronen-Spektren der kosmischen Strahlung, 2008. Diploma Thesis, Technische Universität München.

[5] C. Pioch. *Measurement and Simulation of the Radiation Environment in the Lower Atmosphere for Dose Assessment.* PhD thesis, Technische Universität München, 2012.

[6] W. Rühm. External dosimetry for cosmic rays in aircrafts. In *Advanced WE-Heraeus Physics School "Ionising Radiation and Protection of Man"*, Bad Honnef, 2012.

[7] P. Beck, J.-F. Bottolier, G. Reitz, W. Rühm, and F. Wissmann. Cosmic radiation and aircrew exposure. *Radiation Protection Dosimetry*, 136:231, 2009.

[8] P. Goldhagen. Overview of aircraft radiation exposure and recent ER-2 measurements. *Health Physics*, 79(5):526–544, 2000.

[9] G. Leuthold, V. Mares, W. Rühm, E. Weitzenegger, and H.G. Paretzke. Long-term measurement of cosmic ray neutrons by means of a Bonner spectrometer at mountain altitutes - first results. *Radiation Protection Dosimetry*, 126:506–511, 2007.

[10] W. Rühm, V. Mares, C. Pioch, E. Weitzenegger, R. Vockenroth, and H.G. Paretzke. Measurement of secondary neutrons form cosmic radiation with a Bonner sphere spectrometer at 79° N. *Radiation and Environmental Biophysics*, 48:125–133, 2009.

[11] D.T. Bartlett, R.J. Tanner, and D.J. Thomas. Active neutron personal dosemeters - a review of current status. *Radiation Protection Dosimetry*, 86:107–122, 1999.

[12] M. Luszik-Bhadra. Electronic personal dosemeters: the solution to problems of individual monitoring in mixed neutron/photon fields? *Radiation Protection Dosimetry*, 110:747–752, 2004.

[13] M. Figel. Personendosimetrie - Körperdosisermittlung bei externer Bestrahlung. In *Grundkurs im Strahlenschutz für Ärzte und Medizinphysikexperten*. Helmholtz-Zentrum München, 2012.

[14] T. Bolognese-Milsztajn, M. Ginjaume, M. Luszik-Bhadra, F. Vanhavere, W. Wahl, and A. Weeks. Active personal dosemeters for individual monitoring and other new developments. *Radiation Protection Dosimetry*, 112:141–168, 2004.

[15] M. Wielunski, W. Wahl, N. El-Faramawy, W. Rühm, M. Luszik-Bhadra, and H. Roos. Intercomparison exercise with MeV neutrons using various electronic personal dosimeters. *Radiation Measurements*, 43:1063–1067, 2008.

[16] C.H. Westcott. A study of expected loss rates in the counting of particles from pulsed sources. In *Proceedings of the Royal Society of London*, volume 194 of *Series A*, pages 508–526, 1948.

[17] A. Klett and A. Leuschner. A pulsed neutron dose monitor. In *IEEE 2007 Nuclear Science Symposium & Medical Imaging Conference*, Honolulu, Hawaii, USA, 2007.

[18] M. Caresana, A. Denker, A. Esposito, M. Ferrarini, N. Golnik, E. Hohmann, A. Leuschner, M. Luszik-Bhadra, G. Manessi, S. Mayer, K. Ott, J. Röhrich, M. Silari, F. Trompier, M. Volnhals, and M. Wielunski. Intercomparison of radiation protection instrumentation in a pulsed neutron field. *Nuclear Instruments and Methods in Physics Research A*. to be published.

[19] G.F. Knoll. *Radiation Detection and Measurement*. John Wiley & Sons, 1979.

[20] R. Schütz, M. Wielunski, G. Fehrenbacher, J. P. Biersack, and W. Wahl. Calculation of pulse height distributions for neutron irradiated ^{6}LiF converter silicon detectors. *Radiation Protection Dosimetry*, 84:393–397, 1999.

[21] R. Schütz. *Development of Electronic Detection Systems for the Dosimetry in Neutron Fields*. PhD thesis, Technische Universität Bergakademie Freiberg, 2000.

[22] M. Wielunski, R. Schütz, E. Fantuzzi, A. Pagnamenta, W. Wahl, J. Palfalvi, P. Zombori, A. Andrasi, H. Stadtmann, and Ch. Schmitzer. Study of the sensitivity of neutron sensors consisting of a converter plus Si charged-particle detector. *Nuclear Instruments and Methods in Physics Research A*, 517:240–253, 2004.

[23] M. Wielunski, W. Rühm, and W. Wahl. Entwicklung von elektronischen Neutronen-Photonen Dosimetern. In *DPG Berlin 2008*, Berlin, 2008. Deutsche Physikalische Gesellschaft.

[24] M. Węgrzecki, M. Wielunski, J. Sarnecki, J. Bar, T. Budzyński, M. Cież, P. Grabiec, R. Grodecki, J. Kulawik, D. Lipiński, A. Panas, W. Rühm, W. Słysz, W. Wahl, I. Węgrzecka, K. Witek, and M. Zaborowski. Sensors for neutron dosimeters. In *10th Conference "Electron Technology"*, Wrocław, 2010.

[25] F. Berchtold. Weiterentwicklung und Kalibrierung eines Personendosimeters für Neutronen, 2011. Diploma Thesis, Technische Universität München.

[26] Geant4: A toolkit for the simulation of the passage of particles through matter. `http://geant4.web.cern.ch`.

[27] Geant4 Collaboration. *Geant4 User's Guide for Application Developers*, geant4.9.3 edition, 2009.

[28] T. Mayer-Kuckuk. *Kernphysik*. Teubner, 5th edition, 1992.

[29] K. Bethge. *Kernphysik*. Springer, 1996.

[30] G. Schatz, A. Weidinger, and M. Deicher. *Nukleare Festkörperphysik*. Vieweg+Teubner, 4th edition, 2010.

[31] J.J. Duderstadt and L.J. Hamilton. *Nuclear Reactor Analysis*. John Wiley & Sons, 1976.

[32] R. Schwanker. Entstehung von Strahlung und Eigenschaften von Radionukliden. In *Grundkurs im Strahlenschutz für Ärzte und Medizinphysikexperten*. Helmholtz-Zentrum München, 2012.

[33] R. Schwanker. Natürliche und zivilisatorische Strahlenexposition des Menschen. In *Grundkurs im Strahlenschutz für Ärzte und Medizinphysikexperten*. Helmholtz-Zentrum München, 2012.

[34] H. Schraube, V. Mares, S. Roesler, and W. Heinrich. Experimental verification and calculation of aviation route doses. *Radiation Protection Dosimetry*, 86:309–315, 1999.

[35] V. Mares, T. Maczka, G. Leuthold, and W. Rühm. Air crew dosimetry with a new version of EPCARD. *Radiation Protection Dosimetry*, 136:262–266, 2009.

[36] V. Mares and H. Yasuda. Aviation route doses calculated with EPCARD.Net and JISCARD EX. *Radiation Measurements*, 45:1553–1556, 2010.

[37] R.L. Bramblett, R.I. Ewing, and T. Bonner. A new type of neutron spectrometer. *Nuclear Instruments and Methods*, 9:1–12, 1960.

[38] D.J. Thomas and A.V. Alevra. Bonner sphere spectrometers - a critical review. *Nuclear Instruments and Methods in Physics Research A*, 476:12–20, 2002.

[39] S. Garny, V. Mares, and W. Rühm. Response functions of a Bonner sphere spectrometer calculated with GEANT4. *Nuclear Instruments and Methods in Physics Research A*, 604(3):612–617, 2009.

[40] C. Pioch, V. Mares, and W. Rühm. Influence of Bonner sphere response functions above 20 MeV on unfolded neutron spectra and doses. *Radiation Measurements*, 45:1263–1267, 2010.

[41] C. Pioch, V. Mares, W. Rühm, H. Iwase, Y. Iwamoto, T. Sato, M. Hagiwara, D. Satoh, Y. Nakane, H. Nakshima, Y. Sakamoto, H. Yashima, T. Matsumoto, A. Masuda, J. Nisahiyama, T. Itoga, C. Theis, E. Feldbaumer, L. Jägerhofer, A. Tamii, K. Hatanaka, and T. Nakamura. Calibration of a Bonner sphere spectrometer in quasi-monoenergetic neutron fields of 244 and 387 MeV. *Journal of Instrumentation*, 6:P10015, 2011.

[42] W.R. Leo. *Techniques for Nuclear and Particle Physics Experiments.* Springer, 1994.

[43] W. Rühm. Interaction of ionising radiation with matter. In *Advanced WE-Heraeus Physics School "Ionising Radiation and Protection of Man"*, Bad Honnef, 2012.

[44] ENDF/B-VI: Cross Section Evaluation Working Group,. ENDF/B-VI summary document, 1991.

[45] H. Krieger. *Strahlungsmessung und Dosimetrie.* Vieweg+Teubner, 2011.

[46] ICRP. Conversion coefficients for use in radiological protection against external radiation. In *ICRP Publications*, volume 74. International Commission on Radiological Protection, 1997.

[47] ICRU. Conversion Coefficients for use in Radiological Protection against External Radiation. In *ICRU Reports*, number 57. International Commission on Radiation Units and Measurements, 1998.

[48] R.H. Olsher, T.D. McLean, A.L. Justus, R.T. Devine, and M.S. Gadd. Personal dose equivalent conversion coefficients for neutron fluence over the energy range of 20–250 MeV. *Radiation Protection Dosimetry*, 138:199–204, 2010.

[49] M. Pelliccioni. Overview of fluence-to-effective dose and fluence-to-ambient dose equivalent conversion coefficients for high energy radiation calculated using the FLUKA code. *Radiation Protection Dosimetry*, 88(4):279–297, 2000.

[50] M. Luszik-Bhadra. A prototype personal neutron dosemeter with one Silicon diode. *Radiation Protection Dosimetry*, 96:227–229, 2001.

[51] M. Luszik-Bhadra, W. Wendt, and M. Weierganz. The electronic neutron/photon dosemeter PTB DOS-2002. *Radiation Protection Dosimetry*, 110:291–295, 2004.

[52] T. Lahaye, D. Cutarella, S. Ménard, and T. Bolognese-Milsztajn. The first operational dosemeter for neutrons which complies with IEC Standard 1323. *Radiation Protection Dosimetry*, 96:241–244, 2001.

[53] T. Nunomiya, S. Abe, K. Aoyama, and T. Nakamura. Development of advanced-type multi-functional electronic personal dosemeter. *Radiation Protection Dosimetry*, 126:284–287, 2007.

[54] T. Nakamura, M. Sasaki, O. Ueda, and T. Suzuki. Characterisation of a real-time personal neutron dosemeter with two Silicon detectors. *Radiation Protection Dosimetry*, 85:45–48, 1999.

[55] K. Aoyama, Y. Nagase, T. Suzuki, S. Watanabe, K. Taniguchi, K. Muramatsu, M. Fujita, and Y. Fujii. The development of new generation electronic personal dosimeters. In *Proceedings of IRPA-10*, Hiroshima, 2000. 10th International Congress of the International Radiation Protection Association.

[56] T. Bolognese-Milsztajn, D. Bartlett, M. Boschung, M. Coeck, G. Curzio, F. d'Errico, A. Fiechtner, V. Giusti, V. Gressier, J. Kyllönen, V. Lacoste, L. Lindborg, M. Luszik-Bhadra, C. Molinos, G. Pelcot, M. Reginatto, H. Schuhmacher, R. Tanner, F. Vanhavere, and D. Derdau. Individual monitoring, workplace monitoring and environmental dosimetry. *Radiation Protection Dosimetry*, 110:753–758, 2004.

[57] F. Vanhavere, D. Bartlett, T. Bolognese-Milsztajn, M. Boschung, M. Coeck, G. Curzio, F. d'Errico, A. Fiechtner, J. Kyllönen, V. Lacoste, T. Lahaye, L. Lindborg, M. Luszik-Bhadra, C. Molinos, H. Muller, M. Reginatto, H. Schuhmacher, and R. Tanner. Evaluation of individual monitoring in mixed neutron/photon fields: mid-term results from the EVIDOS project. *Radiation Protection Dosimetry*, 120:263–267, 2006.

[58] N. Tsujimura, T. Yoshida, and C. Takada. Responses of commercially available neutron electronic personal dosemeters in neutron fields simulating workplaces at MOX fuel fabrication facilities. *Radiation Measurements*, 46:1720–1723, 2011.

[59] S. Trinkl. Weiterentwicklung eines elektronischen Photonendosimeters und seine Integration in ein bestehendes elektronisches Neutronendosimeter. Master's thesis, Ludwig-Maximilians-Universität München, to be published.

[60] S. Hunklinger. *Festkörperphysik*. Oldenbourg, 2009.

[61] M.N. Rudden and J. Wilson. *Elementare Festkörperphysik und Halbleiterelektronik*. Spektrum Akademischer Verlag, 1995.

[62] L. J. Beattie, T. J. Brodbeck, A. Chilingarov, G. Hughes, S. A. McGarry, P. N. Ratoff, and T. Sloan. The electric field in irradiated silicon detectors. *Nuclear Instruments and Methods in Physics Research A*, 418:314–321, 1998.

[63] P. Bradley. *The Development of a Novel Silicon Microdosimeter for High LET Radiation Therapy.* PhD thesis, University of Wollongong, 2000.

[64] A. Castaldini, A. Cavallini, L. Polenta, F. Nava, and C. Canali. Electric field distribution in irradiated Silicon detectors. *Nuclear Instruments and Methods in Physics Research A*, 476:550–555, 2002.

[65] C. Hu. Alpha-particle-induced field and enhanced collection of carriers. *IEEE Electron Device Letters*, 3:31–34, 1982.

[66] L.D. Edmonds. A simple estimate of funneling-assisted charge collection. *IEEE Transactions on Nuclear Science*, 38(2):828–833, 1991.

[67] W.G. Abdel-Kader, S.S. El-Teleaty, and P.J. McNulty. Charge collection measurements and theoretical calculations for partially depleted Silicon devices. *Nuclear Instruments and Methods in Physics Research B*, 56/57:1246–1250, 1991.

[68] S. Agostinelli, J. Allison, K. Amako, J. Apostolakis, H. Araujo, P. Arce, M. Asai, D. Axen, S. Banerjee, G. Barrand, F. Behner, L. Bellagamba, J. Boudreau, L. Broglia, A. Brunengo, H. Burkhardt, S. Chauvie, J. Chuma, R. Chytracek, G. Cooperman, G. Cosmo, P. Degtyarenko, A. Dell'Acqua, G. Depaola, D. Dietrich, R. Enami, A. Feliciello, C. Ferguson, H. Fesefeldt, G. Folger, F. Foppiano, A. Forti, S. Garelli, S. Giani, R. Giannitrapani, D. Gibin, J.J. Gómez Cadenas, I. González, G. Gracia Abril, G. Greeniaus, W. Greiner, V. Grichine, A. Grossheim, S. Guatelli, P. Gumplinger, R. Hamatsu, K. Hashimoto, H. Hasui, A. Heikkinen, A. Howard, V. Ivanchenko, A. Johnson, F.W. Jones, J. Kallenbach, N. Kanaya, M. Kawabata, Y. Kawabata, M. Kawaguti, S. Kelner, P. Kent, A. Kimura, T. Kodama, R. Kokoulin, M. Kossov, H. Kurashige, E. Lamanna, T. Lampén, V. Lara, V. Lefebure, F. Lei, M. Liendl, W. Lockman, F. Longo, S. Magni, M. Maire, E. Medernach, K. Minamimoto, P. Mora de Freitas, Y. Morita, K. Murakami, M. Nagamatu, R. Nartallo, P. Nieminen, T. Nishimura, K. Ohtsubo, M. Okamura, S. O'Neale, Y. Oohata, K. Paech, J. Perl, A. Pfeiffer, M.G. Pia, F. Ranjard, A. Rybin, S. Sadilov, E. Di Salvo, G. Santin, T. Sasaki, N. Savvas, Y. Sawada, S. Scherer, S. Sei, V. Sirotenko, D. Smith, N. Starkov, H. Stoecker, J. Sulkimo, M. Takahata, S. Tanaka, E. Tcherniaev, E. Safai Tehrani, M. Tropeano, P. Truscott, H. Uno, L. Urban, P. Urban, M. Verderi, A. Walkden, W. Wander, H. Weber, J.P. Wellisch, T. Wenaus, D.C. Williams, D. Wright, T. Yamada, H. Yoshida, and D. Zschiesche. Geant4 - A simulation toolkit. *Nuclear Instruments and Methods in Physics Research A*, 506:250–303, 2003.

[69] J. Allison, K. Amako, J. Apostolakis, H. Araujo, P.A. Dubois, M. Asai, G. Barrand, R. Capra, S. Chauvie, R. Chytracek, G.A.P. Cirrone, G. Cooperman, G. Cosmo, G. Cut-

tone, G.G. Daquino, M. Donszelmann, M. Dressel, G. Folger, F. Foppiano, J. Generowicz, V. Grichine, S. Guatelli, P. Gumplinger, A. Heikkinen, I. Hrivnacova, A. Howard, S. Incerti, V. Ivanchenko, T. Johnson, F. Jones, T. Koi, R. Kokoulin, M. Kossov, H. Kurashige, V. Lara, S. Larsson, F. Lei, O. Link, F. Longo, M. Maire, A. Mantero, B. Mascialino, I. McLaren, P.M. Lorenzo, K. Minamimoto, K. Murakami, P. Nieminen, L. Pandola, S. Parlati, L. Peralta, J. Perl, A. Pfeiffer, M.G. Pia, A. Ribon, P. Rodrigues, G. Russo, S. Sadilov, G. Santin, T. Sasaki, D. Smith, N. Starkov, S. Tanaka, E. Tcherniaev, B. Tome, A. Trindade, P. Truscott, L. Urban, M. Verderi, A. Walkden, J.P. Wellisch, D.C. Williams, D. Wright, and H. Yoshida. Geant4 developments and applications. *IEEE Transactions on Nuclear Science*, 53:270–278, 2006.

[70] MCNP - A General Monte Carlo N-Particle Transport Code. `http://mcnp-green.lanl.gov`.

[71] J. P. Biersack and L. G. Haggmark. A Monte Carlo computer program for the transport off energetic ions in amorphous targets. *Nuclear Instruments and Methods*, 174:257–269, 1980.

[72] H. Pauw. *Energy Spectra Of Radioactive Neutron Sources.* PhD thesis, Universiteit van Amsterdam, 1970.

[73] S. Trinkl. Untersuchungen zur Verbesserung eines Bonner Vielkugelspektrometers, 2010. Bachelor Thesis, Ludwig-Maximilians-Universität München.

[74] G. Andersson-Lindström and B. Zausig. Nachweis der Reaktion $Si^{28}(n,p)Al^{28}$ in Siliciumhalbleiterzählern bei Neutronenenergien um 14 MeV. *Annalen der Physik*, 7:187–293, 1965.

[75] K.W. Burn. Monte Carlo from binomial to quasi-analogue to deep penetration. In *Advanced WE-Heraeus Physics School "Ionising Radiation and Protection of Man"*, Bad Honnef, 2012.

[76] T. Koi. Thermal neutron scattering from nuclei within chemically bound atoms in Geant4. In *IEEE Nuclear Science Symposium and Medical Imaging Conference.* Standford Linear Accelerator Center, 2006.

[77] S. Garny, G. Leuthold, V. Mares, H.G. Paretzke, and W. Ruhm. GEANT4 transport calculations for neutrons and photons below 15 MeV. *IEEE Transactions on Nuclear Science*, 56(4):2392–2396, 2009.

[78] ROOT | A Data Analysis Framework. `http://root.cern.ch/drupal/`.

[79] L. Urban and V. Ivanchenko. *Geant4 Physics Reference Manual.* Geant4 Collaboration, 2009.

[80] H. Bertini. Low-energy intranuclear cascade calculation. *Physical Review*, 131:1801–1821, 1963.

[81] H. Bertini. Intranuclear-cascade calculation of the secondary nucleon spectra from nucleon-nucleus interactions in the energy range 340 to 2900 MeV and comparisons with experiment. *Physical Review*, 188:1711–1730, 1969.

[82] J. Röhrich, T. Damerow, W. Hahn, U. Müller, U. Reinholz, and A. Denker. A Tandetron^{TM} as proton injector for the eye tumor therapy in berlin. *Review of Scientific Instruments*, 83:02B903, 2012.

[83] K. Niita, N. Matsuda, Y. Iwamoto, H. Iwase, T. Sato, H. Nakashima, Y. Sakamoto, and L. Sihver. PHITS: Particle and Heavy Ion Transport code System, 2010. `http://jolissrch-inter.tokai-sc.jaea.go.jp/pdfdata/JAEA-Data-Code-2010-022.pdf`.

[84] M. Caresana, M. Ferrarini, G. Manessi, M. Silari, and V. Varoli. LUPIN, a new instrument for pulsed neutron fields. 2012. to be published.

[85] Reference neutron radiations. Technical report, International Organization for Standadization (ISO), 2000.

[86] F. Bergmeier. Measurement of doses of secondary neutrons from cosmic radiation by means of various REM counters - results obtained at the Umweltforschungsstation Schneefernerhaus, 2011. Bachelor Thesis, Ludwig-Maximilians-Universität München.

[87] U. Ackermann. Verbesserung eines Bonner Vielkugelspektrometers zum Nachweis von sekundären Neutronen der kosmischen Strahlung, 2011. Diploma Thesis, Technische Universität München.

[88] H. Schraube, J. Jakes, A. Sannikov, E. Weitzenegger, S. Roesler, and W. Heinrich. The cosmic ray induced neutron spectrum at the summit of the Zugspitze. *Radiation Protection Dosimetry*, 70:405–408, 1997.

[89] W.R. Mills, R.L. Caldwell, and I.L. Morgan. Low voltage ^3He-filled proportional counter for efficient detection of thermal and epithermal neutrons. *Review of Scientific Instruments*, 33:866–868, 1962.

[90] A. Sannikov, V. Mares, and H. Schraube. High energy response functions of Bonner spectrometers. *Radiation Protection Dosimetry*, 70:291–294, 1997.

[91] M. Matzke. Unfolding procedures. *Radiation Protection Dosimetry*, 107:155–174, 2003.

[92] G. Simmer, V. Mares, E. Weitzenegger, and W. Rühm. Iterative unfolding for Bonner sphere spectrometers using the MSANDB code - sensitivity analysis and dose calculation. *Radiation Measurements*, 45:1–9, 2010.

[93] National Semiconductor Corporation. *LM117/LM317A/LM317 3-Terminal Adjustable Regulator*, 2004.

[94] T. Sato and N. Koji. Analytical functions to predict cosmic-ray neutron spectra in the atmosphere. *Radiation Research*, 166:544–555, 2006.

[95] T. Sato, H. Yasuda, K. Niita, A. Endoa, and L. Sihverd. Development of PARMA: PHITS-based analytical radiation model in the atmosphere. *Radiation Research*, 170:244–259, 2008.

[96] B. Wiegel, S. Agosteo, R. Bedogni, M. Caresana, A. Esposito, G. Fehrenbacher, M. Ferrarini, E. Hohmann, C. Hranitzky, A. Kasper, S. Khurana, V. Mares, M. Reginatto, S. Rollet, W. Rühm, D. Schardt, M. Silari, G. Simmer, and E. Weitzenegger. Intercomparison of radiation protection devices in a high-energy stray neutron field. Part II: Bonner sphere spectrometry. *Radiation Measurements*, 44:660–672, 2009.

[97] W. Press, S. Teukolsky, W. Vetterling, and B. Flannery. *Numerical Recipes: The Art of Scientific Computing*. Cambridge University Press, 3rd edition, 2007.

[98] M. Galassi, J. Davies, J. Theiler, B. Gough, G. Jungman, P. Alken, M. Booth, and F. Rossi. *GNU Scientific Library Reference Manual*. Network Theory Ltd., 3rd edition, 2009.

[99] C. Robert and G. Casella. *Monte Carlo Statistical Methods*. Springer, 2nd edition, 2004.

[100] F. Salvat. Monte Carlo simulation. Detailed schemes and condensed-history methods. In *Advanced WE-Heraeus Physics School "Ionising Radiation and Protection of Man"*, Bad Honnef, 2012.

[101] B. Stroustrup. *The C++ Programming Language*. Addison-Wesley, 3rd edition, 1997.

[102] F. Salvat. PENELOPE. A code system for Monte Carlo simulation of electron and photon transport. In *Advanced WE-Heraeus Physics School "Ionising Radiation and Protection of Man"*, Bad Honnef, 2012.

[103] H. Iwase, K. Niita, and T. Nakamura. Development of general-purpose particle and heavy ion transport monte carlo code. *Journal of Nuclear Science and Technology*, 39:1142, 2002.

[104] J. C. McDonald, J. E. Tanner, R. D. Steward, R. Michel, M. K. Murphy, and R. J. Traub. Effect of phantom size and composition on neutron dosemeter reading. *Radiation Protection Dosimetry*, 59(4):263–268, 1995.

[105] F. James. A review of pseudorandom number generators. *Computer Physics Communications*, 60:329–344, 1990.

[106] The Message Passing Interface (MPI) standard. `http://www.mcs.anl.gov/research/projects/mpi/`.

[107] M. J. Berger, J. S. Coursey, M. A. Zucker, and J. Chang. Stopping-Power and Range Tables for Electrons, Protons and Helium Ions, 2011. `http://www.nist.gov/pml/data/star/index.cfm`.

A. Details on the Monte Carlo simulations with Geant4

Generally speaking, the *Monte Carlo method* refers to the *stochastic treatment* of a given problem, in contrast to deterministic simulations (e.g. Finite Element method). It relies on a statistical analysis of a huge number of *events* that are simulated independently, yielding the quantities of interest as mean values. The evolution of each of these single events is governed by *random numbers* which are generated by the Monte Carlo engine. The *distributions* those numbers are sampled from represent the *input* to the simulation, as they must be chosen to describe the problem in question. ([99, 100])

In radiation physics, the Monte Carlo method is widely used (e.g. [87, 39, 75, 5]). In that case, one event refers to the *transport* of a *primary particle*, e.g. a neutron, and the *secondary particles* produced at interactions of that particle, through a given *geometry*, e.g. the dosemeter. The result yielded by one such event is for example the track, the energy deposition in a certain volume, or the number of interactions. As stated above, by the analysis of numerous event results, the mean value (and variance), i.e. the overall simulation result, is acquired.

A.1. Structure of the Geant4 framework

GEANT4 ([26, 68, 69]) is a Monte Carlo framework written in C++ ([101]) which is being developed at CONSEIL EUROPÉEN POUR LA RECHERCHE NUCLÉAIRE (CERN). The name "Geant" stands for "GEometry ANd Tracking". Using the GEANT4 framework, the programmer is provided with a number of base classes; in order to create own applications, i.e. to simulate a certain problem, the user has to inherit from these. In the derived classes it is possible to specify the problem; they are then handed to the GEANT4 Monte Carlo engine incorporated in the *G4RunManager* class which is used to control and run the simulation itself. For that, a basic command-line user interface is provided, as well as a simple visualization of the geometry.

The main classes that have to be implemented by the user are the ones describing the geometry to be simulated, the particle beam (i.e. particle type, energy, direction), the physics to be applied and the scoring of the event results.

Geometry

The *Geometry* description class is usually derived from *G4VUserDetectorConstruction*, which is an abstract base class.[1] Three steps have to be taken in order to define the geometry. First, the *solids* are created; for that, GEANT4 provides various basic types of solids, for example boxes, spheres, cones etc. The dimensions of those solids are given by the user and are usually implemented in the class definition. Also, *boolean solids* can be created as intersections or unions of basic solids.

As a second step, *logical volumes* are defined from the basic solids; in order to do that, those volumes are assigned different *materials*, which can be either taken from an internal database ([27]) or constructed from isotopes. Thus, materials with specific isotopic compositions can be used. The materials´ properties concerning the interactions with different kinds of particles are then automatically computed by the GEANT4 run manager, depending on the physics list chosen for the simulation (see below).

The third step in geometry definition is the *placement* of the volumes. These can be positioned relative to the world, i.e. the mother volume all others are placed into, or within each other. Thus, volumes can be designed to hold an arbitrary number of daughter volumes, which however are not allowed to overlap and must not exceed their mother volume. The corresponding boundaries are computed and handled by the framework as long as the placement is done correctly. To ensure this, geometry tests are provided by GEANT4 that can be run on the command-line.

Beam

For the particle *beam*, usually a derived class of *G4VUserPrimaryGeneratorAction* is handed to the GEANT4 engine. In that class, a function *GeneratePrimaries* is implemented, which defines the position, momentum direction, energy and type of each newly created particle. These quantities are usually combined in a so-called *particle gun*, which provides a monoenergetic pencil-beam. In the Primary Generator class however, the parameters describing this gun can be altered for each event yielding for example an energy distribution or a certain beam width. These modifications can then be controlled by random numbers being sampled from appropriate distributions, conforming to the Monte Carlo philosophy.

Physics

The *physics* incorporated in the GEANT4 simulations is usually referred to as the *physics list* applied in a specific simulation. A physics list contains the *particle definitions* that are necessary, a number of different *models*, and the physical *processes* that these models are related to. Thus, for a certain process, like for example elastic scattering of neutrons or pair-

[1] The concept of an abstract geometry class means that users are forced to implement a derived class; this prevents them from running simulations that have no geometry description. For the other necessary implementations, similar means are employed in the GEANT4 framework.

production of photons, several models can be registered; which of them is chosen by the Monte Carlo engine depends on the particle energy, as the models are applicable for distinct energy ranges only.

For the description of electrons, positrons and photons, the *electromagnetic* physics has to be defined. There are two model collections available, which are the *Livermore* and the *Penelope* physics ([79, 102]). They represent extensions to the standard electromagnetic physics models implemented in GEANT4, with slightly altered cross sections for elastic scattering in a very wide energy range up to 1 GeV. To use them in a physics list, a *modular* physics list has to be created, to which the appropriate collection is handed.[2]

In contrast to that, for *hadronic* interactions and the corresponding models, pre-defined physics lists are incorporated in GEANT4. In that regime, the models describing the various processes are very different depending on the kinetic energy of the particle of interest. At very high energies, that is for $E \gtrapprox 12\,\mathrm{GeV}$, for example the *quark gluon string precompound model* or the parametrized *Gheisha model* are used to describe inelastic interactions ([79]). At lower energies, *intra-nuclear cascade models* (INC) are applied. The most important among these are the *Bertini model* ([80, 81]) and the GEANT4 *Binary model* ([79, 5]). It is an active area of research which model can be used to reproduce measured data, and in what situations it can be applied (e.g. [41, 5]). A Bertini-like model is also implemented in other Monte Carlo codes, for example the PHITS code ([83, 103]).

For *neutrons*, the hadronic models can be employed down to kinetic energies of several MeV. At energies below 20 MeV, special treatment of neutron processes is possible in GEANT4. For these energies, cross sections (see section 2.2) are provided, which are taken from the widely used ENDF-B/VI database ([44]); consequently, neutron interaction processes can be described very accurately even in the energy range where the INC models do not apply.[3] In the GEANT4 framework, the "model" utilizing the cross section data is referred to as the *High Precision Neutron Package* (HP). It can be registered as a model to processes just like the hadronic INC and high energy models as well.

The pre-defined hadronic physics lists are compilations of a high-energy model collection, a INC model collection and, if neutrons are required, the HP neutron package. For using Bertini or Binary INC and the quark gluon string model as well as the neutron cross sections, the physics lists *QGSP_BERT_HP* and *QGSP_BIC_HP* can be instantiated in the simulation and registered to the run manager. Those physics lists, or rather their C++ source code, can also be used as a starting point for a custom physics list.

Such a custom list is for example needed if very low energetic neutrons are to be simulated. In that case, the scattering of neutrons is no longer described accurately by the HP package, since this gives the cross sections for scattering on single nuclei only, which is referred to as the *free gas approximation*. If the kinetic energy of the neutrons is in the order of the binding energy of a molecule, this approximation is not valid any more and a cross section

[2] The Livermore and Penelope collections are thus called *Physics Constructors*.
[3] C. Pioch (HMGU), private communication

for scattering on the whole molecule must be applied, which is given in terms of the so-called $S(\alpha, \beta)$ matrix ([76, 77, 39, 5]). Currently, GEANT4 provides cross sections for neutron interactions at thermal energies with three materials only, which are *water*, *polyethylene* and *graphite*. They can be applied by following the instructions given in [76].

When defining the physics list, the user may assign a certain default *range cut*. The concept of *cuts* is necessary when applying the Monte Carlo method in radiation science ([100]). Generally, the cut value refers to a certain *energy*. Particles are tracked by the Monte Carlo engine until their energy reaches a value below the cut value; then, their energy is deposited locally or their track is continued using a simplified method, e.g. the *Continuous Slowing-Down Approximation* (CSDA, [45, 28, 29]). In GEANT4, the cut values are given as *cuts in range*; that is, for all combinations of materials and particles that occur in a simulation, the given range is translated to a certain energy. During the simulation run, particles are then tracked down to zero range ([27, 79]), i.e. to thermal energy in the case of neutrons. However, *secondary particles* are not actually produced if their energy would be below the cut value; instead, their energy is deposited locally. So, by adjusting the cut value, it is possible to alter the accuracy and also the speed of a simulation. In complex geometries, it is also possible to define various *regions* with different values for the range cut. So, it is possible to apply a very low cut value in a region where high accuracy is required and at the same time assign a high cut value in other areas speeding up the overall simulation.

Scoring

The purpose of a Monte Carlo simulation is to infer from a huge number of events by analyzing them statistically. Thus, it is necessary to extract the desired information from the simulation runs by so-called *scorers*. In GEANT4, scorers are classes that are attached to the logical volumes the geometry is constructed of and which are used to read out certain quantities for each event. If the corresponding volume is passed by a particle track, the scorer yields the quantity in question and hands it to a specialized object to store the data, e.g. a *G4HitsMap* or a user-defined class. By attaching several scorers to a volume, all necessary information on an event can be inferred.

Several so-called *primitive scorers* are included in the GEANT4 framework that can be used to record basic quantities like energy deposition or track length; moreover, *filters* can be applied to scorers making them sensitive to certain particles only. The source code of the primitive scorers can also be used as a starting point to write more specialized recording classes.

A.2. Design of the dosemeter simulations

In order to simulate the HMGU dosemeter, several applications were created with the GEANT4 framework. For the present work, release version *9.3* with *patch 02* of the library was used ([26, 27]). In the created programs, the classes mentioned in the above section A.1 were

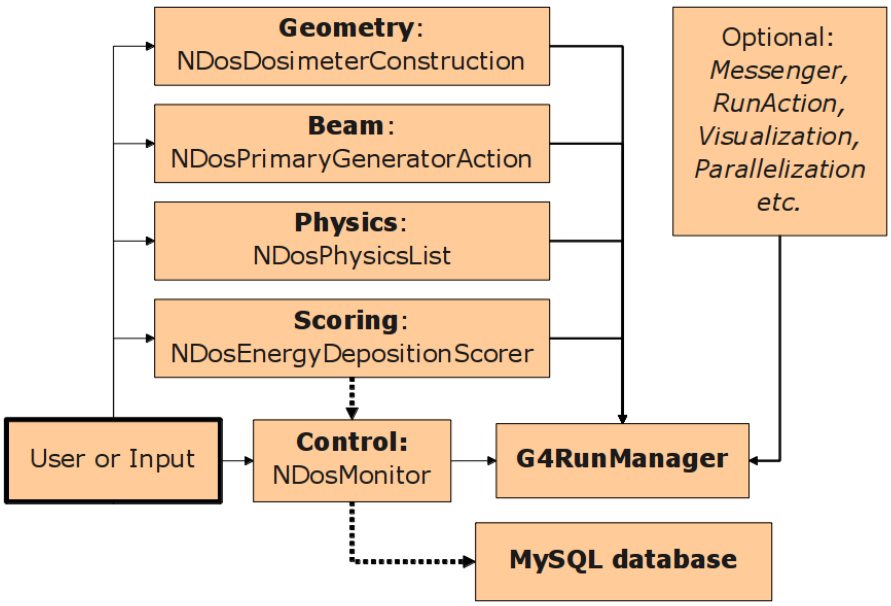

Figure A.1.: C++ classes implemented for the dosemeter simulations; the arrows indicate interconnections via pointers ([101]) and the flow of data

implemented, along with some other classes derived or created for practical reasons. The main difference between the various simulations is the implementation of the geometry class, which of course depends on what part, i.e. sensor, of the dosemeter is to be simulated.

The structure of the simulation applications is shown schematically in figure A.1. As described previously, the most important classes are the ones concerning the geometry, the beam, the physics and several scorers.

For the geometry, different implementations were made, describing either single sensors or the whole dosemeter device. The materials necessary to create the logical volumes were taken from the internal GEANT4 database, unless a specific isotopic or atomic composition was needed to reproduce the design of the device. Thus, for example the LiF converter of the Delta and Albedo sensors was created manually, since in that case the ^6Li abundance of 96 % (see page 35) differs from the natural one given in the database; also, here a mixture of materials with glue and LiF had to be implemented ([25]). Materials not listed in the database, like epoxy, were created manually from elements, but with natural isotopic composition. The densities of most materials were entered by hand; the difference to the densities listed in the database was less than a few percent however.

Projections of the geometry used in the simulations are shown in figure 4.1 on page 44. They were created by the OPENGL viewer included in GEANT4. In 4.1a, a geometry with only the single sensor, the Fast here, is depicted. For the area A of the sensor, i.e. the converter, the detector and the Al_2O_3 substrate, $A = 200\,\mathrm{mm}^2$ was assumed. The thickness of the lead or cadmium housing was taken to be 1 mm. In 4.1b, the geometry for the simulation of the whole dosemeter is displayed. The dimensions implemented here were acquired by measuring

the dosemeter head of a real device. The outer width of the steel box the B_4C filling is brought into is 60.4 mm; the thickness of the device is 16.2 mm. The circuit boards, in which the sensors are placed, are $50.4 \times 50.4\,\mathrm{mm}^2$. At the positions of the sensors, gaps were created using boolean solids (see section A.1).

For later simulations with the Delta and Albedo sensors, not only the whole geometry of the dosemeter was implemented, but also a slab phantom. This was necessary as the Albedo sensor crucially relies on backscattered neutrons from a phantom, as described in section 3.3.3; thus the phantom served to compare measured and simulated data. In the case of the Delta sensors, the impact of the phantom on the number of counts in Delta D1 and G1 (see section 3.3.2) had to be studied. Figure 4.1c shows the geometry used in the case of a phantom, with the dosemeter attached to the phantom surface. Its dimensions are $30 \times 30 \times 15\,\mathrm{cm}^3$; the material is *plexiglass*, i.e $(C_5H_8O_2)_n$. Although a water phantom should be used in order to reproduce a dose value described by the quantity $H_p(10)$ (see section 2.3), all experiments described in this work were conducted with a plexiglass phantom, since the difference is considered negligible[4] ([104]). Thus, of course, the phantom in the simulations was plexiglass as well.

The beam used in the simulations of the sensors and the dosemeter was implemented utilizing the *G4ParticleGun* class described above. As mentioned there, the beam was not designed as a pencil beam, but a certain width d_B^2 was implemented using the random number generator. Thus, the original position of a neutron being simulated is sampled from a square area for each event. The dimension of this square area is referred to as the beam width; e.g., to irradiate the dosemeter device housing, a width of $d_B^2 = 60.4 \times 60.4\,\mathrm{mm}^2$ is needed. The energy of the incident particle can also be sampled from a Gaussian distribution, whose width ΔE_n has to be given by the user. In most cases, however, this functionality was not used, and a mono-energetic beam was applied. The values of the parameters controlling the beam behavior, i.e. ΔE_n and d_B, must be given by the user, so a *Messenger class* was created that enabled command line options to edit these quantities during run-time. In some simulations (the parallelized ones, see below), however, the beam and energy widths were implemented in a hard-coded way, as the input was applied by a script and not during run-time then.

For the simulations of the neutron dosemeter, of course a hadronic physics list as described in supplement A.1 was used. It was implemented as a custom physics list derived from the *Modular Physics List* base class. The code was similar to the pre-defined *QGSP_BERT_HP* and *QGSP_BIC_HP* lists, which were used as samples for the custom one. The constructor (or part of it) of the *NDosPhysicsList* class is shown in listing A.1. One can see that this class is derived from the modular physics list class first. The individual model collections are then introduced using the *RegisterPhysics* member function. These collections, like the *Penelope* physics used here, are *Physics Constructors*; registering them enables the physics list to provide their models to the Monte Carlo engine. As shown in the listing, the pre-defined hadronic physics lists also rely on Physics Constructors as model collections; these are denoted as *HadronPhysicsQGSP_BIC_HP* for the *Binary* INC and *HadronPhysicsQGSP_BERT_HP*

[4] M. Wielunski (HMGU), private communication

Algorithm A.1 Constructor ([101]) of the *NDosPhysicsList* class

```
NDosPhysicsList::NDosPhysicsList(G4int verbose)
    : G4ModularPhysicsList(verbose)
{

    this->defaultCutValue = 0.7*mm;

    // EM Physics
    this->RegisterPhysics( new G4EmPenelopePhysics(verbose));

    ...

    // Hadron Elastic scattering
    this->RegisterPhysics(
        new NDosHadronElasticPhysics("elastic",verbose,1));

    // Hadron Physics
    this->RegisterPhysics(
        new HadronPhysicsQGSP_BIC_HP("hadron",1));
/* or:
    this->RegisterPhysics(
        new HadronPhysicsQGSP_BERT_HP("hadron",1)); */

    ...

}
```

for the *Bertini* INC (see A.1). For most simulations, the Binary model was used, since with the Bertini model slight discrepancies at the transition from cross-section based calculations to the model at $E_n = 20\,\mathrm{MeV}$ were observed (see section 4.2 on page 66).

The elastic scattering of the hadrons is in GEANT4 sourced out of the hadron physics collections to a separate physics constructor, here denoted as *NDosHadronElasticPhysics*. That collection was implemented as well, as here the thermal scattering of neutrons described by the $S(\alpha, \beta)$ matrix had to be enabled. This functionality was however activated as a test when simulating a phantom only, since the thermal scattering models slow down the speed of the applications to a prohibitive value. In the cases where thermal scattering was activated, the cross sections of polyethylene were used for the plexiglass molecules in the phantom. Since currently no thermal cross sections for the latter material are included in GEANT4, that procedure was the best approximation possible.

As can be seen from the "HP" in the hadron physics constructors´ names, the *High Precision Neutron Package* relying on the ENDF-B/VI database was used for neutrons below $E_n = 20\,\mathrm{MeV}$ (see supplement A.1). For that, the cross section data available on the web page [26] appropriate for the GEANT4 version *9.3.p02* was taken. Since it was reported[5] that with these cross sections and that version of GEANT4 , the kinematics of the $^6Li\,(n,\alpha)\,^3H$ nuclear reaction (3.7) is not calculated correctly, the files containing the ^6Li data were replaced by

[5] Z. Hartwig (MIT), `http://hypernews.slac.stanford.edu:5090/HyperNews/geant4/get/hadronprocess/1045.html`, in the GEANT4 Forum at SLAC

Algorithm A.2 Class declaration of *NDosMonitor*

```
class NDosMonitor {

public:

    void setSimID(int id);

    void setNeutronEnergy(double energy);

    int dumpToTable();

    void printEvent( ... );

    void addEnergyFast(int layer, double energy);

    void incrEvent();

    void setCutOff(double cutoff);

    ...

private:

    ...

}
```

the ones from a newer version.

For the scoring of the results of each event, a dedicated scoring class *NDosEnergyDepositionScorer* was implemented, following the design of the primitive energy deposition scorer as described in the previous section. Like the primitive scorer, this one records the energy deposited in the volume it is attached to. The difference, however, is that in the case of the dosemeter simulations, not the usual result collection based on the *G4HitsMap* class was employed, but rather a specialized *Observer* class, called *NDosMonitor*. As can be seen from figure A.1, the data acquired by the scorers is handed to the *monitor*, which serves as both storage and output interface. Thus, the *NDosMonitor* class is the central element of the applications. The data handling is implemented there using *std::vector* containers from the C++ standard template library ([101]). In listing A.2, a part of the public interface of this class is shown. The scorers, that hold a pointer to it, utilize its *addEnergyFast*, *addEnergyAlbedo* etc. member functions, depending on which detector they are used for. The energy depositions are then summed up for each scorer and each event by the monitor class.

Besides the scorers, also the other derived classes hold pointers to *NDosMonitor*. Thus, the primary generator informs the monitor on the neutron energy E_n for each event using the *setNeutronEnergy* class; moreover, the end of a certain event and beginning of the next one is communicated by invoking the *incrEvent* class; the *event number* is handled by *NDosMonitor* alone. If energy was deposited during the event, the total energy deposition and the corresponding sensor is displayed on the screen by the monitor class using its *printEvent* member

function.

As shown in figure A.1, the data is passed by the *NDosMonitor* to a *MySQL database*. There, all energy deposition values for all events of a simulation are stored, along with the sensor name, the scoring layer (see below) and the event number. The member function to accomplish this is *dumpToTable*, which is called if the results collection in *NDosMonitor* reaches a certain length. This procedure both serves as a backup of data, and enables analysis and reanalysis of simulation runs at later times. However, as all outputs are stored, the memory consumption of the database is huge in many cases. For long-running simulations, then, a *cut-off* E_{cut} was applied, below which the events are not stored in the database. This cut refers to the total energy deposition during one event, and has in no way to do with the *range cuts* describe above. If the cut value is chosen small enough, i.e. $E_{cut} < E_{thresh}$, no difference in the response calculated from the simulations occurs. This is because the general features of pulse height spectra, as shown in section 4.1, are not dependent in their very low-energetic regions, where mainly photons (e.g. from (n, γ) reactions) contribute to the signals. In those regions, however, the total number of pulses is huge, so that the application of a cut-off is profitable. Typical values for E_{cut} are $E_{cut} = 10 \ldots 500\,\mathrm{keV}$; they are given by the user or an input file and handed to the monitor class using the *setCutOff* function.

In order to be stored in a database, the outputs must be assigned a certain *key* for identification. This key is referred to as the *SimID*; it is given by the user and passed to *NDosMonitor* with the *setSimID* function. Here, the *SimID* is a integer number which is set for each simulation run. In the analysis, the data can then be identified according to their key, which is the *SimID* passed by the monitor as well. The *SimID* also serves as a *seed* for the random number generator, which is is a version of the *HepJamesRandom* engine described in [105].

The classes described in the previous paragraphs correspond to the classes needed for a basic simulation as shown in supplement A.1. As can be seen from figure A.1, several other optional functionalities were implemented for the dosemeter simulations. Among them are the messenger classes enabling command-line options for the user to adjust beam width and energy, set the *SimID* etc. The *RunAction* class provides information on the simulation run and puts them out on the screen, as well as it triggers the *dumpToTable* function of *NDosMonitor*.

As written above, basic visualization possibilities are part of the GEANT4 toolkit. Thus, to enable the creation of pictures as shown in figure 4.1, the colors and drawing parameters of the various volumes had to be given in the geometry class *NDosDosimeterConstruction*. The actual rendering is then controlled by either user-interface commands or a script; in order to speed up simulations however, no visualization was applied in most cases.

For parallelization of the programs, the *MPI* library (*Message Passing Interface*, [106]) was used. Like most Monte Carlo applications, the dosemeter simulation could be parallelized in a trivial way; the number of events to be simulated had to be distributed on several *processes* running in a multi-core environment. In that case, however, the user interface had to be dropped, so that all inputs had to be given in a *input file*. The parameters, i.e. *SimIDs*, *cut-offs*, *neutron energies* and *number of events per energy*, were then passed to the different program

processes by the *MPI* functions. This procedure was especially important when simulating with a phantom, for example when investigating the Albedo detector (see section 4.1.3 on page 60). The parallelized programs were usually run on a *Intel i3* dual-core PC with four CPU nodes (via *Hyper-Threading*). In the case of very long-running simulations with a phantom, four *Intel i7* computers at the Physics Department of the TU MÜNCHEN were used, with 24 nodes altogether.

A.3. Analysis of the simulation results

The output of the dosemeter simulation programs is the data produced by the various *scorers* during run-time. It is stored in a MYSQL *database*, as described in supplement A.2. For analysis purpose, the data could then be read from the database afterwards.

For analyzing the simulation results, in general two steps were taken. First, *pulse height* or *energy collection spectra* were created for each sensor and each simulation, i.e. histograms of the number of events N_{events} per interval of collected energy E_{coll}. Then, by integration, the *response* of a particular sensor could be inferred from the corresponding pulse height spectrum. In order to accomplish these two tasks, ROOT was used, which is a powerful statistics framework. Like GEANT4, ROOT is developed at CERN ([78]). It provides a C++ interpreter which can be utilized to run user-defined *scripts*, which are designed to read and analyze the data and produce graphs and figures.

When creating pulse height spectra for a simulation output, attention has to be paid to the *charge collection efficiency* (CCE) ϵ_q and its dependence on depth z below the detector surface, as described in section 3.2. The figure on page 32 shows the function $\epsilon_q(z)$ assumed for the detectors used in the HMGU dosemeters. One can see that in general, an energy deposition E_{dep} in a arbitrary depth of the detector does not contribute to the signal E_{coll} to full extend, but only to a fraction equivalent to the CCE at that depth. In order to incorporate this behavior into the analysis, the Silicon detectors in the dosemeter simulations were designed as a stack of thin *layers*. Altogether, between 100 and 200 layers were used to model a 400 μm detector, so one layer consisted of a Silicon film of between 2 μm and 4 μm. Each was assigned a separate *scorer* as described above, yielding entries in the database for each event in which energy was deposited in the corresponding layer. In the analysis then, that energy deposition was weighted according to the value of ϵ_q appropriate for the depth of the layer. Thus for a single event, the *pulse height* or *signal* is given by

$$E_{coll} = \sum_l E_{dep,l} \cdot \epsilon_q(z_l) \tag{A.1}$$

with the sum running over all layers $l = 1 \ldots 100$ or $l = 1 \ldots 200$.

The implementation of this procedure in the analysis scripts is given in listing A.3. The *table* vector array holds all the data that is read from the database for a certain simulation and a certain sensor; the *cce* vector contains the ϵ_q values for the layers. In the *for-loops*

Algorithm A.3 Application of equation (A.1) and creation of a pulse height spectrum in a ROOT script

```
TH1D* createPulseHeightSpectrum(...) {

    // Read data and CCE:
    std::vector<double>* table = readTable(...);
    std::vector<double>* cce = readCCE(...);
    ...

    // Weight depositions according to CCE:
    std::vector<double>* signals = new std::vector<double>;
    for (int j = 0; j < numEntries; ++j) {
        double energy = 0.0;
        for (int k = 0; k < numLayers; ++k) {
            energy += ( cce->at(k) * table[k].at(j) );
        }
        signals->push_back(energy);
    }
    ...

    // Create pulse height histogram:
    TH1D* histogram = new TH1D(...);
    std::vector<double>::iterator iter = signals->begin();
    std::vector<double>::iterator end = signals->end();
    while ( iter != end ) {
        histogram->Fill(*iter);
        ++iter;
    }
    histogram->Scale("width");
    ...

    delete cce;
    delete signals;
    delete[] table;
    return histogram;
}
```

following, equation (A.1) is applied for all events independently, yielding a *pulse height* E_{coll} (called *energy* here) for each; these pulse height values are stored in the new vector *signals*. The newly created *histogram* (ROOT C++ class *TH1D*) is then filled with those values in the *while-loop* (using *iterators*, [101]). By applying the *Scale* member function of the histogram class, the spectrum is normalized to the bin width, yielding a distribution $\frac{\mathrm{d}N_{events}}{\mathrm{d}E_{coll}}$ in the end. Usually, the spectrum was normalized to the number of incoming neutrons as well, which was of course related to the neutron fluence Φ_n and the sensors area $A = 2.0\,\mathrm{cm}^2$ via

$$N_n = \Phi_n \cdot A \tag{A.2}$$

Since the number of counts N_{events} is proportional to the number of incoming neutrons, the

two representations are equivalent:

$$\frac{\mathrm{d}N_{events}}{\mathrm{d}E_{coll}} \propto \frac{1}{N_n} \cdot \frac{\mathrm{d}N_{events}}{\mathrm{d}E_{coll}} = \frac{\mathrm{d}^2 N_{events}}{\mathrm{d}N_n \mathrm{d}E_{coll}} \tag{A.3}$$

The *number of counts* for the incident neutron fluence used in a simulation can be inferred from the pulse height spectrum (A.3) by integration. As described in section 3.1, all events leading to a signal higher then the sensor´s threshold, i.e. $E_{coll} \geq E_{thresh}$, constitute a *count*. Thus, the number of events above E_{thresh} in the pulse height spectrum yields the number of counts N_c via

$$N_c = \int_{E_{thresh}}^{\infty} \mathrm{d}E_{coll} \cdot \frac{\mathrm{d}N_{events}}{\mathrm{d}E_{coll}} = N_n \cdot \int_{E_{thresh}}^{\infty} \mathrm{d}E_{coll} \cdot \frac{\mathrm{d}^2 N_{events}}{\mathrm{d}N_n \mathrm{d}E_{coll}} \tag{A.4}$$

By adjusting the number of incident neutrons N_n in the above formula (A.4), the theoretical number of counts for a arbitrary neutron fluence can be calculated. The ratio, i.e. the *number of counts per number of incident neutrons* is referred to as the *response* of the sensor, which is a useful value to characterize the effectiveness for neutron detection. This definition is for example applied in [20, 21]. However, the response is often defined as *counts per neutron fluence* as well, which is equivalent besides the factor A, i.e. the sensor area. With R denoting the response (unit $[R] = \mathrm{cm}^2$), this yields according to (A.4)

$$R = \frac{N_c}{\Phi_n} = \frac{N_c \cdot A}{N_n} = A \cdot \int_{E_{thresh}}^{\infty} \mathrm{d}E_{coll} \cdot \frac{\mathrm{d}^2 N_{events}}{\mathrm{d}N_n \mathrm{d}E_{coll}} \equiv A \cdot \eta \tag{A.5}$$

Thus, in this thesis η denotes the response per unit sensor area, i.e. $\eta = \frac{R}{A}$.[6] Another definition is the response related to *dose* η', i.e. the number of counts per personal dose equivalent $H_p(10)$. With (2.4), the definition of this quantity (unit $[\eta'] = \mathrm{Sv}^{-1}$) is

$$\eta' = \frac{N_c}{H_p(10)} = \frac{N_c}{h \cdot \Phi_n} = \frac{R}{h} = \eta \cdot \frac{A}{h} \tag{A.6}$$

The responses of the various sensors of the HMGU dosemeter are the central quantities in this work. As will be shown later, the overall response is quite different between the different sensors, partly because of the comparator settings E_{thresh}, partly because of geometric reasons and partly because of the converter composition and thickness. The influence of the neutron energy E_n on the response is huge as well. By running simulations with various incident energies, it becomes possible to approximate the *response function* $R(E_n) \propto \eta(E_n)$ for each sensor, i.e. to investigate the dependency of R on E_n.

Thus, once the response is known at a number of energies, a assumption of $R(E_n)$ can be made by *interpolating* the simulated results. Then, the response to a neutron *spectrum,*

[6] Since $A = 2.0\,\mathrm{cm}^2$, the conversion between the two definitions is easy.

$\bar{R} \propto \bar{\eta}$, i.e. with non mono-energetic neutrons, can be calculated according to

$$\bar{\eta} = \frac{\bar{R}}{A} = \frac{\int \mathrm{d}E_n \eta(E_n) \frac{\mathrm{d}\Phi_n}{\mathrm{d}E_n}}{\int \mathrm{d}E_n \frac{\mathrm{d}\Phi_n}{\mathrm{d}E_n}} \tag{A.7}$$

According to

$$N_c = N_n \cdot \bar{\eta} = \Phi_n \cdot \bar{R} \tag{A.8}$$

this can be used to calculate the number of counts that would be measured in a neutron field with the appropriate energy distribution $\frac{\mathrm{d}\Phi_n}{\mathrm{d}E_n}$ if a certain number of neutrons N_n hit the sensor with area A, i.e. if the neutron field had the fluence $\Phi_n = \frac{N_n}{A}$.

When comparing with measurements, an *uncertainty* has to be assigned to the simulated response values. The overall uncertainty ΔR is given by the uncertainties of fluence (that is, $\frac{N_n}{A}$) and counts $\Delta\Phi_n$ and ΔN_c. In the case of simulations, where the uncertainties are purely statistical, the influence of other quantities like ΔA or evenΔE_n is zero, since those variables are controlled by the user. N_n and N_c are distributed according to the *Poisson distribution*; the uncertainties are thus $\Delta\Phi_n = \frac{\Delta N_n}{A} = \frac{\sqrt{N_n}}{A}$ and $\Delta N_c = \sqrt{N_c}$ ([45, 99]). With

$$\Delta R = R \cdot \sqrt{\left(\frac{\Delta\Phi_n}{\Phi_n}\right)^2 + \left(\frac{\Delta N_c}{N_c}\right)^2} \tag{A.9}$$

this yields

$$\Delta R = R \cdot \sqrt{\frac{1}{N_n} + \frac{1}{N_c}} \tag{A.10}$$

For measurements, response values for comparison can be calculated from the number of counts and the neutron fluence; in that case however, further uncertainties, both statistical and systematical ones, have to be considered (chapter 5).

A.4. Geant4 validations

Unlike several other Monte Carlo codes, e.g. MCNP ([70]), GEANT4 is freely available in numerous versions. Its source code is improved and the functionality expanded steadily, and newer versions are published usually twice a year. Although the outcomes of the simulations are usually reliable, and the whole framework is well validated ([26]), the rapid development however means that in certain cases the results of a particular simulation have to be checked against analytical results or measurements.

For the dosemeter simulations, two points were considered critical. First, it had to be checked whether GEANT4 is capable of assigning the energy deposition in very thin layers of Silicon (the detector layers, as described in A.3) correctly. Furthermore, the remedy used in this work for the incorrect calculation of E_α and E_t due to the cross section problems (see supplement A.2), i.e. the swapping of the cross section files, had to be tested.

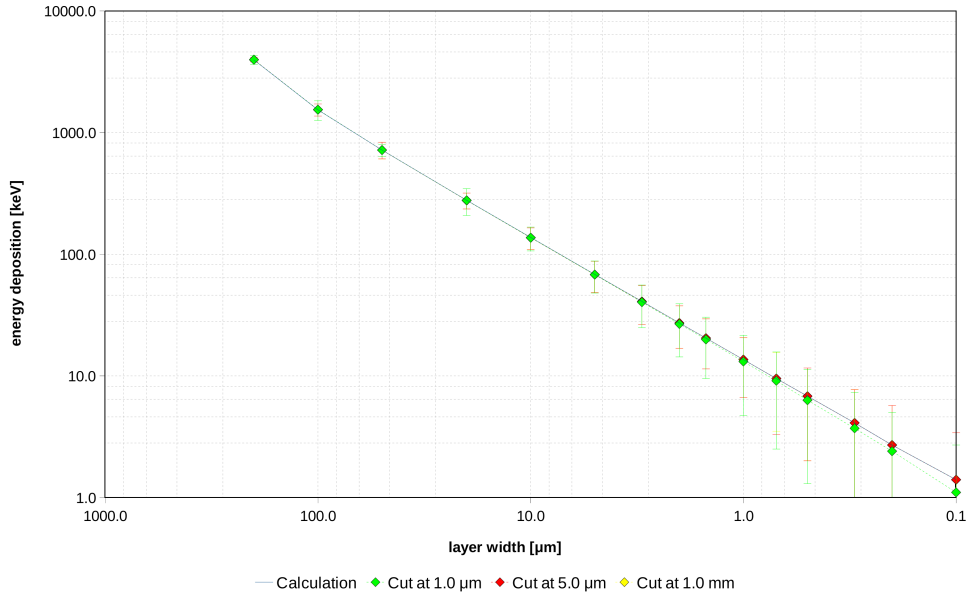

Figure A.2.: Energy deposition of 5.0 MeV protons in a Silicon slab of variable thickness. The (descending) thickness is displayed on the x-axis, the energy deposition per particle on the y-axis. The points refer to GEANT4 simulation with different range cut values; the line corresponds to a calculation from the stopping power [107].

Energy deposition in thin layers

As mentioned above, the GEANT4 simulations of the dosemeter are scoring the energy deposition in 100 or 200 layers of Silicon, each with a thickness of 4 μm or 2 μm in order to enable a weighting with the charge collection efficiency ϵ_q during the analysis. As there were doubts if the calculation of the deposited energy, especially concerning different range cuts, worked correctly,[7] a simple test simulation was run. In that program, *protons* with a kinetic energy of 5.0 MeV were used as primary particles; the physics list applied here was *QGSP_BERT,* i.e. the Bertini model with standard electromagnetic physics (see supplement A.1). The geometry was a simple Silicon slab with a specific thickness and a energy deposition scorer assigned to it. In several simulation runs, the energy deposition per incident particle in the Silicon layer was scored. In between those runs, the thickness of the layer was changed, varying from 400 μm to 0.1 μm. Furthermore, three different range cuts were applied, which were 1.0 μm, 5.0 μm and 1.0 mm.

As a comparison, the energy depositions in the Silicon films of varying thicknesses were calculated from the *stopping power* values given in the NIST database ([107]), assuming that the energy loss of a proton in matter is equivalent to the energy deposition in that matter. In order to yield the energy deposition, the values were integrated using the *trapezoid rule*.

[7] M. Wielunski (HMGU), private communication

Results of the simulations and a comparison with the NIST calculation are displayed in figure A.2. It turns out that down to a Silicon thickness of 0.1 μm, all results agree rather well. Concerning the simulations, there is only a slight difference between the values obtained with a range cut of 1.0 μm and the ones with a higher cut. The points obtained with cut values of 5.0 μm and 1.0 mm are not the distinguishable. Above around 1.0 μm slab thickness, the simulated and calculated energy deposition show almost no difference. Below, the energy deposition with a range cut of 1.0 μm is slightly lower than the other values; this can be attributed to the *delta rays*, i.e. secondary electrons with rather high kinetic energy that leave the volume without depositing much of their energy there. Their energy of course contribute to the energy loss of the proton and is incorporated in the NIST values from which the curve in figure A.2 is calculated. With high cut values, those secondaries are not produced in the Monte Carlo simulations, and thus their energy is deposited locally yielding a similar behavior. Only with a very small range cut, the delta electrons are tracked, and the energy deposition decreases.

This test shows that the energy deposition in thin layers is handled correctly by the GEANT4 scorers, even in layers with thicknesses below 1.0 μm. In the case of very thin films, the range cut should be set to a small value. Thus, for the dosemeter simulations, a range cut corresponding the the layer thicknesses of the Silicon detector was chosen, which was 2.0 μm mostly. When simulating the dosemeter on a phantom, cuts were assigned to the different *regions* separately, so it was possible to apply a range cut of 2.0 nm, but only in the sensor regions themselves.

Kinematics and cross-section of the $^6Li\,(n,\alpha)\,^3H$ reaction

When using the *High Precision Neutron Package*, cross sections from the ENDF-B/VI database ([44]) are used to calculate the kinematics of neutron reactions with certain nuclei ([79]). As it was mentioned in supplement A.2, an error in the treatment of the reaction (3.7), i.e. $^6Li + n \rightarrow {}^4He + {}^3H$, concerning the energy of the emitted alpha and tritium particles was reported in the GEANT4 forum (see footnote on page 141). To fix this problem, the cross section data files for ^6Li from a newer version of GEANT4 (i.e. 9.5) were used to replace the incorrect one.

To determine the correctness of this procedure, another simple simulation program was created, with *QGSP_BERT_HP* as a physics list and neutrons with $E_n = 10\,\text{keV}$ as primary particles. The geometry consisted of a ^6Li slab with a thickness of $d = 1\,\mu\text{m}$. The energy and fluence of tritium ions ^3H were scored with a $1.0 \times 1.0\,\text{mm}^2$ scorer behind the Lithium layer at a distance of 9.8 mm. The solid angle corresponding to this is $\Omega = \frac{1.0\,\text{mm}^2}{(9.8\,\text{mm})^2} \approx 10.4\,\text{msr}$. Furthermore, the number of produced ^3H ions in the Lithium target was scored. The two scorers were restricted to tritium by applying an appropriate *filter*.

The test simulation was run with $1 \cdot 10^9$ primary neutrons. The outcome was compared to analytically calculated values. For the number of reactions, the cross section at 10 keV, which is $\sigma_{n,\alpha} \approx 1.504\,\text{b}$ according to [44], and the density of ^6Li, $\rho \approx 0.534\,\text{g/cm}^3$, were used to

calculated the interaction probability within the $1.0\,\mu$m Lithium film according to equation (2.3), that is $p = 1 - \exp(-\Sigma_{n,\alpha} d) \approx 8.04 \cdot 10^{-6}$. Thus, for one billion incident neutrons, $N_{calc} = 8040 \pm 90$ (n, α) reactions are expected. The simulation result acquired by the tritium production scorer was $N_{sim} = 7941 \pm 89$, which agrees with the theoretical value within the error ranges.

From the 7941 reactions, nine, i.e. 9 ± 3 tritium particles were emitted in forward direction and registered by the $1.0 \times 1.0\,\mathrm{mm}^2$ scorer. Their energy was between 2.79 MeV and 2.81 MeV, which is the correct range according to equations (3.8) and (3.9) as well as figure 3.10. Assuming that the emission of ${}^3H$ ions is isotropic, one expects 6.7 ± 2.7 particles in a solid angle $\Omega \approx 10.4\,\mathrm{msr}$ from $N_{calc} = 8040 \pm 90$ tritiums being produced. This again fits well to the simulated value.

In order to judge the outcome of this test, one must consider that the original problem leading to the remedy applied here was that GEANT4 calculated a tritium energy of $E_t = 1.56\,\mathrm{MeV}$ according to footnote 5 on page 141. That energy however was no longer scored in the simulation with the fixed cross section files. It can thus be considered save to apply the presented workaround to create reliable simulation results.

B. Comparison of simulation results with mono-energetic measurements

The simulation results presented in section 4.2 give the response $\eta = \frac{R}{A}$ of the various sensors of the HMGU dosemeter at certain points of neutron energy E_n. By interpolation, the dependency of the response on that energy, that is $R(E_n)$, can be approximated. Before a comparison with the measurements conducted in this work can be done however, equation (A.7) has to be applied for the energy distribution of each experiment in question. The response value at a distinct energy can not be validated that way.

Using mono-energetic neutrons however, the mono-energetic responses of the sensors can be measured directly, at least in an energy range where such neutrons are available. An appropriate experimental campaign at the Physikalisch-Technische Bundesanstalt (PTB) has been done with the dosemeter prototypes. These measurements were not conducted in the frame of this work, and the final results as well as a thorough description of the experimental setup will be given in a forthcoming Master´s thesis.[1] Here, only the result of a preliminary analysis is outlined.

At the PTB, accelerator-produced protons and deuterons can be directed on deuteron, tritium and Lithium targets producing neutrons in ${}^3H(p,n)$, ${}^3H(d,n)$, ${}^2H(d,n)$ and ${}^7Li(p,n)$ reactions. The neutrons are measured behind the target in direction of the primary beam, so that their kinetic energy is given by the beam energy and the Q-value of the appropriate reaction. Seven different neutron energies have been utilized in the experiment with the dosemeters, ranging from $E_n \approx 140\,\mathrm{keV}$ to $E_n \approx 14.8\,\mathrm{MeV}$. The fluence at each energy corresponded to a dose of $H_p(10) \approx 0.9 \ldots 5.4\,\mathrm{mSv}$, respectively, in a distance of either $d = 1\,\mathrm{m}$ or $d = 1.5\,\mathrm{m}$ from the target. For the actual measurements, eight dosemeters were attached to two plexiglass phantoms in that distance d. The positions of the individual devices were on the surface were marked.

For the preliminary analysis, these positions were used to determine the correction factors for the fluence due to solid angle and cross section energy dependence. For the dosemeters in a maximal radial distance from the beam axis, the correction factors were in the order of 14 %. Also, the dependence of the neutron kinetic energy on the dosemeter position was taken into account. Here, the correction that had to be applied was less than 2 % for all devices. The mean energy for a given measurement was determined by averaging over the neutron energies at the eight dosemeter positions.

[1] F. Bergmeier and M. Wielunski (HMGU), private communication

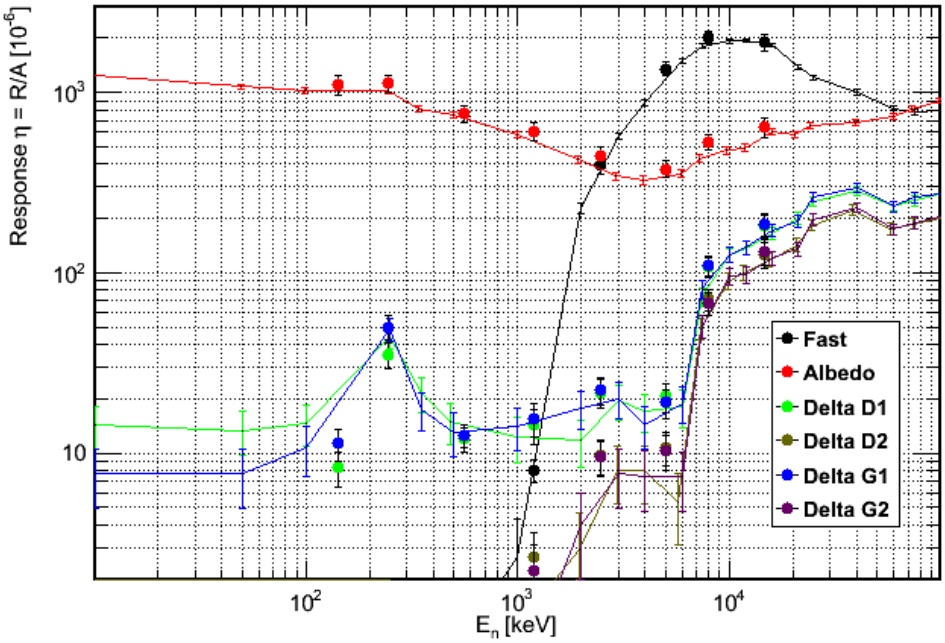

Figure B.1.: Response functions for the sensors of the dosemeter obtained with phantom, and response values measured at PTB (F. Bergmeier and M. Wielunski, HMGU, private communication)

For the calculation of uncertainties, the errors in radial and axial distance were estimated as $\Delta d = 0.5\,\mathrm{cm}$ and $\Delta r = 1\,\mathrm{cm}$, respectively. In the final analysis, these values will have to be concretized. The uncertainty in the dose (on the beam axis in distance d from the target) was around ${}^{\Delta H_p(10)}/_{H_p(10)} \approx 2.5 \ldots 5.5\,\%$ according to PTB statements.[2]

In figure B.1, the response functions of the six sensors calculated from the simulation results in chapter 4 are shown; as described there, a phantom geometry was used, as well as the Binary INC model as physics list and for neutron energies below 20 MeV the HP package. In the analysis, the lower threshold values given in the table on page 108 were used. For the general shape of the functions, this obviously makes little difference. The dependences of $R \propto \eta$ on E_n for the various sensors have been discussed shortly in section 4.2 already. Here, anyway, only the energy sub-range in which neutrons at the PTB are available is shown. The preliminary results of the measurement campaign are displayed in the same figure. In most cases, a remarkably good agreement with the simulations can be observed.

For the Fast sensor, only the energies $E_n > 1\,\mathrm{MeV}$ can be used for comparison, since the response is nearly zero below. In spite of the low experimental uncertainty here, the interpolated curve almost exactly reproduces the measured points. In case of the Albedo sensor, the characteristics of the response behavior with energy in the measurement is also given by the simulation very well. For nearly all tested energies, the interpolated curve lies

[2] S. Röttger (PTB), according to F. Bergmeier and M. Wielunski (HMGU), private communication

within the experimental uncertainty. The fact that in the PTB measurements the response is estimated slightly too high might be because of scattered neutrons from the other dosemeter devices, since they were positioned quite closely to each other on the phantoms.

For the Delta sensors, the comparison is generally more difficult because of the lower statistics due to the lower overall response. However, the same characteristic $R = R(E_n)$ dependence is shown in measurements and simulations, and agreement within the uncertainty range is true for most points as well. It must be noted that in some cases, seemingly huge discrepancies are owned to the linear interpolation of the simulated points; if the simulation resolution was higher, the agreement in the cases of e.g. $E_n \approx 140\,\mathrm{keV}$ or $E_n \approx 2.5\,\mathrm{MeV}$ would be better.

Generally, it can be concluded from the graphical comparison that the simulation results reproduce the (experimentally) true behavior of the response very well for all sensors of the dosemeter, at least in the energy range considered here. This is a very important indication for the reliability of the GEANT4 applications created in this thesis. During their development, former PTB measurements (e.g. [21, 15, 3]) have already been used for checking; as a final comparison in the present thesis however, only the newest results are shown, since only in their case prototypes with the current design have been tested.

Publications from this work

From the present work, two publications originated, that is one article in an international journal which will be published soon, and one poster with corresponding oral presentation:

Article *Intercomparison of Radiation Protection Instrumentation in a Pulsed Neutron Field*
M. Caresana, A. Denker, A. Esposito, M. Ferrarini, N. Golnik, E. Hohmann, A. Leuschner, M. Luszik-Bhadra, G. Manessi, S. Mayer, K. Ott, J. Röhrich, M. Silari, F. Trompier, M. Volnhals, M. Wielunski
Nuclear Instruments and Methods in Physics Research A, to be published

Poster Presentation *Development of Active Neutron Dosemeters*
M. Volnhals, M. Wielunski, W. Rühm
Advanced WE-Heraeus Physics School "Ionizing Radiation and Protection of Man", Bad Honnef, August 2012
awarded with a "Best Poster Prize"

Further publications on the charge collection efficiency of the PIN-diodes (section 3.2) and the measurements at the PTB (supplement B) are currently being prepared.

Acknowledgment

This thesis would not have been possible without the support of numerous people, especially at the HMGU, the TU and of course in my private circle.

First and foremost thank Dr. Marek Wielunski, not only for telling me everything about the HMGU dosemeter, but also for countless general notes on physics, measurement techniques and electronics, as well as for being a likable companion when traveling and for his willingness to turn a blind eye if necessary.

Special appreciation I owe Prof. Werner Rühm, the supervisor of this thesis, for enabling it, for the many discussions and for always having a scrutinizing view on my work. The members of his group I would like to thank for their help with routine problems, for the discussions, the supply with data and knowledge and for the friendly company. Especially I would like to highlight Sebastian Trinkl for his help with Linux, Dr. Christian Pioch for notes and examples to GEANT4, Vladimir Mares for the Zugspitze spectra and last but not least Anita Herrling, for organizing practically everything. Thanks also to my workmates, especially *dem Faulen* and *dem Fleißigen* as well as Pedro Nogueira, for the funny time we had.

I also owe appreciation and special thanks to Prof. Shawn Bishop, the reviser and advisor of this thesis, for his willingness to supervise a work which is only slightly related to his own area of research. Without him, all this would not have been possible at all.

Since with the finishing of this thesis not only my affiliation to the HMGU, but also my physics studies are over (at last), it is time to express gratitude to some persons that have played an important role in my education. Among these, I thank Karl Müller of the KKI and his team, without whom I would not have studied physics and Dr. Nevena Martin, without whom I would not have learned to program.

Many thanks I also owe to my friends, who so often had to miss my company during my studies and especially during the creation of this thesis.

Martina, who has been my love and company all during my studies, deserves my gratitude and appreciation very much, since she has to experience all the *Schmarrn* I come up with and still makes my life worth something. I thank her not only for being my girl-friend (my quasi-wife), but for being a *friend*.

Of course, my special appreciation goes to my parents and family, who not only provided financial help but also, which is more important, encouragement, patience and a sympathetic ear to my problems. I thank them for their struggle to bring me to the point in life I am now, and hope that they can feel happy and proud of what they have accomplished in that.

Erklärung

des Diplomanden

Name: Volnhals
Vorname: Matthias

Mit der Abgabe der Diplomarbeit versichere ich, dass ich die Arbeit selbständig verfasst und keine anderen als die angegebenen Quellen und Hilfsmittel benutzt habe.

Landshut, 13.11. 2012